Thesis for the Degree of Doctor of Philosophy

Understanding the Circumstellar Structure of High-Mass Young Stellar Objects Based on Interferometric Observations

Jungha Kim

School of Physical Sciences

Department of Astronomical Science

SOKENDAI

Kanagawa, Japan

September, 2020

Understanding the Circumstellar Structure of High-Mass Young Stellar Objects Based on Interferometric Observations

by

Jungha Kim

Advised by

Dr. Mareki Honma

Dr. Tomoya Hirota

Dr. Katsunori Shibata

Dr. Hideyuki Kobayashi

Submitted to the Department of Astronomical Science

and the Faculty of the Graduate School of

SOKENDAI in partial fulfillment

of the requirements for the degree of

Doctor of Philosophy

Understanding the Circumstellar Structure of High-Mass Young Stellar Objects Based on Interferometric Observations

by

Jungha Kim

Submitted to the Department of Astronomical Science
on September 29, 2020, in partial fulfillment of the
requirements for the degree of
Doctor of Philosophy

Abstract

Summary of snapshot imaging survey of H_2O maser using KaVA is presented to examine typical trend in spectral and spatial distributions of maser features and select appropriate target to investigate in detail. Detected 15 H_2O maser sources are classified into three groups: three for “blue” , two for “red”, and 10 for “both”. The H_2O masers in “both” group are highly expected to trace bipolar outflows and isotropically expanding shells/winds even though targets in “blue” and “red” would be tracing a apart of those structures. These 10 targets in “both” group are largely divided into two groups: five sources are classified as “compact” while others are in “elongated”. “Elongated” structure may trace bipolar outflows with high possibility while “compact” structure is hard to imagine what kinds of dynamical structures can be traced. To examine the environmental difference between these two groups, the 3D velocity structures of H_2O masers are going to be obtained with monitoring observations. To investigate the trend in the distribution of H_2O masers, morphology factor was defined as $\alpha = l_{\max}/l_{\min}$ where $l_{\max}$ and $l_{\min}$ are major size and minor size of H_2O maser distribution, respectively. Therefore, G25.82-0.17, one of targets having the largest morphology factor about 0.4, was selected for the first case study from the KaVA LP as a first step to KaVA LP ultimate goals. Based on the results from the imaging survey, monitoring observations were done including G25.82-0.17.

G25.82-0.17 was selected for the pilot case study as the first step to KaVA LP ultimate goals since it shows about 60 features with 60 velocity range, suggesting it is a good laboratory to investigate the connection between the dynamical structures in the vicinity of the powering source and H_2O maser 2D and 3D distributions. It is very important for verification of technical and scientific aspects of KaVA LP studies at the same time before extending the research.

By taking full advantage of VERA and KaVA observations, parallax and proper motions of H_2O masers in G25.82 are measured to estimate accurate distance and 3D velocity structure of H_2O masers for further analysis. In addition, the galactic position and the peculiar motion of G25.82 is presented to compare with other high-mass star forming regions. The 8 maser features have been successfully employed detected in more than five epochs. Obtained parallax is 0.225 ± 0.020 mas, corresponding to a distance of $4.44^{+0.4}_{-0.4}$ kpc which is a factor of 0.89 (=4.44 kpc/5.0 kpc) smaller than the kinematic distance. In case of uncertainty, it is reduced to 10% of 89%.

In addition to annual parallax, internal proper motions of H_2O maser features in G25.82 were measured. In total, 21 H_2O maser features were identified which were detected at least in three epochs. Most of identified H_2O maser features have blueshifted or similar velocities to the systemic velocity of G25.82 (93.7 km s^{-1}). In addition to the bluest feature, slightly redshifted velocity component (97.1 km s^{-1} feature) moving toward the NE. Features having velocities close to the systemic velocity distributed at Dec offset$\sim$ 0 are moving away with each other. The central cluster shows motions divided into two groups which are moving toward N and SW.

Moreover, the galactic position of G25.82 is measured and it is on the "Scutum-Centaurus Arm" at the edge of "Long Bar" at the galactic center with the location in the middle of other neighboring high-mass star-forming regions. Therefore, G25.82 is also located at the inner Galaxy region where the star formation is actively occurring. In addition to the galactic position, the peculiar motions of the maser source can be estimated by subtracting the effect of Galactic rotation and the peculiar motion of the Sun from the motion of the maser source. It may be strongly affected by the parallax uncertainty, we obtained the peculiar motion components of G25.82 to be ($U_{\rm s}$, $V_{\rm s}$, $W_{\rm s}$) = (33, −9, 18).

Results of continuum and spectral line observations with ALMA and 22 GHz water (H_2O) maser observations using KaVA and VERA toward a high-mass star-forming region, G25.82–0.17 are presented. Multiple 1.3 mm continuum sources are revealed, indicating the presence of young stellar objects (YSOs) at different evolutionary stages, namely an ultra-compact HII region, G25.82–E, a high-mass young stellar object (HM-YSO), G25.82–W1, and starless cores, G25.82–W2 and G25.82–W3. Three sets of CO outflow lobes are detected. Two of them have N–S direction while the other has SE–NW. In addition, two SiO outflows, at N–S and SE–NW orientations, are identified. The CH_3OH 8_{-1}–7_0 E line, known to be a class I CH_3OH maser at 229 GHz is also detected showing a mixture of thermal and maser emission. Moreover, the H_2O masers are distributed in a region $\sim 0''.25$ shifted from G25.82–W1. The CH_3OH 22_4–21_5 E line shows a compact ring-like structure at the position of G25.82–W1 with a velocity gradient, indicating a rotating disk or envelope. Assuming Keplerian rotation, the dynamical mass of G25.82–W1 is estimated to be >25 $M_\odot$ and the total mass of 20 $M_\odot$-84 $M_\odot$ is derived from the 1.3 mm continuum emission. The driving source of the N1–S1 CO outflow (N–S SiO outflow) is G25.82–W1 while that of the SE–NW CO (SiO) outflow is uncertain. Outflow parameters obtained from the CO 2-1 line, reveal that the N1–S1 CO outflow is tracing the smaller scale and higher velocity outflow from the driving source than the $C^{18}O$ outflow detected by the single-dish observations. Furthermore, the relationships between time-dependent outflow parameters (mass lose rate, force, and luminosity) and with the source luminosity have the similar relationships shown in low-mass to high-mass regime, suggesting the star-forming mode in G25.82 is likely a scaled-up version of low-mass star formation. Although one cannot be ruled out that a possibility of the existence of multiple unresolved low-mass YSOs, detection of multiple high-mass starless/protostellar cores and candidates without low-mass cores implies that HM-YSOs could form in individual high-mass cores as predicted by the turbulent core accretion model. If this is the case, the high-mass star formation process in G25.82 would be consistent with a scaled-up version of low-mass star formation.

Thesis Supervisor: Mareki Honma
Title: professor

Thesis Supervisor: Tomoya Hirota
Title: professor

Thesis Supervisor: Katsunori Shibata
Title: professor

Thesis Supervisor: Hideyuki Kobayashi
Title: professor

Contents

List of Figures

List of Tables

Chapter 1

Introduction

1.1 High-mass Star Formation

High-mass stars, also called OB type stars, have luminosities larger than $10^3 L_\odot$ and stellar masses larger than $8M_\odot$. They are known to have large impact not only their close neighborhood but their whole natal clusters during their whole lifetime (Zinnecker & Yorke, 2007; Tan et al., 2014). They also provide heavy elements for the next generations of stars and influence the initial mass function (IMF) of their parental environments. Despite that, the formation of high-mass stars remains incompletely understood compared to that of low-mass counterparts. Understanding high-mass star formation process is important to itself and it is fundamental to fully constrain the origin of the formation of high-mass star clusters and the initial mass function (IMF). It can also provide accurate constraints such as star-formation rates (SFR) and IMF for galactic studies and numerical simulations.

1.1.1 Theoretical review

The basic concept of high-mass star formation is still controversial since different high-mass star-forming mechanisms have been proposed. The two competing theoretical models that describe the formation of high-mass stars are as follow:

Monolithic collapse (Core accretion). This model predicts that high-mass stars are formed (in most cases) from isolated massive dense cores fragmented from the natal molecular cloud (McKee & Tan, 2002). Monolithic collapse in these isolated massive dense cores with self-gravitating turbulent structure is expected. The star in birth gathers material from this massive dense core alone. The expected core mass function is similar to Initial Mass Function (IMF) (Krumholz et al., 2005). The accretion rates of $10^{-4} - 10^{-3}$ $M_\odot$ yr^{-1} (McKee & Tan, 2003) are required to overcome radiation pressure from the central protostar to accrete more mass to be massive. From the observational studies, the high accretion rates are often observed (e.g., Beltrán et al., 2011). The monolithic collapse process is slow and quasi-static. Given the non-zero angular momentum of the collapsing core, this model predicts the existence of protostellar accretion disks around massive stars (Yorke, & Sonnhalter, 2002). These accretion disks have been recently found around early-B to late-O type stars by interferometric observations (Beltrán & de Wit, 2016; Hirota, 2018).

The weakness of this theory is that the lack of evidence for the existence of truly isolated massive stars. de Wit et al. (2005) reported that only 4% of O type stars might have formed in the outside of a young cluster. In addition, the presence of monolithic prestellar cores is unconfirmed. Even though there have been few claims of their existence (Tan et al., 2013; Wang et al., 2014; Sanhueza et al., 2017), the cores are not massive nor dense enough to from a high-mass star in many cases. Finally, one of the big caveats of this model is fragmentation. Krumholz et al. (2007) has proposed that the increase in Jeans masses by heating from the protostellar object could prevent fragmentation. Alternatively, as suggested by Hennebelle et al. (2011) and Commerçon et al. (2011) simulations, fragmentation could be controlled by the magnetic field. With high magnetized environment, a low level of fragmentation is shown in cores in these simulations while a high level of fragmentation is shown in turbulence dominant cores over magnetic field.

Competitive accretion. This model highlights two factors of high-mass star formation, their location and time of birth. It predicts the initial fragmentation of clumps results in a cluster of low-mass dense cores with masses close to the Jeans masses. The central cores compete with the other cores to gather its masses to form high-mass stars (Bonnell & Bate, 2006). The global collapse is expected in cloud scale and the most massive stars are located near the center of the gravitational potential. In this theory, high-mass stars always form in clustered environments.

In the initial competitive accretion model, disks were not predicted, or were small, due to severe impact from the tidal interactions with other members of the protocluster (Cesaroni et al., 2006). Updated version of the competitive accretion model also predicts the presence of disks around the members having the highest masses in the cluster.

The claim is proposed by Krumholz et al. (2005) that this model is not appreciable to make massive stars because the virial parameters and accretion rates are too low. They argued the protostellar masses would not to be allowed to grow in such a turbulent environment with the low accretion rates. In addition, according to theoretical calculations, Bondi-Hoyle accretion is halted when the central protostellar mass reaches around 10 $M_\odot$ because of radiation pressure. Finally, another weakness of the model is that stellar feedback from the newly-formed OB-type stars was not taken into account. Bonnell & Bate (2006) proposed that high-mass stars form through a competitive accretion process after a gravitational collapse to answer the criticisms. Most of these criticisms have been answered by proposing that initially the relative velocities between gas and stars are low and the turbulence is locally small, which allows the low-mass stars to accrete mass. In addition, regarding feedback from OB-type stars, through disk-mediated accretion process, the mass flow can avoid affection of the incident UV flux.

In either case, high-mass young stellar objects (HM-YSOs) require higher mass accretion rates of $10^{-4} - 10^{-3}$ $M_\odot$ yr^{-1} (McKee & Tan, 2003) compared to that of low-mass YSOs ($\sim 10^{-6} M_\odot \mathrm{yr}^{-1}$; Evans et al., 2009) to accrete mass to the central star by overcoming radiation pressure problem. Higher mass accretion rates result in shorter evolutionary timescales. Non-spherical accretion has been proposed as a possible solution to the stellar feedback problem to form OB-type stars (Nakano, 1989; Jijina & Adams, 1996). Theoretical studies in recent years show agreement with disk-mediated accretion scenarios for both theoretical models (e.g., Krumholz et al., 2009; Kuiper et al., 2010, 2011; Klassen et al., 2016; Beltrán, 2018a).

1.1.2 Observational review

Evolutionary scenario for high-mass stars has also been suggested based on observations Figure 1.1. Despite the lack of information on evolutionary sequence, a terminology for high-mass precursors exists. Most high-mass stars born within the dense massive molecular cloud. Objects considered as the first stage of high-mass star formation have been called high-mass starless clumps, high-mass prestellar cores, or infrared-dark clouds (IRDCs). As already mentioned, the larger-scale cloud structures remains unclear, however, high-mass prestellar cores would be gravitaionally bound cores that will collapse and form individual high-mass stars or binaries. Sources in the following phase are called hot molecular cores (HMCs), high-mass protostellar objects (HMPOs). Masses to be high-mass star are gathered in this phase. When and how the material falls into the central part are still far from understanding. The final phase are associated with HII region, hypercompact HII (HCHII) region and ultracompact HII (UCHII) region.

High-mass stars impact their natal environment through a various feedback effects. They eject momentum, mechanical and thermal energy into the surrounding medium via protostellar jets/outflows and radiation pressure. Since outflows also play a key role in controlling the high-mass star formation itself by extracting angular momentum from the system to prevent halting accretion, YSOs having rotating disks are usually accompanied by outflows (disk-outflow system). Despite the ratio of accretion to ejection rate is roughly determined, accretion process through the disks in the system is closely connected to the ejection process by outflows. Observing outflows is good tool to investigate accretion process indirectly to get a clue to solve the mystery of the high-mass star formation. Evolution of outflow itself in time (e.g. opening angle, inclination, and power, etc) also provides information to establish

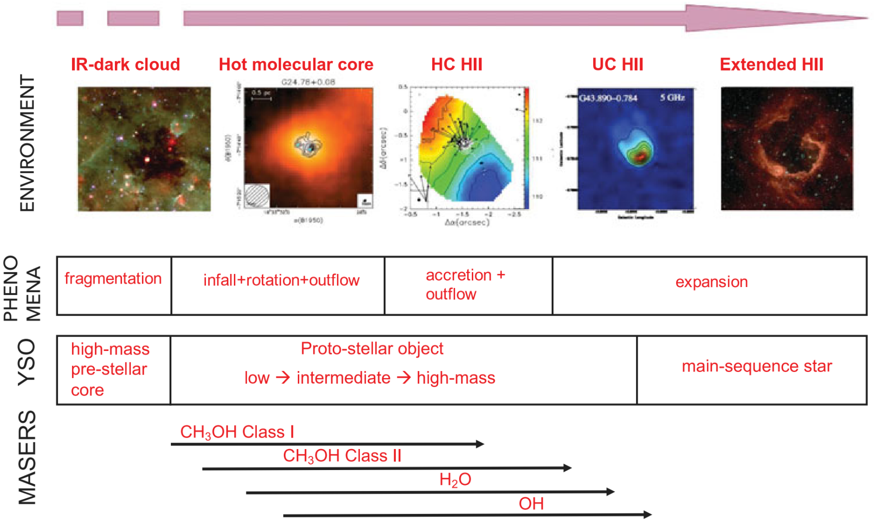

Figure 1.1: Evolutionary sequence for high-mass stars from cold IRDCs to chemically rich HMCs to HII regions from Beltrán (2018a).

the evolutionary scenario of HM-YSOs. Detailed observational studies of disk-outflow system are crucial to understand when and how stars gather their masses to be massive.

Observations toward HM-YSOs are in progress to establish the evolutionary sequence based on observations and give accurate constraints for modeling. However, observing high-mass star-forming regions are challenging. Since the evolutionary timescale of HM-YSOs are short, they remain embedded in their natal envelopes. In addition, most HM-YSOs are located at distance > 1 kpc from the sun and they usually form in clustered environment where the stellar separation is < 1 pc, which makes them difficult to resolve. Target itself is rare and limited. Therefore, investigating high-mass star and massive cluster formation requires high angular resolution imaging at far-infrared (FIR) to (sub)millimeter wavelengths.

Advances in (sub)millimeter interferometry have enabled the identification of high-mass protoclusters, in which multiple millimeter continuum sources exist, and the detection of disks surrounding HM-YSO members. Multiplicity is commonly shown in high-mass star formation (e.g., Preibisch et al., 1999; Mason et al., 2009; Sana & Evans, 2011). In many cases, the members in the protocluster present a diversity in star formation signposts providing strong evidence that neighboring objects can exist in different evolutionary stages of formation in close proximity to each other. It emphasizes the potential interaction between HM-YSOs, as well as their possible impact on nearby low-mass YSOs. That is why observations with high spatial resolution is necessary to disentangle cause and effect in such a feedback loop. Furthermore, millimeter and centimeter imaging with high sensitivity is required to obtain an accurate census of their low-mass companions given the deeply embedded nature of protoclusters.

1.2 Current Interferometers

The angular resolution of interferometer is determined by the longest baseline of the array while the sensitivity strongly depends on the number of antennas or telescopes in the array. The number of baselines with N telescopes is $N(N-1)/2$. Successful interferometric operation of large (sub)millimeter arrays has been achieved over recent years. Astronomical interferometers are listed: (1) the Sub-millimeter Array (SMA) having 8 dishes; and (2) the Plateau de Bure Interferometer (PdBI) composed of 6 antennas originally and is upgraded to include 12 antennas more and renamed to NOEMA recently; (3) the Combined Array for Research in Millimeter-wave Astronomy (CARMA) operates with 23 telescopes; (4) one of the most powerful arrays is the Jansky Very Large Array (JVLA) with 27 antennas; (5) another is of course the Atacama Large Millimeter/submillimeter Array (ALMA) provides over 1000 baselines with > 50 dishes.

Even more smaller scales of signposts of star formation can be observed with Very Long Baseline Interferometers (VLBIs) with the highest angular resolutions among ground based arrays. Current powerful VLBI arrays are as follow: (1) Korean VLBI Network (KVN) and

VLBI Exploration of Radio Astrometry (VERA) arrays (KaVA) composed of three KVN 21-m antennas in Korea and four VERA 20-m antennas in Japan; (2) East Asian VLBI Network (EAVN); (3) The European VLBI Network (EVN); (4) The Very Long Baseline Array (VLBA).

Figure 1.2 shows the maximum angular resolution provided by the different interferometers at various wavelengths reported by Beltrán & de Wit (2016). As seen in this figure, the scales of star formation that interferometers and VLBI arrays can trace are totally different. The complementarity is aiming for a complete picture of a disk-outflow system of HM-YSO. Introduction on this is shown in the following Section.

1.3 Observational studies toward HM-YSOs

As already mentioned above, detailed studies of disk-outflow system are essential to constrain current star-formation models. To do this, finding disk-outflow system around HM-YSOs and disentanglement of disk and outflow are going to be the first step. Although the number of observed targets with high spatial/spectral resolutions is still insufficient, many efforts are in progress by sub-arcsecond resolution observations using interferometers such as ALMA and SMA (e.g., (Kim et al., 2020)).

Signatures of rotating disks and/or envelope around B-type HM-YSOs have been reported even before the era of ALMA (Cesaroni et al., 2007; Beltrán et al., 2014; Sánchez-Monge et al., 2014; Hirota et al., 2017; Motogi et al., 2017, 2019; Beltrán & de Wit, 2016; Moscadelli et al., 2019). Velocity gradients have also been detected with scales of 100–1000 au around O-type HM-YSOs indicating circumstellar disks (e.g., Beltrán & de Wit, 2016; Beuther et al., 2017; Cesaroni et al., 2017).

In contrast, since it is unclear whether more massive O-type HM-YSOs can be formed in a similar way because such objects usually show more massive ($> 100 M_{\odot}$) and larger ($> 10^4$ au) rotating structures called toroids. The toroids are likely forming a group of stars in their centers. Cesaroni et al. (2017) found evidence for disks around the various O-type HM-YSOs

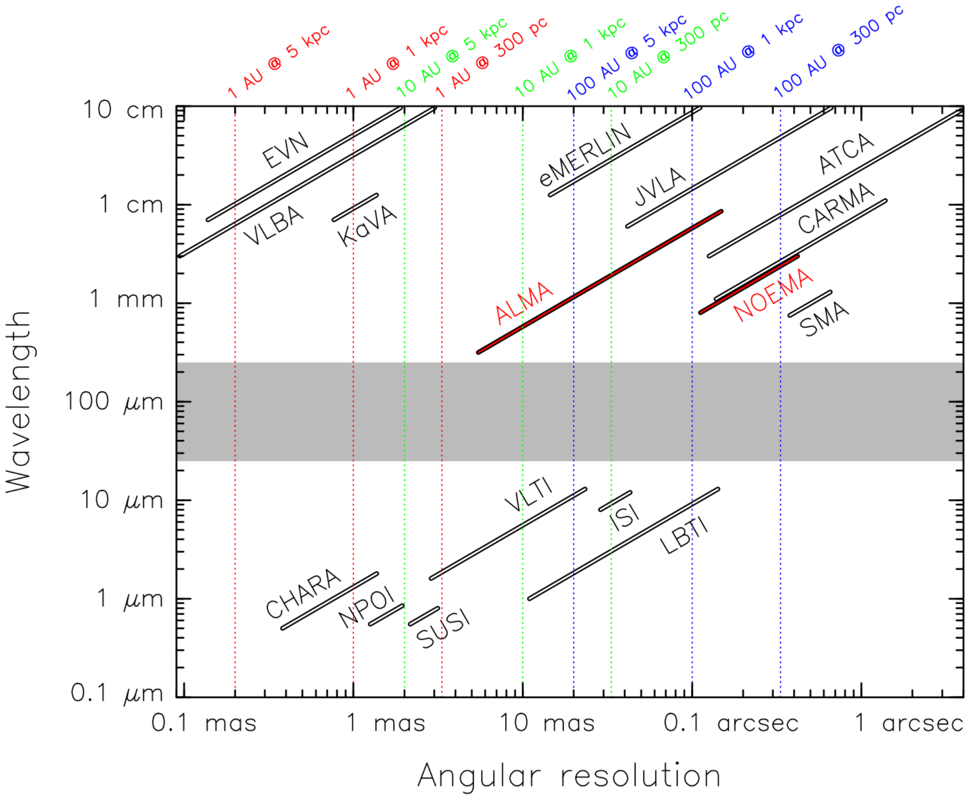

Figure 1.2: Wavelength coverage and maximum angular resolution of current interferometers from Beltrán & de Wit (2016). For ALMA and NOEMA, the wavelength coverage and angular resolution correspond to those provided by the completed interferometers. The shaded area indicates the range of wavelengths for which the atmosphere transmission is close to zero. Dotted vertical lines indicate the angular resolution needed to trace spatial scales of 1 au (red lines), 10 au (green lines), and 100 au (blue lines), for sources located at 300 pc, 1 kpc, and 5 kpc.

Table 1.1. Disk-outflow system in HM-YSOs

Source	Distance (kpc)	L_{bol} ($L_\odot$)	Resolution ($''$)	Disk radius (au)	Maser^b detection
G16.59-0.05^a	3.6	B-type	0.15	500	C2,H
NGC 6334 I SMA1b	1.3	B-type		800	C2
S255IR SMA1	1.78	B-type	0.1	1850	C2
Cepheus A HW2	0.725	B-type		360	C2
G35.02-0.74N A^a	2.19	B-type	~0.5	1500	C2,H
G35.02-0.74N B^a	2.19	B-type	~0.5	2600	C2,H
G353.273+0.641	1.7	B-type	0.09	250	C2
Orion Source I		B-type	~0.4		C2,H
G35.03+0.35 A	3.2	B-type	~0.5	2200	C2
IRAS 20126+4104	1.7	B-type	~0.5		C2
G339.88-1.26	2.1	B-type	~0.3	530	C2
G25.82-0.17^a	5.0	···	~0.3	5000	C1,C2,H
G24.78+0.08 A1	7.7	O-type	0.2	4600	C2
IRAS 16547-4247	2.9	O-type	0.06	1500	C2
G11.92-0.61 MM 1b	3.37	O-type	0.11	850	C2,H
G31.41+0.31^a	7.9	O-type	0.22	3600	C2,H
G17.64+0.16	2.2	O-type	0.02	~600	C2
AFGL 4176 mm1	4.2	O-type	0.3	2000	C2
G23.01-0.41^a	4.6	O-type	~0.2		C2,H

[a] Targets having direct comparison between the distribution of H_2O maser and that of thermal line emission.

[b] C1:Class I CH_3OH maser, C2:Class I CH_3OH maser, H:H_2O maser

by ALMA survey using CH_3CN tracer. They chose six luminous ($> 10^5\ L_\odot$) targets from the "toroid" sample of Beltrán et al. (2005, 2011). Detailed investigations of the half of these six sources, G31.41+0.31, G24.78+0.08, and G17.64+0.16 were done (Beltrán et al., 2018b; Maud et al., 2018, 2019; Moscadelli et al., 2018). Toward G17.64+0.16, a disk-like structure is detected in the SiO 5–4 line with the angular resolution of $0.2''$ as shown in Figure 1.3 (~ 400 au). Perpendicular to this disk-like structure, large-scale outflow in the ^{13}CO 2–1 line is observed using Atacama Compact Array. Accounting for all observational results, Maud et al. (2018) suggests that G17.64+0.16 is an O-type YSO in the final stages protostars that has not evolved into a compact HII region.

Clear velocity gradients are observed in the CH_3CN 12–11 line transitions toward G31.41+0.31 and G24.78+0.08. The gradient shown in G31.41+0.31 indicates rotational spin-up and infall motion toward the two central cores Figure 1.4. In case of G24.78+0.08, this gradient is caused by wind and outflow feedback from the O-type star at the center of an Hyper compact $\mathrm{H}ii$ region Figure 1.6.

In addition to survey results, individual studies toward O-type HM-YSOs have been reported with high angular resolution of $0.2''$. A fragmented Keplerian disk in the CH_3CN 12–11 lines is detected toward G11.92-0.61 MM 1 (Ilee et al., 2018). They claim that MM 1 is divided into two components, MM 1a , which is the source of a bipolar molecular outflow, and MM 1b, located 0.57" (1920 au) to the southeast. The total enclosed mass in MM 1a is 40 $M_\odot$ while MM 1b is <0.6 $M_\odot$. This mass ratio and orbital properties of these two sources suggest that MM 1b is one of the first observational results of the formation of a binary star via disk fragmentation around an HM-YSO.

Furthermore, Moscadelli et al. (2019) report the rotating structure around G16.59-0.05.

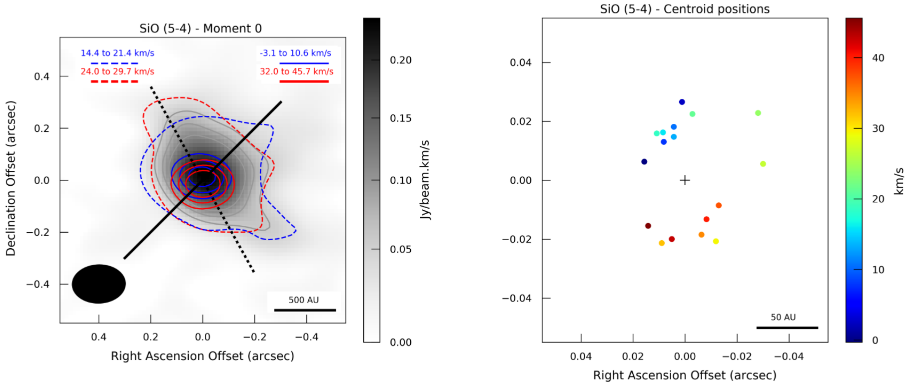

Figure 1.3: *Left panel*: integrated intensity map of the SiO emission integrated over the V_{LSR} between 21.4 and 24.0 km s^{-1}. The grey contours highlight the elongated emission. The blue and red solid contours show blue- and redshifted high velocity SiO emission (levels at 10, 15 and 20σ, where σ = 9.57 and 9.41 mJy $beam^{-1}$· km s^{-1} for the blue- and redshifted high velocity emission, respectively) while the dashed lines indicate the 10 σ level (σ = 7.54 and 6.58 mJy $beam^{-1}$· km s^{-1} for the blue- and red-shifted emission, respectively) of the lower velocity component. The synthesized beam is shown in the bottom left of the figure. The black solid line is the direction of the outflow while the dotted line is that of the disk major axis. *Right panel*: plot of the centroid positions from a two dimension (2D) Gaussian fitting of each channel of the SiO emission between -0.3 and 45.6 km s^{-1}, clearly showing that the blue- and redshifted emission are distributed to the north-east and south-west, respectively. The scale is changed by a factor of ten compared to the left panel (Maud et al., 2018).

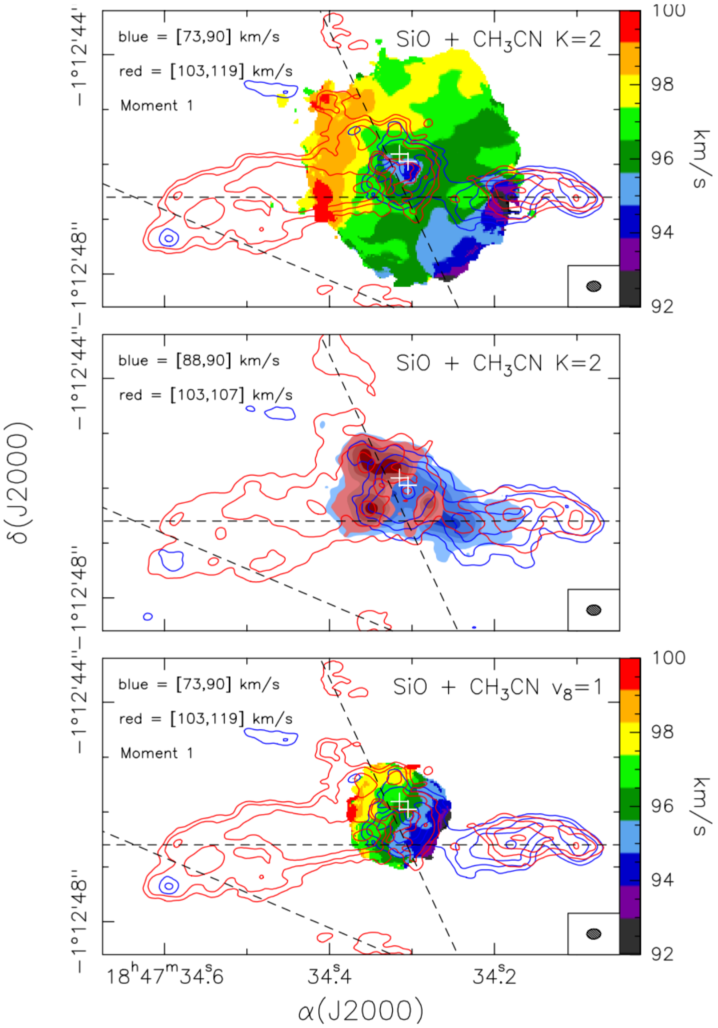

Figure 1.4: *Top panel*: moment 1 map of CH$_3$CN K = 2 (12–11) (colors) overlaid on the SiO 5–4 blueshifted (blue contours) and redshifted (red contours) averaged emission. The CH$_3$CN K = 2 line velocity map has been computed over the velocity range from 92 to 100 km s^{-1}. *Middle panel*: overlay of CH$_3$CN K = 2 (12–11) and SiO 5–4 blue- and redshifted. Contour and grayscale levels are 6, 18, 36, and 72 mJy beam^{-1}. *Bottom panel*: same as the top panel but for CH$_3$CN K, l = (6, -1) v8=1 (12–11). The synthesized beam is shown in the lower right corner. The white crosses indicate the positions of the two compact free–free continuum sources detected by Cesaroni et al. (2011). The black dashed lines indicate the direction of the three possible outflows from Beltrán et al. (2018b).

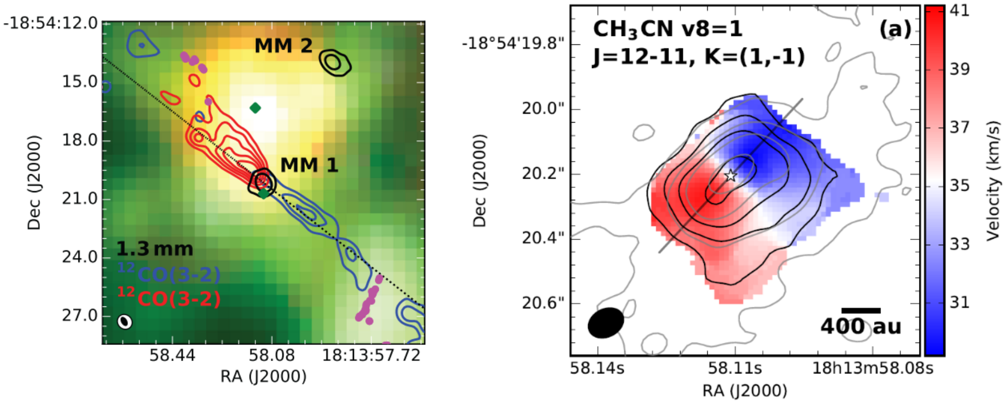

Figure 1.5: *Left*:SMA 1.3 mm continuum (black contours) and blue- and redshifted CO 3-2 emission. The outflow PA is denoted by the dotted black line (Ilee et al., 2018). *Right*: reproduced figure by Moscadelli et al. (2019) using Figure 2 from Ilee et al. (2018). Integrated intensity (black contours) and intensity weighted velocity (moment 1; color scale) for the CH_3CN $v8$=1 J=12–11 (K =1,-1) line observed with ALMA. The solid black line indicates the PA of the V_{LSR} gradient.

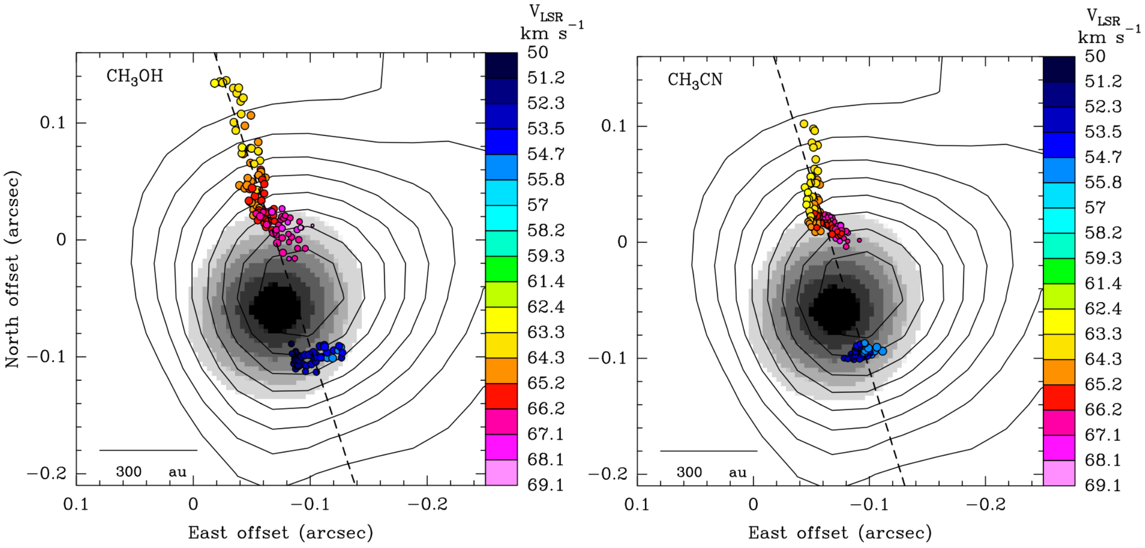

Figure 1.6: The disk around the high-mass YSO Bm (Moscadelli et al., 2019). Colored dots denote the peak positions of the bluest and reddest velocity channels for the emission of the nine CH_3OH (*left*) and seven CH_3CN (*right*) lines (see Table 2 in Moscadelli et al., 2019). The dashed black lines show PA for CH_3OH (18°) and CH_3CN (17°). JVLA 22 GHz and 13 GHz continuum are shown with grayscale and black contours, respectively.

1.4 Masers in High-mass Star Formation

One powerful tools to investigate the evolution of high-mass stars is molecular maser emission. The first discovery of astrophysical maser emission was hydroxyl (OH) emission toward several interstellar HII regions (Weaver et al., 1965). Molecular masers such as water (H_2O), methanol (CH_3OH), and OH, are known to be associated with a large number of HM-YSOs, and they provide information on the distribution and kinematics of shocked gas in their vicinity. These maser species are complementary with each other for investigating overall three-dimensional (3D) structures and dynamics around host objects by multi-epoch and multi-species VLBI studies. H_2O and CH_3OH masers will be introduced which are used for the analysis of this dissertation.

1.4.1 H_2O Maser

The first discovery of H_2O masers was reported by Cheung et al. (1968). It involved the $6_{16}--5_{23}$ transition at 22 GHz. It is the only water transition that can be observed using current VLBI arrays. The pumping mechanism for H_2O masers is known to be collision in high-density (10^7-10^9 cm^{-3}) and high-temperature (300-1000 K) regions (Stahler, & Palla, 2005). The 22 GHz H_2O masers trace shocked gas associated with various kinds of dynamical structures including low- (a few 10 km s^{-1}) and high- (>100 km s^{-1}) velocity outflows, disks, and HII regions (e.g. Moscadelli et al., 2005; Beltrán & de Wit, 2016; Motogi et al., 2016).

1.4.2 CH_3OH Maser

Since Ball et al. (1970) have reported the first detection of methanol (CH_3OH) masers, several CH_3OH masers were reported. CH_3OH masers are divided into two classes based on their pumping mechanisms (Menten, 1991). Class I CH_3OH masers (e.g. 44 GHz) are detected offset from the YSOs and are collisionally excited in the shocked regions of extended lobes of low-velocity outflows (Kurtz et al., 2004; Cyganowski et al., 2009). In contrast, class II

CH_3OH masers (e.g. 6.7 GHz) are mostly found in the immediate vicinity of HM-YSOs (e.g., Breen et al., 2013; Fujisawa et al., 2014) and are usually associated with rotating and possibly accreting disks (e.g., Bartkiewicz et al., 2009; Sugiyama et al., 2014; Motogi et al., 2017) or low-velocity outflows traced by infrared emission (De Buizer et al., 2012). The 44 GHz CH_3OH also show possible association with expending gas. In some cases, the class I CH_3OH masers (e.g. 36 and 229 GHz) and the 6.7 GHz class II CH_3OH masers show spatial overlap (e.g., in DR21(OH) Fish et al., 2011). To distinguish the origin of the Class I CH_3OH masers, wide view of 0.1-0.5 pc observed by interferometer such as ALMA is required.

1.4.3 Recent outflow studies associated with masers

Outflow activity is intimately associated with ongoing star formation. A number of outflow studies have revealed a correlation between the ejected mass, represented by the bolometric luminosity ($L_{\rm bol}$) of YSOs and the outflow properties. This relationship holds over six orders of magnitude of $L_{\rm bol}$ (e.g., Beuther et al. 2002, their Figure 4; Maud et al. 2015, their Figure 7). It is interpreted as evidence for a single outflow mechanism. However, on scales of a few 1000 au, there are poor statistics on outflow properties for stellar luminosities exceeding $10^3 L_\odot$.

Most recent and technically similar survey with the survey that this thesis used (Section 1.5 and Chapter 2), have been carrying out by Sanna et al. (2018). It is the Protostellar Outflows at the EarliesT Stages (POETS) survey with the goal of imaging the inner outflow scales of 10–100 au in a statistically-significant sample of luminous YSOs (38) to study the dynamical properties of the outflow emission in the vicinity of HM-YSOs. They are also targeting both the molecular and ionized components of the outflows by combining the kinematic information of outflow gas, obtained from the H_2O maser emission, with ejected mass, inferred from free-free continuum emission (e.g. Moscadelli et al., 2016; Sanna et al., 2016). The outflow kinematics is studied at mas scales through VLBA observations of the 22 GHz H_2O masers belonging to the Bar and Spiral Structure Legacy survey (BeSSeL; Reid et al., 2014; Reid, 2018). Sanna et al. (2018) have employed JVLA at C- (6 GHz), Ku- (13 GHz), and K-band (22 GHz) in the A- and B-Array configurations with the full width half maximum (FWHM) beams of $0''.1$–$0''.4$ to determine the spatial structure and the spectral index of the radio continuum emission and to address its nature.

Sanna et al. (2018) reported the high-resolution radio continuum images of 33 sources belonging to 25 star-forming regions. Moscadelli et al. (2019) completed the combined analysis of the radio continuum and H_2O maser observations for 25 targets, with a particular focus on the H_2O maser kinematics. The main result of Moscadelli et al. (2019) is that the 3D velocity distribution of the H_2O masers near the YSO in all samples can be interpreted in terms of a single physical scenario: a disk-wind (DW). The observed masers are produced in the different regions of the DW, from the axial collimated jet portion to the wide-angle outer layers.

Moreover, Moscadelli et al. (2020) presents a statistical analysis of the kinematic properties at mas resolution associated with 36 distinct YSOs. This is the first VLBI survey of the 22 GHz H_2O masers, based on maser positions and 3D velocities determined with an accuracy of a few mas and a few km s^{-1}, respectively. They found that the H_2O masers are a reliable proxy for the position of the YSOs (<1000 au). In addition, the distribution of maser luminosity is strongly peaked towards low values, indicating that about half of the maser population is still undetected with the current VLBI detection thresholds of 50–100 mJy beam^{-1}. They also reported 55% of the position angles of the proper motions of H_2O masers are directed on the sky within an angle of 30° from the jet axis. Finally, they showed 3D maser velocities statistically support models in which H_2O maser emission arises from planar shocks with propagation direction close to the plane of the sky. Similar statistical study is ongoing with KaVA with better spatial and spectral resolution and larger spectrum of data set combining not only H_2O maser but also CH_3OH maser (see Chapter 2).

1.5 Aims of this dissertation

To understand the circumstellar structure of HM-YSOs in the evolutionary stages of HM-YSOs that maser can trace, this thesis aims to (1) reveal the star-forming environment that the maser associated HM-YSOs have, (2) figure out the H_2O masers are excited at which part of the circumstellar structure, (3) clarify the spatial and spectral structure of outflow that can be traced by Class I CH_3OH masers.

G25.82–0.17 is chosen to achieve these goals because it is one of handful potential high-mass star-forming sites showing association with H_2O, class I CH_3OH (e.g. 44 GHz), and class II CH_3OH (e.g. 6.7 GHz) having thermal line and continuum information. Direct comparison between thermal line and continuum emission obtained with ALMA masers observed with VLBI arrays (KaVA and VERA) will provide evolutionary status of G25.82–0.17. Finding new CH_3OH masers for unique observational proof at high frequencies with ALMA (e.g. 216 GHz and 229 GHz) were done to understand the association between these masers and the HM-YSO. For this analysis, accurate positions of H_2O masers were derived by the phase referencing analysis using VERA observational data. Furthermore, parallax of H_2O masers is measured to estimate accurate distance to the target and to derive accurate physical parameters which are important to constrain further analysis by modeling. To investigate 3D velocity field of gas flow near HM-YSOs in G25.82–0.17, the proper motions of H_2O masers are measured using the KaVA monitoring data. The 3D velocity field of H_2O masers could provide information of the inner interior of outflow.

Direct observations of detailed circumstellar structures (e.g. disk-outflow system) within 10^3 au are essential for addressing evolution of individual HM-YSO and its feedback history on its parental nature which is closely connected to overall star-formation process in host protocluster as shown in this dissertation. Furthermore, source-to-source diversities of jet/outflow, disk, and envelope structures themselves also contain important suggestions on both of initial condition (angular momentum, magnetic field, etc) and evolutionary process in high-mass star formation. This dissertation also proves that H_2O and class I CH_3OH masers can trace HM-YSOs at the evolutionary stage with active accretion mode (outflows). Further similar studies to this dissertation with large samples will provide information to establish the most likely evolutionary scenario for high-mass stars.

Chapter 2

KaVA Large Program

2.1 Introduction

KaVA large program (LP) was proposed for a systematic observational study of 22 GHz H_2O and 44 GHz class I CH_3OH masers. KaVA is a combined array composed of three 21-m radio telescopes of KVN in Korea and four 20-m radio telescopes of VERA in Japan Figure 2.1. Observations of Class II CH_3OH maser at 6.7 GHz is going to be followed in the near future. Multi-epoch VLBI observations are in progress to measure proper motions of these two maser lines with KaVA. Statistical studies on quantitative properties (e.g., mass, temperature, size etc) and evolutionary stages of HM-YSOs can be done by investing spectral energy distribution (SED) based on radio/IR data set toward a large sample of HM-YSOs. The KaVA LP aims to establish an evolutionary sequence for the high-mass star formation process that can be traced by different maser species and to study the 3D velocity structures of low- and high-velocity outflows from HM-YSOs (e.g., Torrelles et al., 1997; Moscadelli et al., 2000; Goddi et al., 2005, 2011; Burns et al., 2017). In total, 87 sources with strong maser emission were selected as an initial sample based on previous single-dish surveys (e.g., Kang et al., 2015; Kim et al., 2018). Selected sample list covers the HM-YSO evolutionary phase

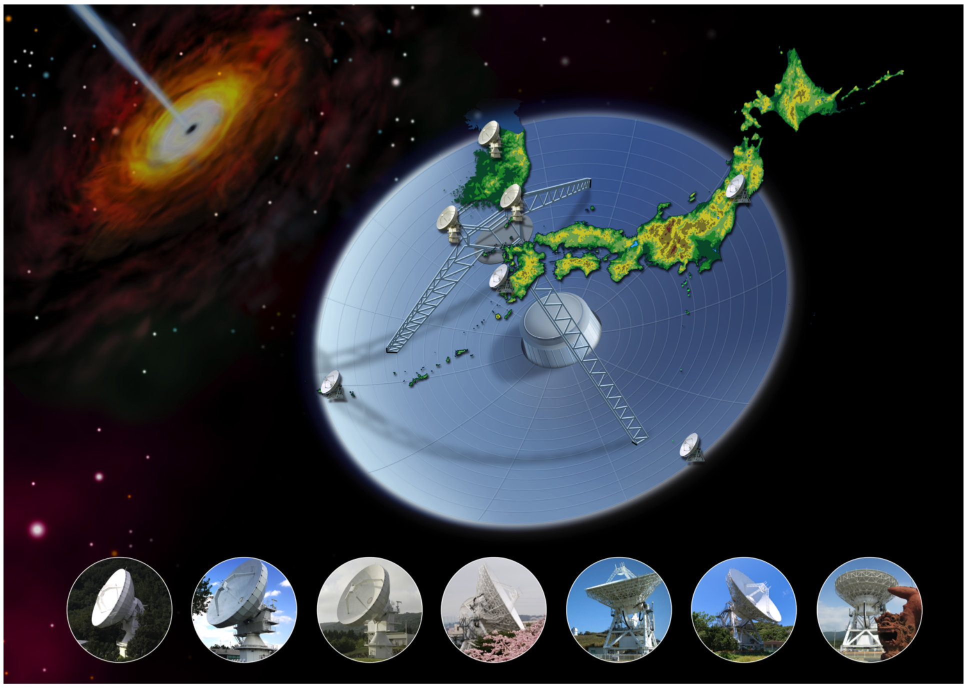

Figure 2.1: KaVA observatory.

with a dynamic range and mass range of 100. Proposed studies can be done only by using KaVA, which is capable of imaging of 22 GHz H_2O maser, 44 GHz CH_3OH maser, and 6.7 GHz CH_3OH maser (in the near future) as demonstrated by Matsumoto et al. (2014).

KaVA LP has been proposed to address key issues in high-mass star formation as summarized below. First, we will establish an evolutionary sequence of different maser species in high-mass star-formation (Figure 1.1). To achieve that comprehensive studies of the circumstellar structure toward HM-YSOs having different maser species in coherent way are essential. As already mentioned in the previous chapter, various maser species are known to be associated with HM-YSOs. However, their relationship between the central HM-YSOs and their evolution is not well established so far. Observational results from the previous studies show disagreement each other. Some of the previous observations suggested that class

I CH_3OH masers at 44 GHz appear in the earlier evolutionary stage than class II CH_3OH masers at 6.7 GHz (Ellingsen et al., 2007; Breen et al., 2010) while others proposed vice versa (Fontani et al., 2010). Inconsistency is mainly caused by observations with insufficient spatial resolution to identify masers and their powering sources.

Similar systematic surveys of 22 GHz H_2O and 6.7 GHz CH_3OH masers have been done. The spatial resolution, however, is still not enough to reveal 3D velocity structure of masers (e.g. Beuther et al., 2002b). In addition, as introduced in Section 1.4.3, POETS survey combining 3D velocity structure of H_2O maser and radio continuum emission has been done with the high angular resolutions of $0''.1$–$0''.4$ (e.g., Sanna et al., 2019; Moscadelli et al., 2019, 2020). In contrast, our survey can provide 3D velocity view traced by three maser species with 1 mas scale of resolution which is $10^2 - 10^3$ times higher than previous studies. Identifying their powering source candidates can be investigated at a scale of 1000 au (see Fujisawa et al., 2014, for 6.7 GHz CH_3OH masers). Moreover, we are going to provide radio continuum information obtained with VLA observations to investigate ionized component of outflows. The main uniqueness of KaVA LP is that direct comparison between molecular components in different scales traced by maser and other thermal line and continuum emission. It will provide not only physical properties of outflow itself but also those of driving source. It would be possible to obtain hint to understand the evolution of circumstellar structures of HM-YSOs, such as disk-outflow systems.

In addition, VLBI observations of masers is one of powerful tools to reveal possible mechanism of outflow driven by HM-YSOs. Outflows are one of the most important diagnostics of star formation in both low- and high-mass cases since they play a significant role to extract angular momentum from the hosting system. Beuther, & Shepherd (2005) predicted that initial outflows have well-collimated morphology and evolve into outflows having wide opening angles as described in Figure 2.2. On the other hand, Seifried et al. (2012) suggested that poorly-collimated outflows are driven by HM-YSOs in the early stage ($< 10^4$ yrs), and then evolve into well-collimated outflows with the Keplerian disks around the central

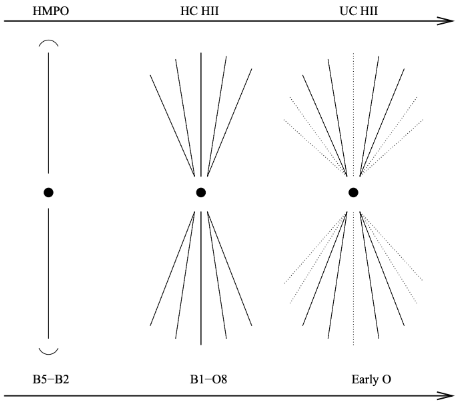

Figure 2.2: Evolutionary scenario for outflows (Beuther, & Shepherd, 2005). The evolution of an early B-type star from an HMPO via a HCHII region to an UCHII region is presented (*top*) with the evolution of an early O-type star which goes through B- and late O-type stages (*bottom*).

HM-YSOs based on their numerical simulations. It is observationally proved by Surcis et al. (2014) by VLBI observations of H_2O masers in VLA2 of W75N. Thus, it is worth establishing a scenario explaining when and how outflows having different morphology to be formed and evolved during high-mass star forming history.

2.2 Observations and Data reduction

We carried out VLBI observations from March 21, 2016, to January 12, 2016 with the KaVA toward 25 sources selected based on the KVN single dish survey. We chose the targets showing several maser components with fringe detection. The positions of the phase tracking center of the targets are listed in Table 2.1. To verify our observations, well-studied water maser samples such as AFGL 5142 (Goddi, & Moscadelli, 2006; Burns et al., 2017, e.g.,) and W51 N (Imai et al., 2002, e.g.,) are also included.

All data were calibrated in coherent way. Basically we followed general calibration for VLBI data. The total bandwidth was 256 MHz (16 MHz × 16 IFs) and recorded the left-hand circular polarization at a 1 Gbps sampling rate. We analyzed only one of the 16 MHz IF channels assigned to the H_2O $6_{1,6}$-$5_{2,3}$ transition. The spectral resolution is 15.625 kHz (~0.21 km s $^{-1}$) for the H_2O maser line. The correlation process was carried out at the Korean-Japan Correlation Center, Daejeon, Korea (KJCC: Lee et al., 2015). Extragalactic radio continuum sources, NRAO 530, DA193, and BALLAC, were employed for bandpass and delay calibration. KaVA data calibration was carried out using the Astronomical Image Processing System (AIPS) developed by National Radio Astronomy Observatory (NRAO)[1] (van Moorsel et al., 1996). Measured system temperatures were delivered with the correlated data. First, gains were calibrated by using the AIPS task APCAL using measured system temperatures. Next, delays and phase offsets were removed by running AIPS task FRING using aforementioned calibrators. Bandpass response was also calibrated using the same calibrators. Fringe fitting was done on a reference maser component having the highest intensity in each source spectrum. Imaging and CLEAN (deconvolution) were performed using the AIPS task IMAGR. We set the cell size of image as 0.2 mas and the pixel number of each axis as 4096.

2.3 Results and Discussion

2.3.1 Spectral distributions of H_2O masers

Water masers were detected toward 20 sources among 25 including well-known targets such as G174.20-0.07 (AFGL 5142) and G49.49-0.37 (W51 N). As shown in from Figure 2.5 to Figure 2.9, spectral distributions of H_2O masers show source to source variation (Figure 2.3). They have different numbers of different velocity components from one or two features of masers (ΔV< 10 km s^{-1}; e.g. G11.95-0.16 and G30.41-0.23) to 62 features (ΔV> 100 km s^{-1};

---

[1] http://www.aips.nrao.edu/index.shtml

Table 2.1. KaVA Observations for Imaging Survey

Source name	R.A. ($^{h\ m\ s}$)	Dec. ($^{\circ\ \prime\ \prime\prime}$)	$V_{\rm lsr}$ (km s^{-1})	D (kpc)	Detection	Identifier
G357.97-0.16	17:41:20.24	-30:45:08.00	-5	···	Y	G357.967N
G351.77-0.53	17:26:42.57	-36:09:09.6	1	2.2[a]	Y	
G351.24+0.67	17:20:17.76	-35:54:42.8	3	1.34[b]	Y	
G192.58-0.04	06:12:53.6	+18:00:25.10	11	1.59[b]	Y	S255N
G174.20-0.07	05:30:48.0	+33:47:54.00	-3	2.13[c]	Y	AFGL 5142
G49.49-0.39	19:23:43.96	+14:30:31.00	59	5.41[b]	Y	
G49.49-0.37	19:23:40.00	+14:30:51.00	60	5.13[b]	Y	W51 N
G45.07+0.13	19:13:22.06	+10:50:53.60	58	8.00[b]	Y	
G35.19-0.74	18:58:13.10	+01:40:35.00	29	2.19[b]	Y	IRAS 18556+0136
G34.26+0.15	18:53:18.66	+01:14:57.70	55	···	Y	
G33.42-0.00	18:52:19.70	+00:25:47.00	43	···	N[d]	IRAS 18497+0022
G30.82-0.05	18:47:46.80	-01:54:36.00	96	···	Y	
G30.41-0.23	18:47:38.95	-02:20:51.80	43	···	Y	RMS 3158
G28.39+0.08	18:42:51.97	-03:59:54.00	77	···	N[d]	G28.37+0.07 MM1
G25.82-0.17	18:39:03.63	-06:24:09.50	94	···	Y	
G25.38-0.15	18:38:08.14	-06:46:52.98	39	···	N[d]	JCMT 18354
G19.61-0.14	18:27:16.00	-11:53:53.00	77	···	N[d]	IRAS 18244-1155
G18.34+1.78	18:17:49.95	-12:08:06.48	30	···	Y	G18.34+1.78SW
G16.93+0.96	18:18:08.62	-13:45:07.00	20	···	Y	RMS 2547
G13.87+0.28	18:14:35.83	-16:45:35.90	48	3.94[b]	Y	
G12.88+0.48	18:11:51.40	-17:31:29.60	39	2.50[b]	Y	
G11.95-0.16	18:12:21.00	-18:39:35.00	1	···	Y	IRAS 18094-7840
G10.62-0.38	18:10:28.56	-19:55:49.50	-2	4.95[b]	Y	IRAS 18075-1956
G10.47+0.03	18:08:38.10	-19:51:50.00	75	8.55[b]	Y	IRAS 18056-1952
G10.34-0.14	18:09:00.00	-20:03:35.0	4	···	···[d]	

[a] Trigonometric distance to G351.77-0.53 (Norris et al., 1993).

[b] Distances determined by measuring trigonometric parallaxes (Reid et al., 2014).

[c] Trigonometric distance to G174.20-0.07 (AFGL 5142) (Burns et al., 2017).

[d] Non-detection.

e.g. G49.49-0.39). In addition, toward G351.77-0.53 and G357.97-0.16, extremely blueshifted H_2O masers were successfully detected with KaVA as we expected (Figure 2.5). We note that this snapshot imaging survey is for finding appropriate target for monitoring observations. Therefore, we excluded targets showing only one or two components and non-detection (e.g. G11.95-0.16 and G33.42-0.00) for further analysis. In addition, during the KaVA snapshot imaging survey observation period, monitoring observations have been already started toward the G351.77-0.53 and G357.97-0.16. Thus, data for these two targets was also not used. One of well-known targets (G49.49-0.37; W51 N) was not included because the verification process was done with the other target, G174.20-0.07 (AFGL 5142). The water maser data toward 15 sources were analyzed.

A maser 'spot' refers to an individual maser emission peak in a spectral channel while a maser 'feature' denotes a group of maser spots considered to exist within the same maser cloudlet and located physically close to each other. The peak positions of maser spots were derived by Gaussian fitting to the individual channel images using the AIPS task SAD. We employed image pixels greater than 5σ noise levels of each images for the Gaussian fitting to distinguish maser spots from side lobes. Firstly, we identified maser feature which was detected at least in two channels. Secondly, a representative maser spot was defined by comparing the maser intensities of each spot in the individual channels. Therefore, we selected a spot having the highest intensity among maser spots within one feature as a representative spot.

We classified spectra into three groups according to the spectral distribution of H_2O maser features. Blue shifted dominant sources are classified as "blue" while red shifted dominant sources are named as "red". Both blue and red shifted components were detected toward most of sources. They are classified as "both". Water maser spectra show various profiles source by source as expected. The systemic velocities of each source adopted from the previous thermal molecular line surveys (e.g., Urquhart et al., 2011; Shirley et al., 2013). Although it strongly depends on the definition of the systemic velocities of each target, 3 sources

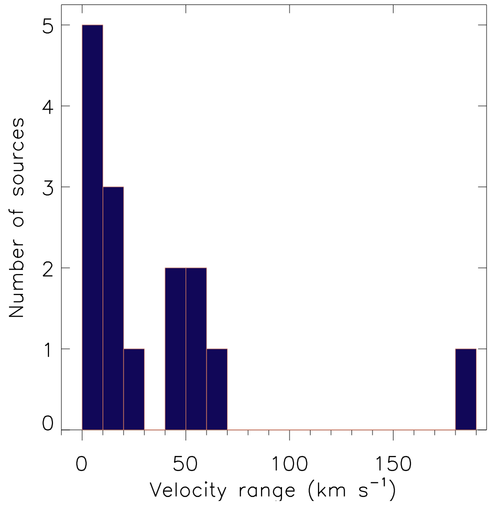

Figure 2.3: Velocity range distribution of detected H_2O maser features.

were classified as “blue" , 2 were “red”, and 10 sources were classified as “both" among 15 H_2O maser sources. The H_2O masers having both components are highly expected to trace bipolar outflows and isotropically expanding shells/winds in the vicinity of H_2O maser hosting source. In addition, there is a possibility that H_2O masers are tracing only one side of outflow (blue- or redshifted lobe only). Therefore, monitoring observations for all detected H_2O masers are required to clarify the motion of these masers.

2.3.2 Spatial distributions of H_2O masers

We started to analyze H_2O maser maps toward sources for which VLBI images are already available to compare with the previous results. For example, we compared water maser maps of G174.20-0.07 (AFGL 5142) from this work (Figure 2.8 (a) and (b)) and Burns et al. (2017, ; see Figure 2 (Figure 2.4) and Figure 3). Water maser observations in Burns et al. (2017) were conducted with VERA. Even though there is time gap between observations in this work and Burns et al. (2017), most of main H_2O maser features reported by Burns et

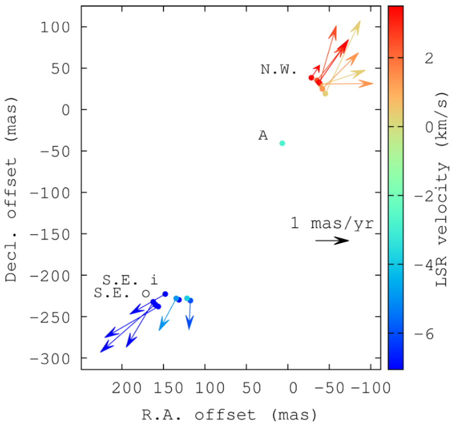

Figure 2.4: Internal motions of H_2O masers in G174.20-0.07 (AFGL 5142). Vectors indicate proper motion having the same velocities in the color bar. Detailed information of annotations are listed in Table 2 of Burns et al. (2017).

al. (2017) were shown in the KaVA map such as N.W., S.E. (i and o), and F.S. feature. In addition, the central A component was also detected. The red shifted feature at (0,0) in the map presents small velocity gradient inside the arc-like structure. This arc-structure has been reported by Burns et al. (2017) which may trace bow shock. Bow shock is known as signpost of the interaction between the outflow driven by the central protostar and the dense envelope. Moreover, another NW feature that was not shown in Burns et al. (2017) was detected located outer region than N.W. feature. It cannot be ruled out that H_2O masers can be newly excited by chance, however, better sensitivity of KaVA may catch the weaker H_2O maser feature that cannot be detected with VERA only. If it is the case, this may trace the previous accretion if the accretion occurs in AFGL 5142 episodically because the ejection from the protostar is closely connected to the accretion to the protostar. Using the verified analysis method, H_2O maser distribution maps were made for rest of the observed sources.

In addition to the classification by spectra, H_2O maser distribution is also classified by their spatial distribution. As already mentioned above, the H_2O masers in “both” group are highly expected to trace bipolar outflows and isotropically expanding shells/winds. Therefore, 10 targets classified as “both” group are largely divided into two groups: a “compact” distribution group and an “elongated” distribution group. “Compact” and “elongated” are defined based on morphology of H_2O maser distribution. To investigate the trend in the distribution of H_2O masers, morphology factor was defined as $\alpha = l_{\max}/l_{\min}$ where $l_{\max}$ and $l_{\min}$ are major and minor size of H_2O maser distribution, respectively. The major size is estimated from the distribution map regarding the axis roughly connecting blue- and redshifted components while the minor size defined as the maximum distance of maser feature from the major axis. Since accurate distance information is not estimated for all source, direct comparison between the linear scale is not available. However, the ratio of major and minor length (morphology factor) provides a hint on the morphology of H_2O maser distribution source to source. Estimated morphology ratio is listed in subsection 2.3.3.

To minimize the effect from H_2O masers from different driving sources, H_2O maser features distributed in the central region of the each map ($1'' \times 1''$) are employed. We classified spatial distributions of H_2O masers using the median value of morphology factor of 0.18. Five sources, including G25.82–0.17 one of the targets having the large morphology ratio (~0.4), are classified as “compact” while the others are in “elongated” group.

2.3.3 Source selection for KaVA monitoring observations

Toward targets, such as G34.26+0.15, G30.82-0.05, and G25.82-0.17, classified as “both”, several tens of features (50-60) were detected with several tens of velocity ranges (50-60 km s^{-1}). These targets are a good laboratory to investigate the connection between the dynamical structures in the vicinity of the powering source and H_2O maser 2D and 3D distributions. The difference in H_2O maser distribution would be caused by different dynamical structures in the vicinity of the hosting objects. Elongated structure may trace bipolar outflows with high possibility while compact structure is hard to imagine what kinds of dynamical structures can be traced. To examine the environmental difference between these two groups, the 3D

Table 2.2. Spectral and spatial distributions of detected H_2O masers

Source name	velocity range (km s^{-1})	Number of features	Spectral classification	Morphology	Spatial Classification
G351.24+0.67	14	14	Red	···	···
G192.58-0.04	7	8	Blue	···	···
G174.20-0.07	10	20	Both	0.12	Compact
G49.49-0.39	180	62	Both	0.16	Compact
G45.07+0.13	9	14	Both	0.22	Elongated
G35.19-0.74	4	11	Both	0.07	Compact
G34.26+0.15	64	46	Both	0.41	Elongated
G30.82-0.05	48	53	Both	0.20	Elongated
G25.82-0.17	57	57	Both	0.40	Elongated
G18.34+1.78	46	7	Both	0.17	Compact
G16.93+0.96	6	5	Blue	···	···
G13.87+0.28	11	3	Red	···	···
G12.88+0.48	9	2	Blue	···	···
G10.62-0.38	24	21	Both	0.09	Compact
G10.47+0.03	58	12	Both	0.20	Elongated

velocity structures of H_2O masers are going to be obtained with monitoring observations.

Therefore, G25.82-0.17, one of targets having the largest morphology factor of ~0.4, is selected for the first case study from the KaVA LP as a first step to KaVA LP ultimate goals because it has a larger scale of view obtained with ALMA while the other source does not have. Based on the results from the KaVA imaging survey, KaVA monitoring observations were done including G25.82-0.17 (see Appendix A).

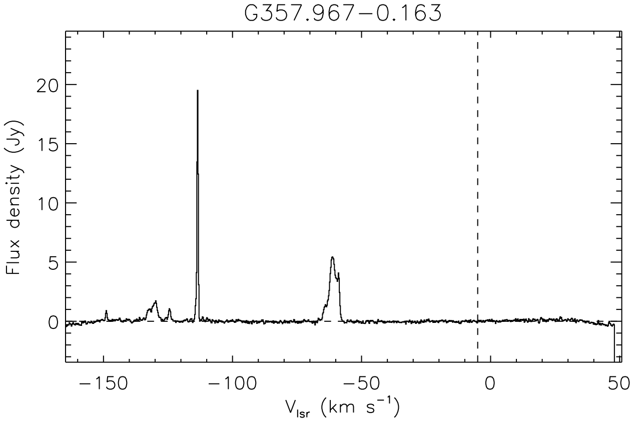

(a)

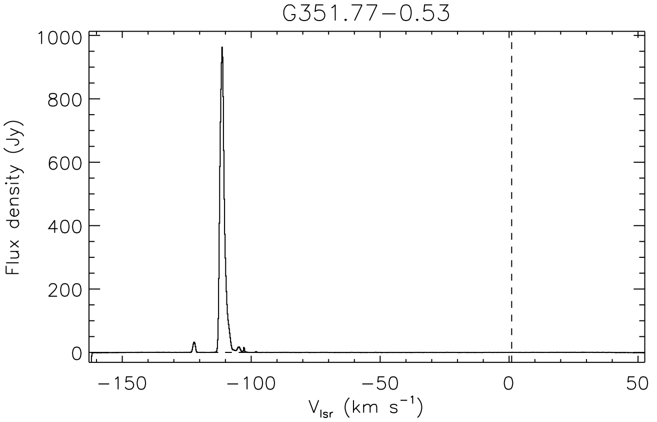

(b)

Figure 2.5: The 22 GHz H_2O maser spectrum toward (a) G357.97-0.16 (G357.967N) and (b) G351.77-0.53. The vertical dashed line and the horizontal dashed line represent the systemic velocity of source and zero baseline, respectively.

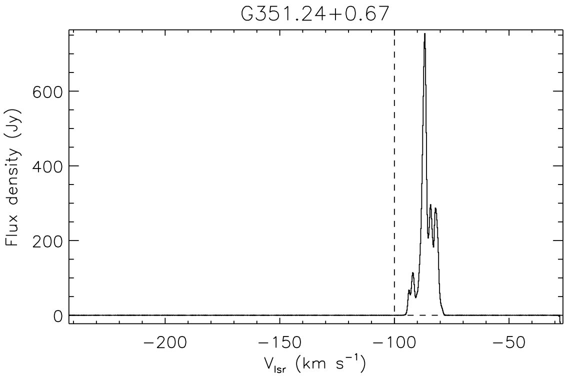

(a)

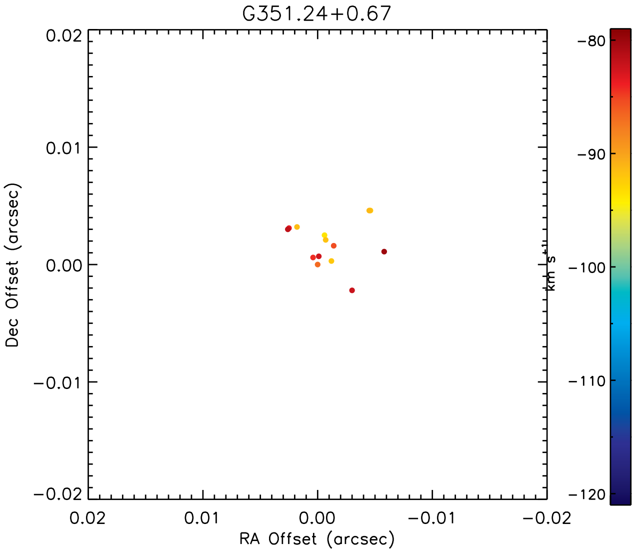

(b)

Figure 2.6: (a) The 22 GHz H_2O maser spectrum toward G351.24+0.67. The vertical dashed line and the horizontal dashed line represent the systemic velocity of source and zero baseline, respectively. (b) Distribution of H_2O masers toward G351.24+0.67. Filled circles denote H_2O maser spots having the same velocities in the color bar. The reference position (0,0) is the position of the strongest maser spot in the spectrum.

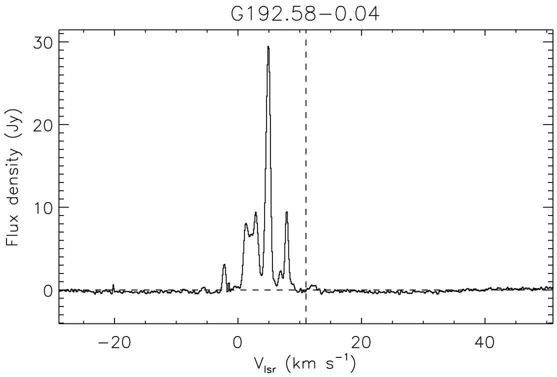

(a)

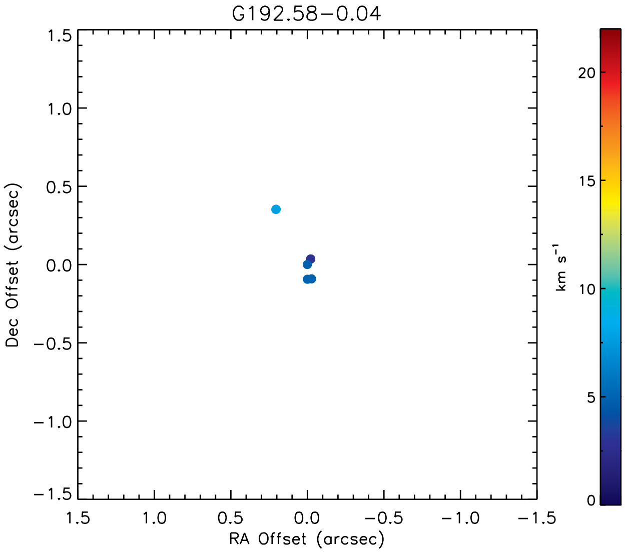

(b)

Figure 2.7: (a) The 22 GHz H_2O maser spectrum toward G192.58-0.04 (S255 N). The vertical dashed line and the horizontal dashed line represent the systemic velocity of source and zero baseline, respectively. (b) Distribution of H_2O masers toward G192.58-0.04 (S255 N). Filled circles denote H_2O maser spots having the same velocities in the color bar. The reference position (0,0) is the position of the strongest maser spot in the spectrum.

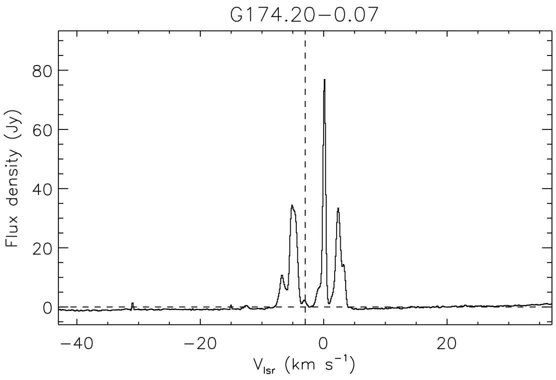

(a)

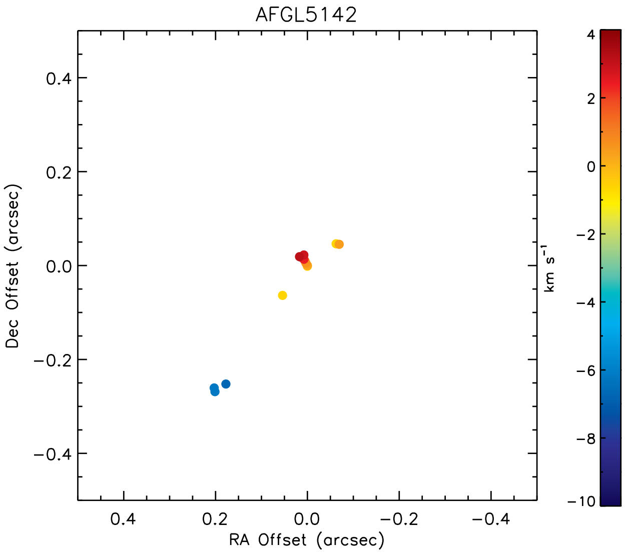

(b)

Figure 2.8: (a) The 22 GHz H_2O maser spectrum toward G174.20-0.07 (AFGL 5142). The vertical dashed line and the horizontal dashed line represent the systemic velocity of source and zero baseline, respectively. (b) Distribution of H_2O masers toward G174.20-0.07 (AFGL 5142). Filled circles denote H_2O maser spots having the same velocities in the color bar. The reference position (0,0) is the position of the strongest maser spot in the spectrum.

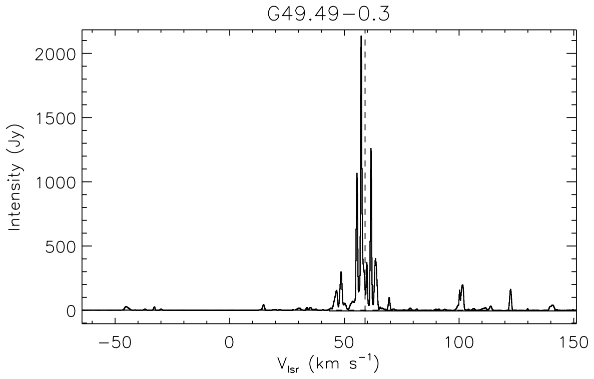

(a)

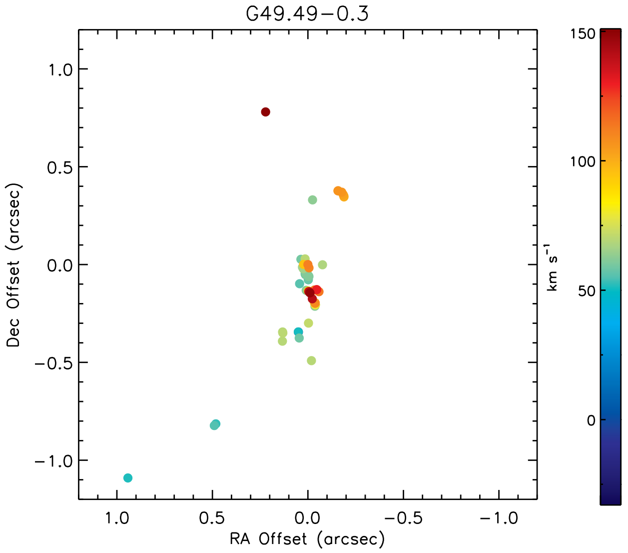

(b)

Figure 2.9: (a) The 22 GHz H_2O maser spectrum toward G49.49-0.39. The vertical dashed line and the horizontal dashed line represent the systemic velocity of source and zero baseline, respectively. (b) Distribution of H_2O masers toward G49.49-0.39. Filled circles denote H_2O maser spots having the same velocities in the color bar. The reference position (0,0) is the position of the strongest maser spot in the spectrum.

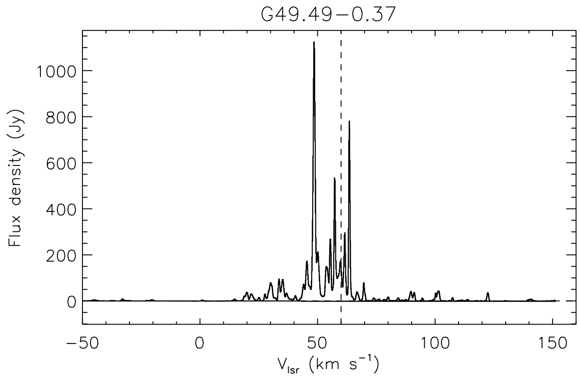

Figure 2.10: The 22 GHz H_2O maser spectrum toward G49.49-0.37 (W51d). The vertical dashed line is the systemic velocity while the horizontal dashed lines represent the zero baseline.

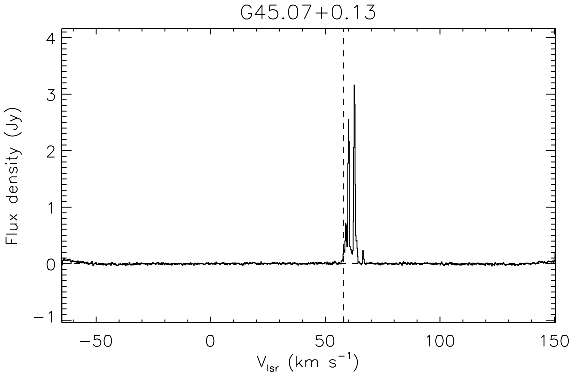

(a)

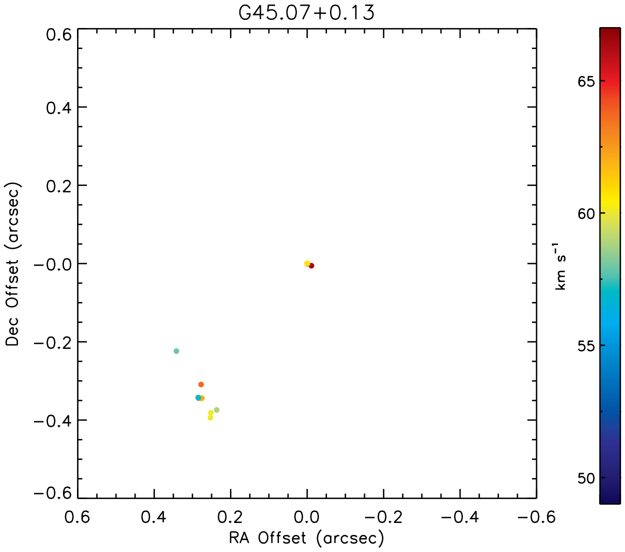

(b)

Figure 2.11: (a) The 22 GHz H_2O maser spectrum toward G45.97+0.13. The vertical dashed line and the horizontal dashed line represent the systemic velocity of source and zero baseline, respectively. (b) Distribution of H_2O masers toward G45.07+0.13. Filled circles denote H_2O maser spots having the same velocities in the color bar. The reference position (0,0) is the position of the strongest maser spot in the spectrum.

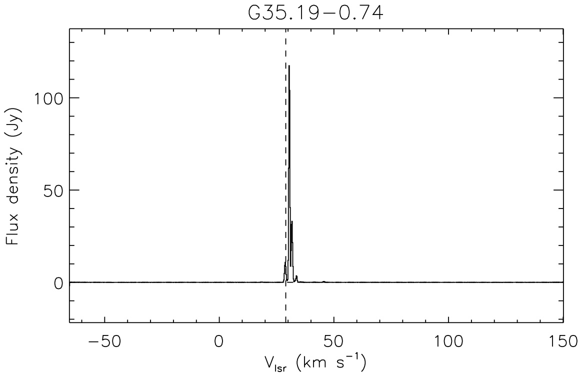

(a)

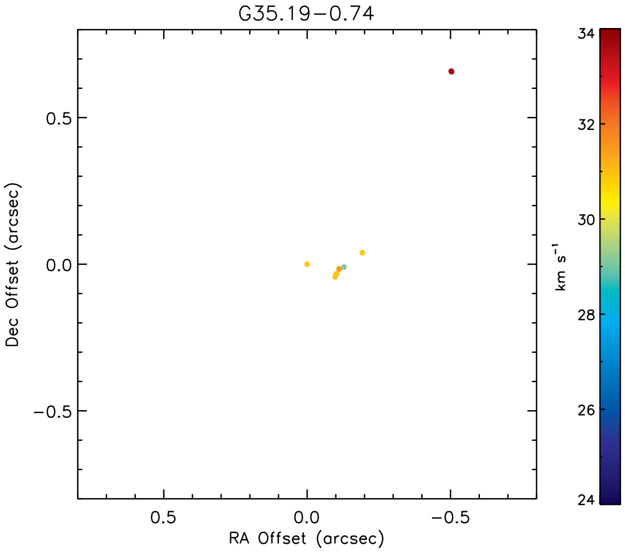

(b)

Figure 2.12: (a) The 22 GHz H_2O maser spectrum toward G35.19-0.74 (IRAS 18556+0136). The vertical dashed line and the horizontal dashed line represent the systemic velocity of source and zero baseline, respectively. (b) Distribution of H_2O masers toward G35.19-0.74 (IRAS 18556+0136). Filled circles denote H_2O maser spots having the same velocities in the color bar. The reference position (0,0) is the position of the strongest maser spot in the spectrum.

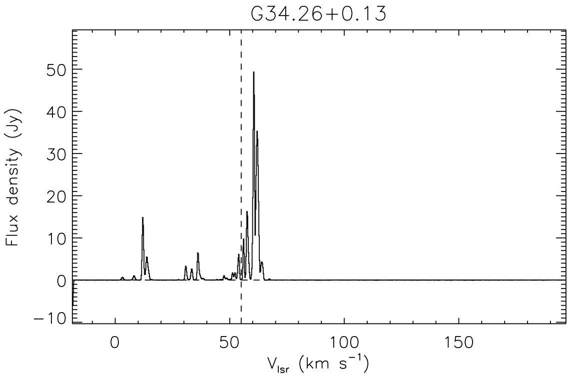

(a)

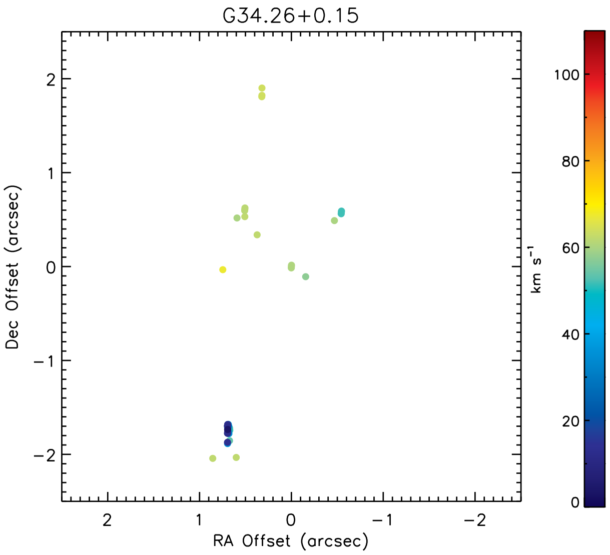

(b)

Figure 2.13: (a) The 22 GHz H_2O maser spectrum toward G34.26+0.15. The vertical dashed line and the horizontal dashed line represent the systemic velocity of source and zero baseline, respectively. (b) Distribution of H_2O masers toward G34.26+0.15. Filled circles denote H_2O maser spots having the same velocities in the color bar. The reference position (0,0) is the position of the strongest maser spot in the spectrum.

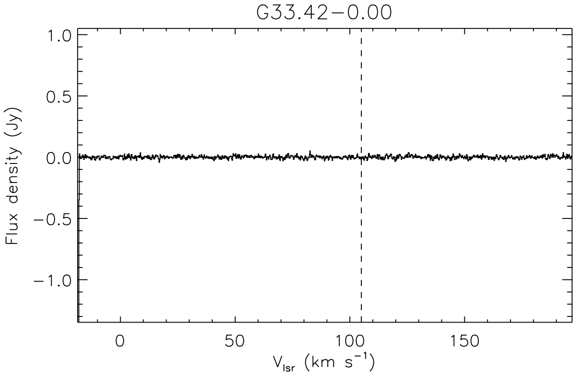

Figure 2.14: The 22 GHz H_2O maser spectrum toward G33.42-0.00 (IRAS 18497+0022). The vertical dashed line is the systemic velocity while the horizontal dashed lines represent the zero baseline.

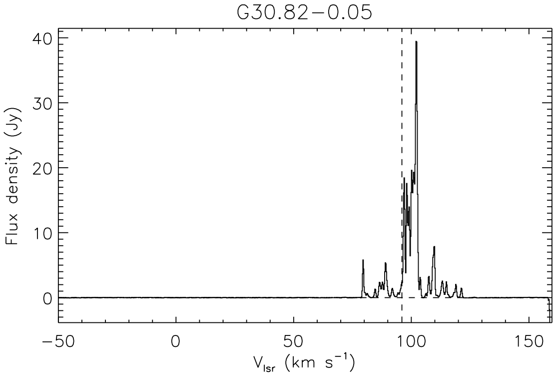

(a)

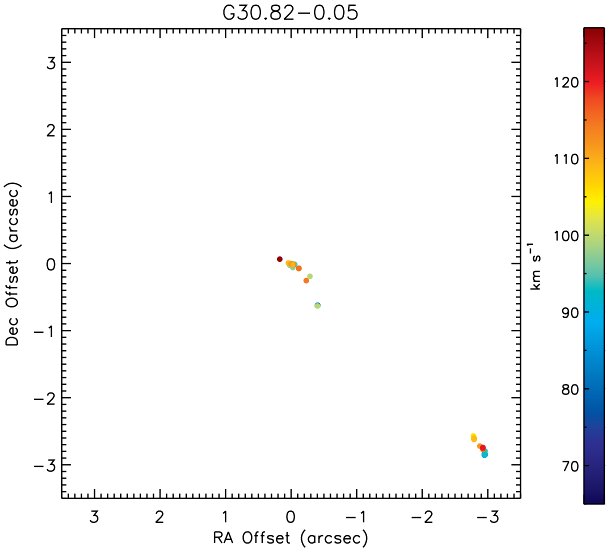

(b)

Figure 2.15: (a) The 22 GHz H_2O maser spectrum toward G30.82-0.05. The vertical dashed line and the horizontal dashed line represent the systemic velocity of source and zero baseline, respectively. (b) Distribution of H_2O masers toward G30.82-0.05. Filled circles denote H_2O maser spots having the same velocities in the color bar. The reference position (0,0) is the position of the strongest maser spot in the spectrum.

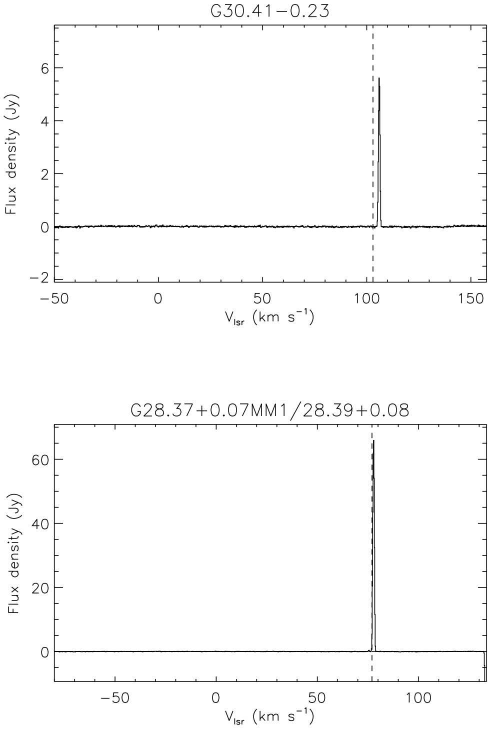

(a)

(b)

Figure 2.16: The 22 GHz H_2O maser spectrum toward (a) G30.41-0.23 (RMS 3158) and (b) G28.37+0.08 (G28.37+0.07MM1). The vertical dashed line and the horizontal dashed line represent the systemic velocity of source and zero baseline, respectively.

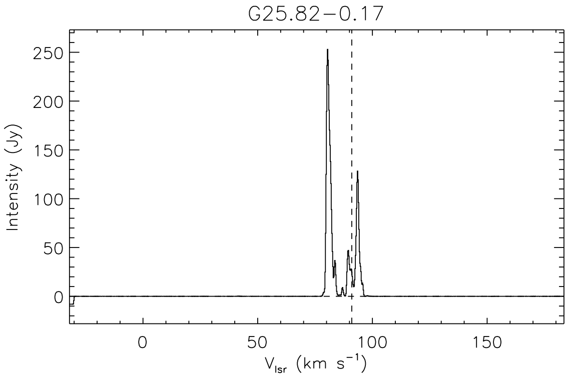

(a)

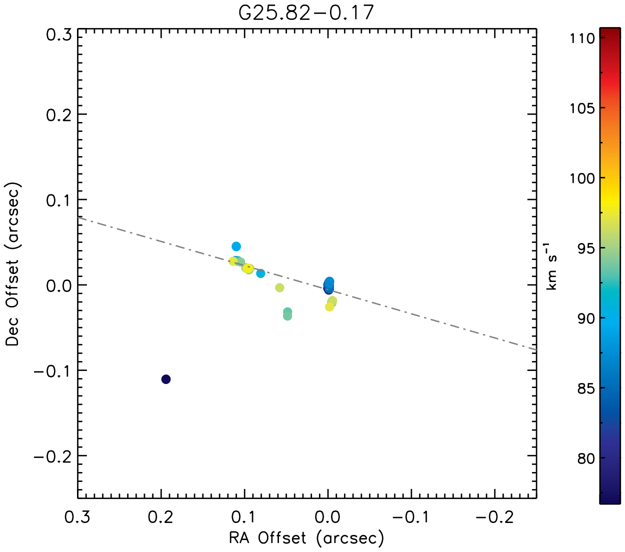

(b)

Figure 2.17: (a) The 22 GHz H_2O maser spectrum toward G25.82-0.17. The vertical dashed line and the horizontal dashed line represent the systemic velocity of source and zero baseline, respectively. (b) Distribution of H_2O masers toward G25.82-0.17. Filled circles denote H_2O maser spots having the same velocities in the color bar. The reference position (0,0) is the position of the strongest maser spot in the spectrum.

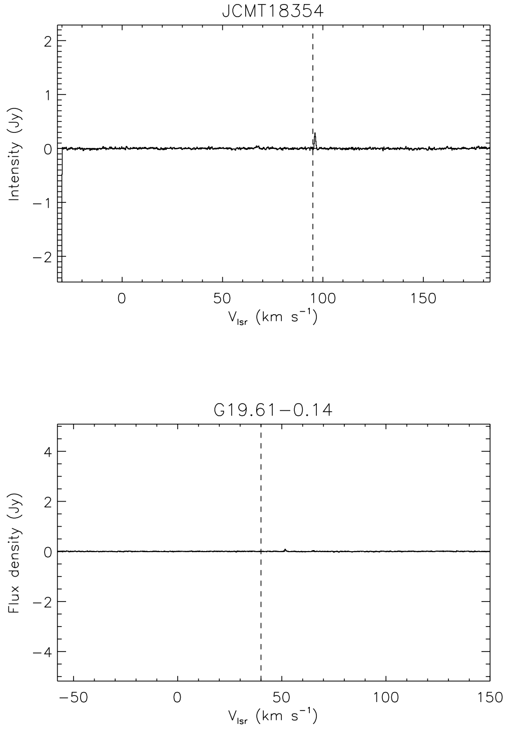

(a)

(b)

Figure 2.18: The 22 GHz H_2O maser spectrum toward (a) G25.38-0.15 (JCMT 18354) and (b) G19.61-0.14 (IRAS 18244-1155). The vertical dashed line and the horizontal dashed line represent the systemic velocity of source and zero baseline, respectively.

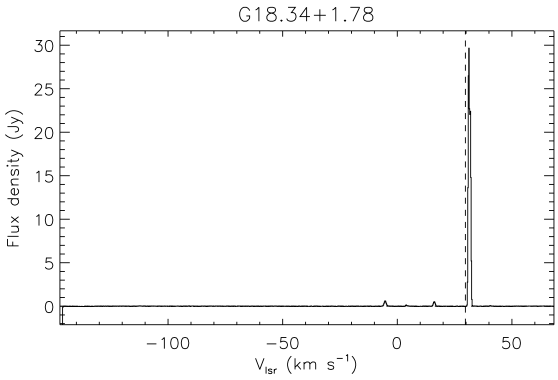

(a)

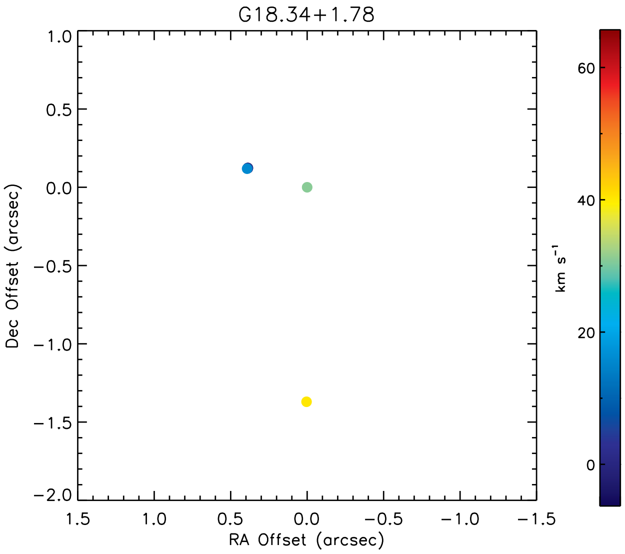

(b)

Figure 2.19: (a) The 22 GHz H_2O maser spectrum toward G18.34+1.78 (G18.34+1.78SW). The vertical dashed line and the horizontal dashed line represent the systemic velocity of source and zero baseline, respectively. (b) Distribution of H_2O masers toward G18.34+1.78SW. Filled circles denote H_2O maser spots having the same velocities in the color bar. The reference position (0,0) is the position of the strongest maser spot in the spectrum.

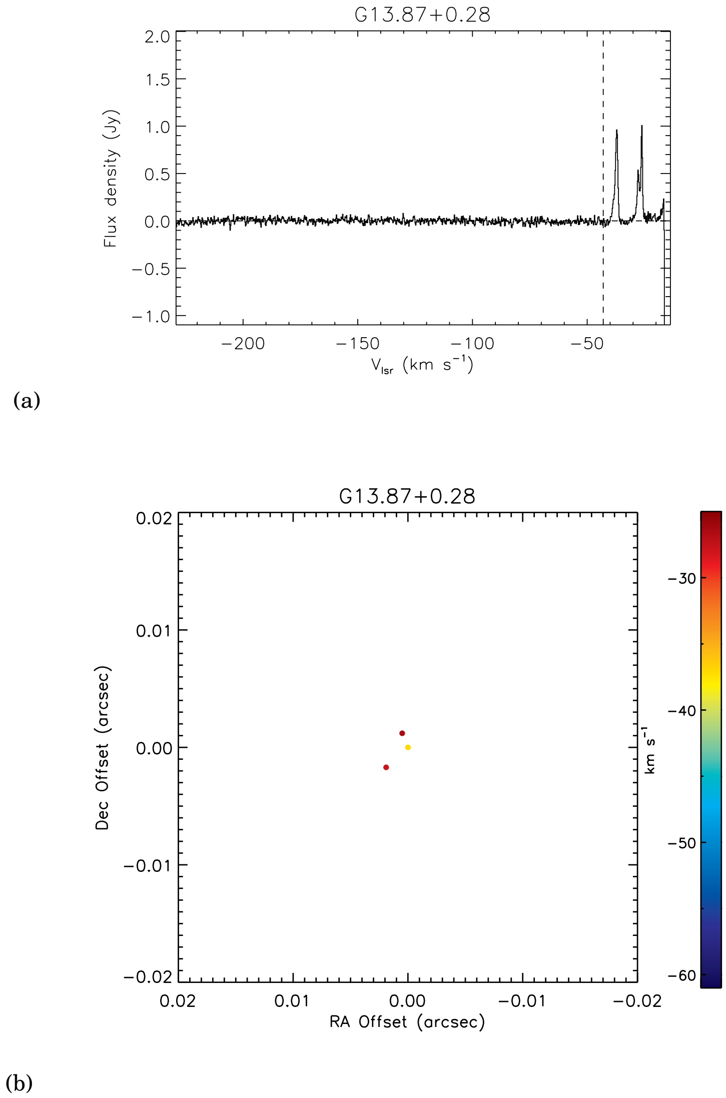

Figure 2.20: (a) The 22 GHz H_2O maser spectrum toward G13.87+0.28. The vertical dashed line and the horizontal dashed line represent the systemic velocity of source and zero baseline, respectively. (b) Distribution of H_2O masers toward G13.87+0.28. Filled circles denote H_2O maser spots having the same velocities in the color bar. The reference position (0,0) is the position of the strongest maser spot in the spectrum.

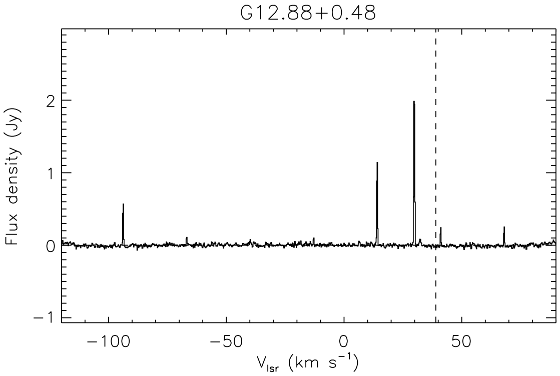

(a)

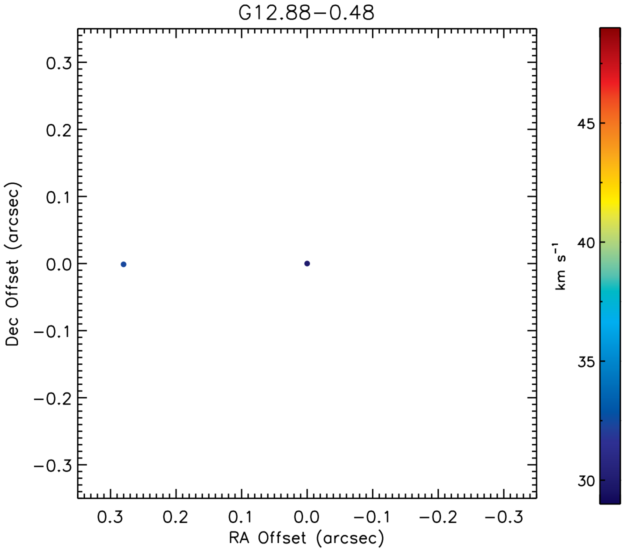

(b)

Figure 2.21: (a) The 22 GHz H_2O maser spectrum toward G12.88+0.48. The vertical dashed line and the horizontal dashed line represent the systemic velocity of source and zero baseline, respectively. (b) Distribution of H_2O masers toward G12.88+0.48. Filled circles denote H_2O maser spots having the same velocities in the color bar. The reference position (0,0) is the position of the strongest maser spot in the spectrum.

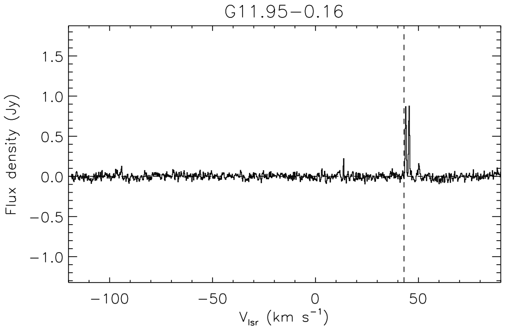

Figure 2.22: The 22 GHz H_2O maser spectrum toward G11.95-0.16 (IRAS 18094-1840). The vertical dashed line is the systemic velocity while the horizontal dashed lines represent the zero baseline.

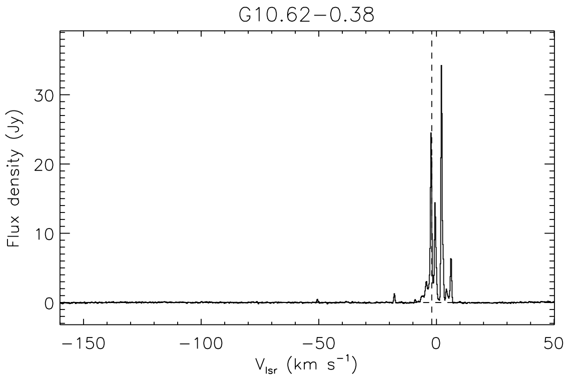

(a)

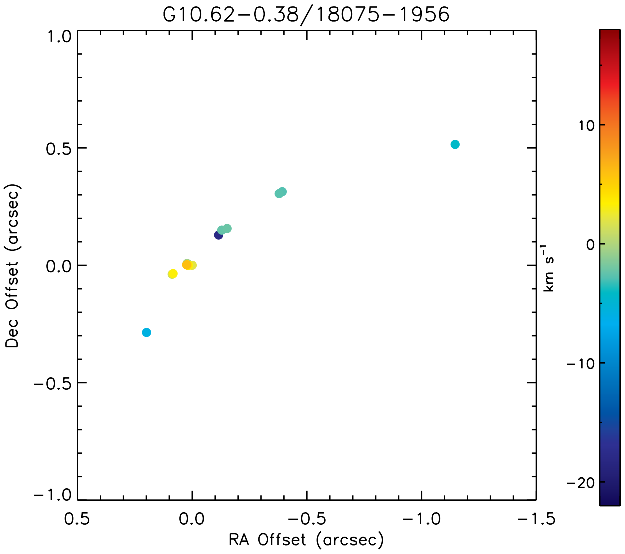

(b)

Figure 2.23: (a) The 22 GHz H_2O maser spectrum toward G10.62-0.38 (IRAS 18075-1956). The vertical dashed line and the horizontal dashed line represent the systemic velocity of source and zero baseline, respectively. (b) Distribution of H_2O masers toward IRAS 18075-1956. Filled circles denote H_2O maser spots having the same velocities in the color bar. The reference position (0,0) is the position of the strongest maser spot in the spectrum.

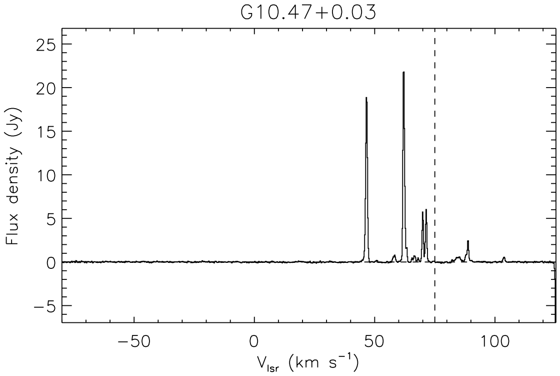

(a)

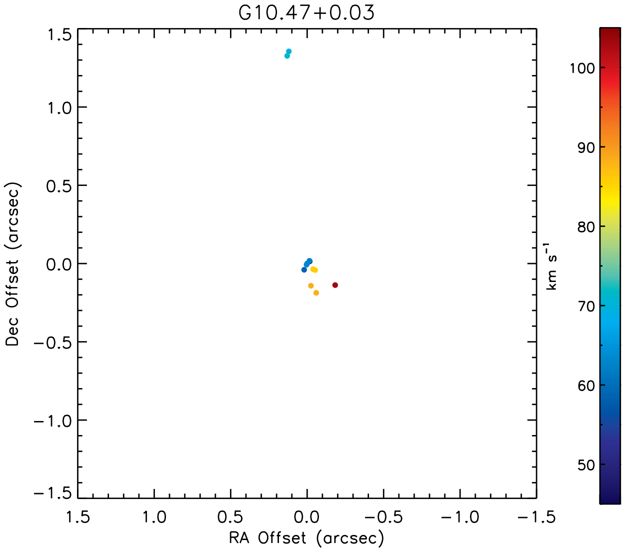

(b)

Figure 2.24: (a) The 22 GHz H_2O maser spectrum toward G10.47+0.03 (IRAS 18056-1952). The vertical dashed line and the horizontal dashed line represent the systemic velocity of source and zero baseline, respectively. (b) Distribution of H_2O masers toward IRAS 18065-1952. Filled circles denote H_2O maser spots having the same velocities in the color bar. The reference position (0,0) is the position of the strongest maser spot in the spectrum.

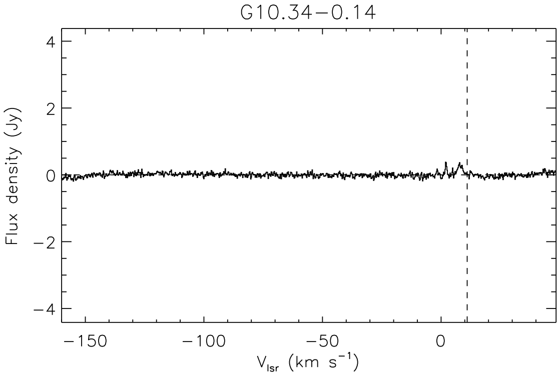

Figure 2.25: The 22 GHz H_2O maser spectrum toward G10.34-0.14. The vertical dashed line is the systemic velocity while the horizontal dashed lines represent the zero baseline.

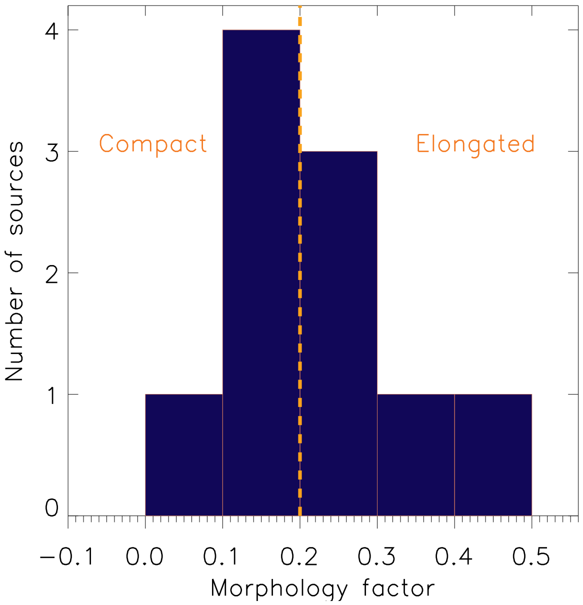

Figure 2.26: Ratios of the major and minor sizes of H_2O maser distributions. Red dotted line denotes the median ratio of major and minor sizes used as the standard to classify sources in two groups according to the spatial distribution.

Chapter 3

Trigonometric distance and proper motions of H_2O masers in G25.82–0.17

3.1 Introduction

For masers tracing outflowing gas and/or rotating/infalling gas motions in circumstellar disks around YSOs, proper motions are expected. For example, masers moving with velocities $\geq$ 10 km s^{-1} will result in proper motions $\geq$ 0.4 mas/year for a source at a distance at 5000 pc. These proper motions can be measured only through VLBI multi-epoch observations. Measurement of proper motions of masers provides 3D velocity field of gas surrounding HM-YSOs. In general, proper motion measurements of H_2O masers are limited by strong time variability of their intensity (e.g. Brand et al., 2003). However, the very high angular resolution of the VLBI observations allows to use short time intervals of a few weeks, therefore minimizing the time-dependent effects. In addition, by measuring parallax of H_2O masers, distance to the source can be estimated which is important physical parameter to constrain other physical properties such as source mass. In other word, to investigate physical properties of YSOs, accurate distance to the source is essential.

3.2 G25.82–0.17

This region is weak or dark at infrared wavelengths (e.g., *Wide-field Infrared Survey Explorer* (WISE); Wright et al., 2010). However, a large scale ^{13}CO outflow has been reported with the James Clerk Maxwell Telescope (JCMT), indicating that G25.82–0.17 is a potential site of high-mass star formation (de Villiers et al., 2014). In addition, both 6.7 GHz CH_3OH and 12 GHz CH_3OH masers were detected (e.g., Walsh et al., 1998; Błaszkiewicz & Kus, 2004; Breen et al., 2015, 2016; Hu et al., 2016; Surcis et al., 2019), strongly suggesting the existence of a HM-YSO close to the CH_3OH maser site as the 6.7 GHz CH_3OH maser is exclusively associated with HM-YSOs (Breen et al., 2013). Thus, G25.82–0.17 is a suitable target for a detailed study of the HM-YSO(s) associated with outflow and possibly disk through high resolution maser observations. The systemic velocity of G25.82–0.17 is 93.7 km s^{-1} from ammonia (the NH_3 (1,1) line) observations using the Effelsberg 100 m telescope (Wienen et al., 2012), with a corresponding kinematic distance of 5 ± 0.3 kpc (Green & McClure-Griffiths, 2011). Hereafter, we will refer to our target, G25.82–0.17, as G25.82 for simplicity.

We carried out H_2O maser monitoring observations toward G25.82 with VERA and KaVA simultaneously to take full advantages of both arrays at the same time. The fluctuation of atmosphere is one of significant error sources which can be effectively canceled out using the unique dual-beam system of VERA (Honma et al., 2008a). Then VERA can measure the absolute positions of maser sources by measuring relative positions with respect to the reference sources with high accuracy. Such VLBI technique is the 'phase-referencing'. In the case of KaVA, additional shorter baselines, compared to VERA only, fill up the UV coverage resulting in better sensitivity to detect weak maser spots as much as we can. To obtain 3D velocity structure of masers, more features provide better 3D view of course. These are why

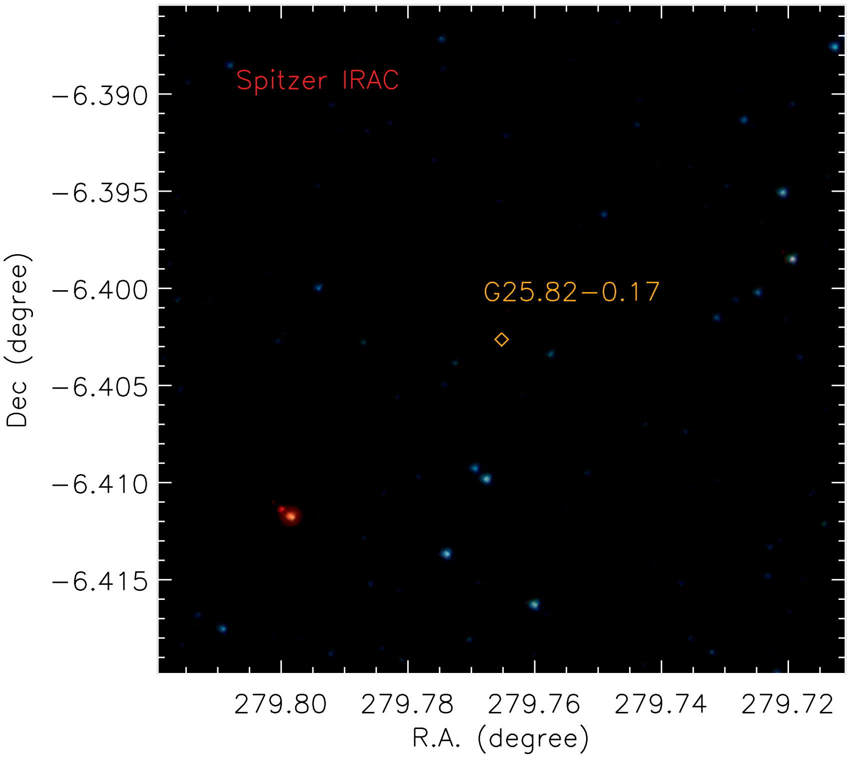

Figure 3.1: *Spitzer* three-color composite image in the vicinity of G25.82–0.17. Blue, green, and red are presented the IRAC 3.6, 4.5, and 8.0 μm, respectively. Orange open-diamond denotes the tracking position for G25.82–0.17.

VERA and KaVA observations are essential for each own purpose.

3.3 Observations and Data Analysis

3.3.1 VERA Observations

We carried out intensive H_2O maser monitoring observations toward G25.82 to measure the parallax and derive absolute positions of H_2O maser features. In total, 7 epochs of 1 Giga-bit-per-second (Gbps) observations and 10 epochs of 4 Gbps observations were carried out. The dual-beam phase-referencing mode was used for these observations (Honma et al., 2008a), in which the target source, G25.82, and a phase calibrator, J1846-0651, were observed simultaneously. The A-beam was assigned to observe our target while the B-beam was set toward the phase reference source. This method is used to derive accurate absolute positions of the H_2O maser spots. The phase reference center for G25.82 was (α,δ)=($18^h39^m03^s.63$, -06°24′09.05″), while that for J1846-0651 was (α,δ)=($18^h46^m03^s.300384$, -06°51′27.74731″). The position of J1846-0651 was from VLBA calibrator list [1]. Observation setting was changed during the monitoring period from 1 Gbps observations to 4 Gbps observations to achieve better sensitivity by enlarging the size of bandwidth for the phase reference source, especially for the continuum observations using B-beam toward the phase reference source. It was because the phase reference source that we used for VERA observations was very faint (~50 mJy beam^{-1}).

The 1 Gbps Observations

The 1 Gbps monitoring observations toward G25.82 were operated with VERA from November 2016 to September 2017. Signals were sampled with 2-bit quantization and filtered to 16 IF bands with 16 MHz bandwidth by the VERA digital filter system. The spectral resolutions for maser and continuum were set to be 15.625 kHz (or 0.21 km s^{-1}) and 1 MHz, respectively.

---

[1] http://www.vlba.nrao.edu/astro/calib/

Table 3.1. Summary of VERA 1 Gbps Observations

Epoch	Observation date	Modified Julian date	Synthesized beam size (PA) (mas×mas) (°)	$T_{\rm sys}$ (K)	$\rm rms_{cont}$ (mJy $\rm beam^{-1}$)	$\rm rms_{maser}$ (mJy $\rm beam^{-1}$)
1	2016 November 24	57716	1.8×0.7 (-34.6)	100-6000	0.33	168.0
2	2017 January 20	57773	1.7 × 0.8 (-32.3)	100-600	0.28	43.5
3	2017 March 17	57829	1.7 × 0.8 (-32.5)	100-2000	0.28	62.7
4	2017 May 02	57875	1.6 × 0.8 (-31.7)	100-2000	0.35	48.4
5	2017 June 02	57906	1.6 × 0.7 (-35.8)	150-2500	0.40	54.8
6	2017 September 15	58011	1.7 × 0.7 (-34.3)	150-3000	0.29	272.4
7	2017 November 12	58069	1.4×1.0(-34.8)	100-4000	0.54	64.8

The accumulation period was 1 second. Data were recorded with hard-disk recorder OCTADISK at the recording rate of 1024 Mbps. One IF channel was assigned to G25.82 while other 15 IF channels were used for the phase reference source, J1846-065151. Correlation process was carried out with the MIZUSAWA software correlator of NAOJ (Oyama et al., 2016). The bandwidth of each IF channel and spectral resolution settings were the same as KaVA observations, 16 MHz and 15.625 kHz (or 0.21 km s^{-1}), respectively. We also used image pixels with maser fluxes greater than 5σ noise level to identify maser spots with the 1σ noise levels. Summary of VERA 1 Gbps observations is listed in Table 3.1.

Calibration processes were also done with AIPS. Because the reference source, J1846-0651, was not bright enough to apply traditional phase referencing technique, we conducted *inverse phase-referencing* analysis to 1 Gbps data which was introduced in Imai et al. (2012) (see the flowchart of inverse phase-referencing from Burns et al. (2015); Figure 3.2). First, we operated the same processes of amplitude calibration as described in Chapter 2. Then, we corrected the Doppler effect such as earth rotation to the LSR velocities of maser source using SETJY and CVEL. Bandpass calibration was done with the calibrator, NRAO 530 or DA406 (J1613+3412).

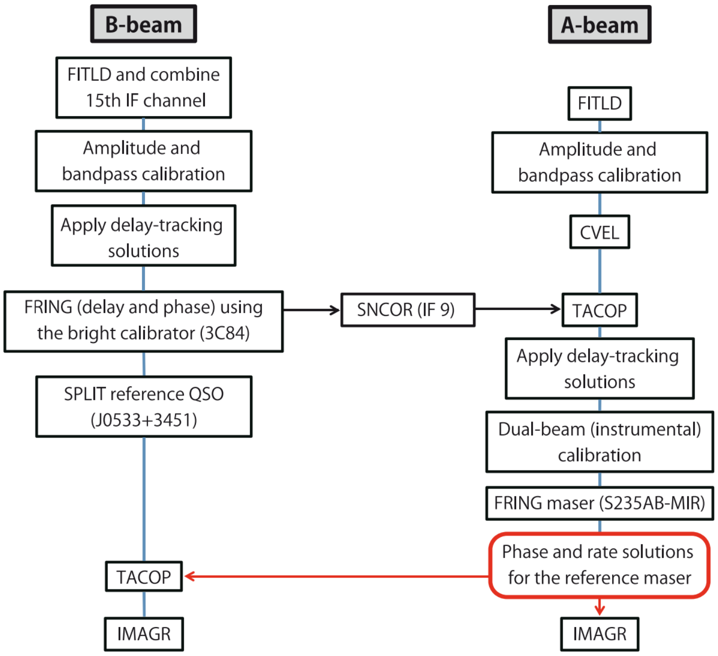

Figure A1. Flowchart of the IPR procedure using VERA7/VERA7MM data.

Figure 3.2: Flowchart of the inverse phase referencing analysis using VERA data from Burns et al. (2015)

For phase calibration, delay-tracking solutions were applied to both A- and B-beam data to correct the geometric delay, troposphere delay, and ionosphere delay (Honma et al., 2008a,b; Nagayama et al., 2020, and see VERA Collaboration et al. (2020) for summary and all references, etc). These solutions were also copied and used to the maser data in A-beam because the B-beam provides better determination of phase slope with the wider bandwidth than that of A-beam.

Instrumental phase differences from the dual-beam system is corrected for A-beam data by applying external table measured using an artificial noise source (Honma et al., 2008a,b; Nagayama et al., 2020). Phase and rate solutions can be obtained with FRING using the reference maser channel in the A-beam. The solutions were applied to the B-beam data (phase-referencing the reference source). Finally, we made an image of the reference source with IMAGR, producing a map having an origin at the phase tracking center of B-beam. The position of the reference source was determined by conducting 2D Gaussian fitting with JMFIT. Since we already knew the accurate position of the reference source, the offset of the new position of the reference source would be the separation of H_2O the reference maser feature from the reference source. Thus, the offset of the reference source gave the absolute coordinates of the maser. Fringe-rate solutions from the A-beam data were also applied to the A-beam for self-calibration. We changed the phase center of G25.82 to $(\alpha,\delta)_{J2000}$= ($18^h39^m03^s.604$, $-06°24'11''.397$) using the result of phase referencing analysis of the first epoch data. After finished all calibration processes, we made images of masers with IMAGR, then estimated the positions by 2D Gaussian fitting with JMFIT. The synthesized beam sizes are listed in Table 3.1.

The 4 Gbps Observations

In this mode, signals were sampled with 2-bit quantization and filtered to 2 IF bands with the bandwidth of 512 MHz. Each IF band was assigned to the target source and reference source, respectively. Sensitivity of 4 Gbps mode is higher than that of 1 Gbps mode by a factor

Table 3.2. Summary of VERA 4 Gbps Observations

Epoch	Observation date	Modified Julian date	Synthesized beam size (PA) (mas×mas) (°)	T_{sys} (K)	rms$_{\mathrm{cont}}$ (mJy beam^{-1})	rms$_{\mathrm{maser}}$ (mJy beam^{-1})
1	2017 December 25	58112	1.7 × 0.9 (−34.1)	110-1700	0.22	27.2
2	2018 February 15	58164	1.4 × 0.8 (−34.4)	100-1400	0.26	28.3
3	2018 April 01	57829	1.6 × 0.8 (−27.2)	100-400	0.13	19.4
4	2018 May 16	58254	2.0 × 0.8 (−8.85)	150-12000	0.26	51.3
5	2018 September 14	58375	1.5 × 0.8 (−29.8)	200-800	0.35	16.5
6	2018 October 29	58420	1.9 × 0.8 (−36.4)	120-2500	0.18	27.5
7	2018 December 20	58462	1.5 × 0.8 (−32.3)	120-350	0.13	22.4
8	2019 February 13	58527	1.8 × 0.8 (−34.5)	100-4000	0.24	25.7
9	2019 April 03	58576	1.5 × 0.9 (−31.6)	100-800	0.15	26.4
10	2019 May 31	58634	2.0× 0.9 (−41.4)	200-2500	0.27	63.1

of $\sqrt{2}$ corresponding to ~ 15 mJy beam^{-1}. Then the phase reference source can be detected with ~ 3σ. The data were recorded with hard-disk recorder VSREC with recording rate of 4096 Mbps. The correlation process is the same as that for 1 Gbps data.

Calibration for the 4 Gbps data was done with AIPS. Traditional phase-referencing analysis was operated (Honma et al., 2008a). Amplitude calibration was applied using the antenna gain and T_{sys} information. Instrumental delay was corrected with calibrator in B-beam. Phase calibration was done with the reference source in B-beam, then we conducted the self-calibration with the reference source. We applied the UVW recalculation table and the dual beam instrumental phase calibration to A-beam with external tables. For the next step, we copied and applied the phase calibration and self-calibration solutions from B-beam to A-beam data. After that, we made the images of the target source with IMAGR, then estimated the positions by 2D Gaussian fitting with JMFIT. Summary of VERA 4 Gbps observations is listed in Table 3.2.

Table 3.3. Summary of KaVA Observations

Epoch	Observation date	Modified Julian date	Synthesized beam size (PA) (mas×mas) (°)	rms (mJy beam^{-1})
1	2018 March 12	58189	1.19 × 1.16 (−37)	23.9
2	2018 April 30	58238	1.44 × 1.12 (−15)	50.9
3	2018 September 04	58365	1.53 × 1.01 (−8)	36.4
4	2018 October 26	58417	1.42 × 1.08 (−14)	23.2
5	2018 November 11	58433	1.49 × 1.11 (−18)	35.7
6	2019 January 16	58499	1.61 × 1.17 (0)	17.7
7	2019 February 26	58540	1.43 × 1.07 (−19)	20.7
8	2019 April 13	58586	1.47 × 1.14 (−16)	24.2

3.3.2 KaVA Observations

G25.82 was also monitored with KaVA to collect more maser features at K-band from March 12, 2018 to April 13, 2019, as a part of a monitoring survey toward high-mass star-forming regions (see Chapter 2.3). The position of the phase tracking center of the target was (α,δ) = ($18^h39^m03^s.63$, -6°24′09″.5) in the J2000.0 epoch. Observation settings, correlation processes, and calibration processes were the same as described in Chapter 2.2. An extragalactic radio continuum source, NRAO 530 was employed for calibration for G25.82. The second epoch of monitoring observations (r18120b) has been excluded for further analysis because of technical error in observations.

Imaging were performed using the AIPS. We set the cell size of image as 0.2 mas and the pixel number of each axis as 4096 to cover all detected H_2O masers toward targets. The peak positions of maser spots were derived by 2D Gaussian fitting to the individual channel images using the SAD. We employed image pixels greater than 5σ noise level for the Gaussian fitting to distinguish maser spots from side lobes. To adjust the reference positions of each distribution maps at each epochs, the position of 93.7 km s^{-1} feature was used as the central position of the maps.

3.4 Results

3.4.1 Annual Parallax Measurement

Several H_2O maser features have been identified which are relatively stable during 900 days toward G25.82. The absolute proper motions and annual parallax of these maser features were derived to provide accurate constraints such as distance. The features were chosen for measurement that were detected in more than five epochs. The 8 maser features have been successfully employed based on these criteria as listed in Figure 3.4.1. We fit the measured absolute positions of the maser features with least-square method. A χ^2 fit of the common annual parallax (π) and linear absolute proper motions (μ) of each feature were operated.

Figure 3.4.1 shows the best-fit parallax with all data points after the subtraction of linear proper motions. We adapted the errors produced by JMFIT as the formal error which are thought to be thermally generated. Since errors in the measurements are larger than expected from thermal errors of 0.1 mas, in the fitting process, systematic errors (post-fit residuals) were obtained by iterating until the reduced χ squared to be unity. These additional error floors of 0.08 mas and 0.13 mas were added in the RA direction and Dec direction, respectively. The estimated parameters are the parallax, π, initial position, $(\Delta\alpha, \Delta\delta)$, and linear proper motion $(\mu_\alpha \cos\delta, \mu_\delta)$. The results are shown in Figure 3.3. Obtained parallax is 0.225 ± 0.020 mas, corresponding to a distance of $4.44^{+0.4}_{-0.4}$ kpc.

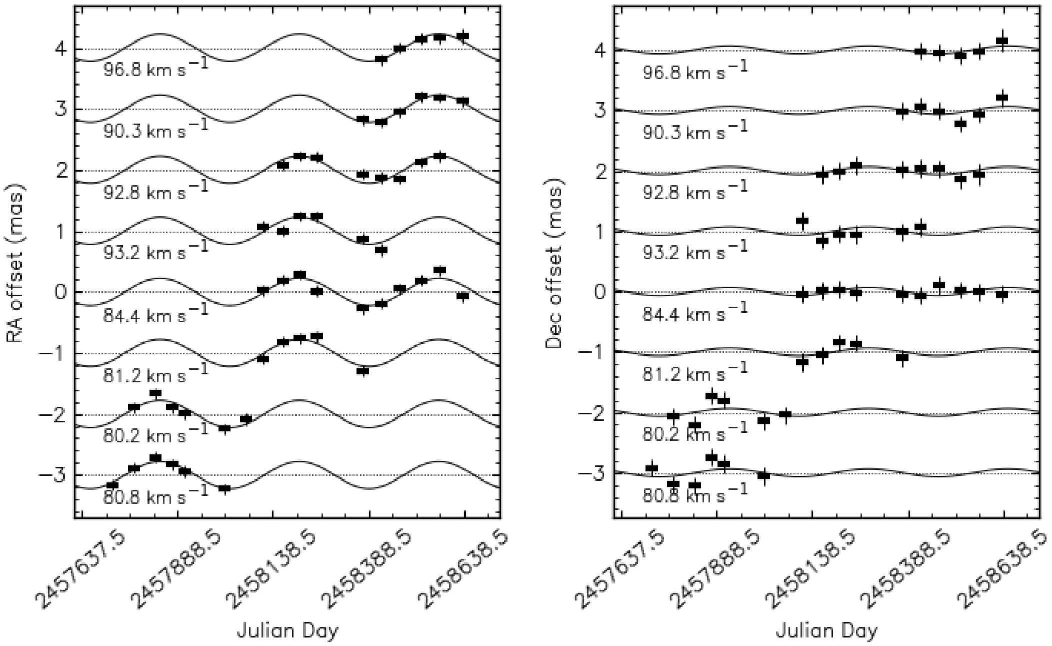

Figure 3.3: Parallax and proper motion fits of G25.82, yielding an absolute parallax of 0.225 ± 0.020 mas

Table 3.4. Absolute positions of the maser features toward G25.82

Feature ID	Epoch	V_lsr (km s^{-1})	$\Delta\alpha\cos\delta$ (mas)	$\Delta\delta$ (mas)
1	161124	80.8	4.74 (0.009)	3.57 (0.012)
1	170120	80.2	4.47 (0.006)	2.89 (0.008)
1	170317	80.4	4.10 (0.008)	2.47 (0.010)
1	170502	80.4	3.54 (0.013)	2.61 (0.018)
1	170602	80.2	3.13 (0.017)	2.28 (0.020)
1	170915	79.9	1.83 (0.011)	1.32 (0.014)
2	170120	80.2	3.31 (0.006)	0.01 (0.008)
2	170317	80.4	2.99 (0.009)	−0.50 (0.011)
2	170502	80.4	2.31 (0.011)	−0.30 (0.015)
2	170602	80.2	1.90 (0.012)	−0.58 (0.014)
2	170915	79.9	0.62 (0.011)	−1.60 (0.015)
2	171112	80.4	0.22 (0.016)	−1.87 (0.017)
3	171225	81.2	0.02 (0.010)	−2.83 (0.013)
3	180215	81.4	−0.13 (0.008)	−3.51 (0.009)
3	180401	81.6	−0.44 (0.004)	−4.00 (0.006)
3	180516	82.1	−0.78 (0.008)	−4.70 (0.017)
3	180914	82.3	−2.34 (0.009)	−6.80 (0.010)
4	171225	84.4	−0.45 (0.011)	−2.98 (0.013)
4	180215	84.4	−0.69 (0.008)	−3.61 (0.010)
4	180401	84.4	−0.94 (0.004)	−4.18 (0.006)

Table 3.4 (cont'd)

Feature ID	Epoch	V_lsr (km s^{-1})	$\Delta\alpha\cos\delta$ (mas)	$\Delta\delta$ (mas)
4	180516	84.6	−1.56 (0.006)	−4.83 (0.014)
4	180914	84.4	−2.78 (0.008)	−6.45 (0.009)
4	181029	84.2	−3.04 (0.006)	−7.07 (0.008)
4	181220	83.9	−3.21 (0.011)	−7.58 (0.014)
4	190213	84.0	−3.49 (0.005)	−8.39 (0.007)
4	190403	83.9	−3.71 (0.003)	−9.07 (0.004)
4	190531	84.2	−4.58 (0.009)	−9.87 (0.013)
5	171225	93.2	114.58 (0.013)	23.70 (0.016)
5	180215	94.1	114.26 (0.009)	22.68 (0.011)
5	180401	94.1	114.30 (0.004)	22.19 (0.006)
5	180516	94.3	114.09 (0.006)	21.58 (0.014)
5	180914	93.8	113.16 (0.006)	20.02 (0.007)
5	181029	93.6	112.78 (0.016)	19.50 (0.019)
6	180215	92.8	114.41 (0.011)	22.87 (0.013)
6	180401	92.8	114.29 (0.006)	22.41 (0.008)
6	180516	92.6	114.01 (0.008)	21.99 (0.018)
6	180914	92.4	113.01 (0.007)	20.52 (0.008)
6	181029	92.4	112.69 (0.018)	20.03 (0.022)
6	181220	92.2	112.36 (0.005)	19.42 (0.007)
6	190213	92.2	112.31 (0.007)	18.61 (0.009)

Table 3.4 (cont'd)

Feature ID	Epoch	V_lsr (km s^{-1})	$\Delta\alpha\cos\delta$ (mas)	$\Delta\delta$ (mas)
6	190403	92.3	112.12 (0.031)	18.13 (0.043)
7	180914	90.3	−4.60 (0.005)	−5.52 (0.006)
7	181029	90.3	−4.99 (0.005)	−5.91 (0.006)
7	181220	90.3	−5.22 (0.006)	−6.53 (0.008)
7	190213	90.5	−5.40 (0.005)	−7.31 (0.007)
7	190403	90.6	−5.79 (0.002)	−7.67 (0.003)
7	190531	90.7	−6.30 (0.009)	−7.99 (0.011)
8	181029	96.8	154.26 (0.007)	252.45 (0.008)
8	181220	96.8	154.10 (0.007)	251.81 (0.010)
8	190213	96.8	153.88 (0.009)	251.11 (0.012)
8	190403	96.9	153.56 (0.007)	250.60 (0.010)
8	190531	96.6	153.20 (0.042)	250.10 (0.063)

3.4.2 Internal proper motion of H_2O maser

Internal proper motions of H_2O maser features in G25.82 were measured using KaVA monitoring data (Figure 3.4). Using the position of the 97.3 km s^{-1} feature as reference, we obtained the relative distribution of all detected H_2O maser features (Figure 3.5). Although lifetime of H_2O masers is short, several components are relatively stable to be detected during multiple epochs. In total, 21 H_2O maser features were identified which were detected at least in three epochs. Most of identified H_2O maser features have blueshifted or similar velocities to the systemic velocity of G25.82 (93.7 km s^{-1}). The proper motions of each fea-

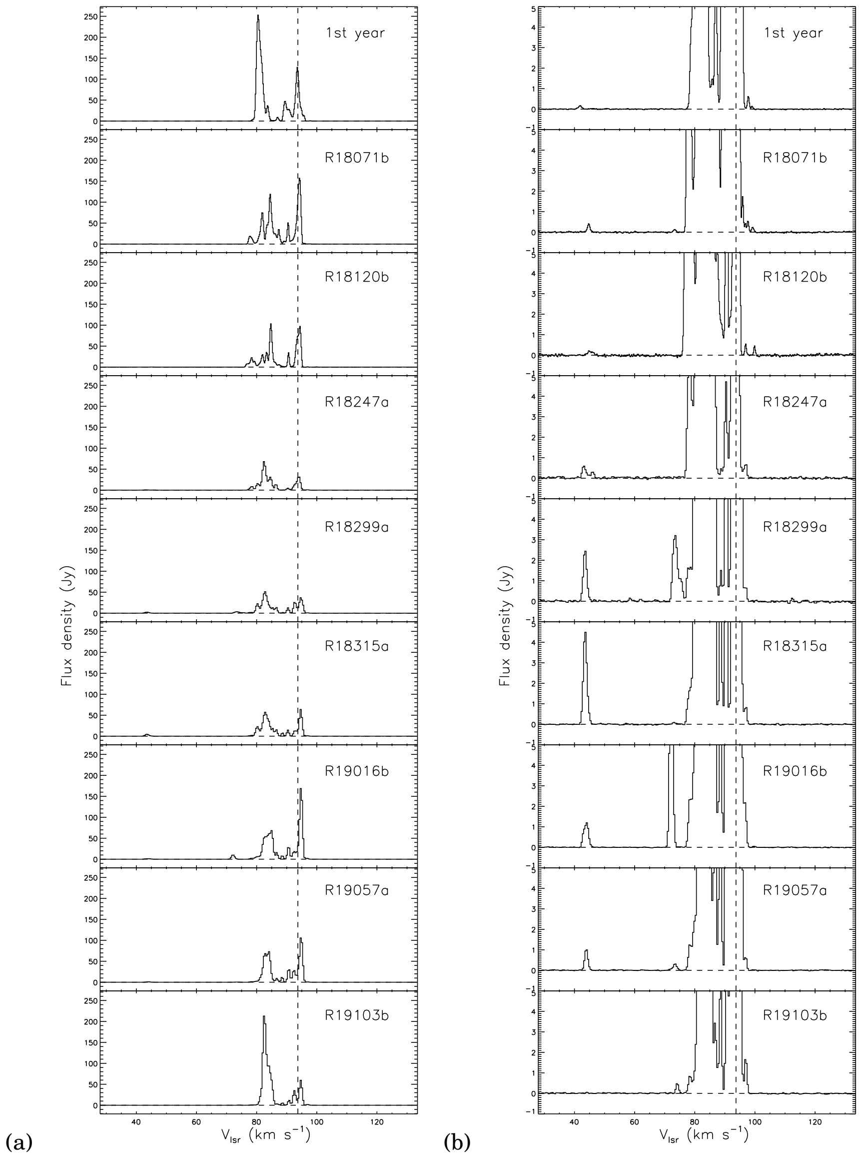

Figure 3.4: (a) Water maser spectra toward G25.82-0.17. (b) Zoomed up spectra for the weaker features with the modified y range is shown. Vertical dashed lines denote the systemic velocity of G25.82-0.17. Vertical dashed line shows the velocity component the used for the reference position in Figure 3.5.

ture are derived by linear fitting the positions in directions of right ascension and declination each. For example, linear fitted results for 86.5 km s^{-1} and 97.1 km s^{-1} features are shown in Figure 3.6.

The relative proper motion vector of i^{th} component ($\vec{\mu_i^r}$) contains the internal motions of masers and the systemic motions of the reference feature expressed as

$$\vec{\mu_i^r} = \vec{\mu}_i + \vec{\mu}_0. \tag{3.1}$$

Here $\vec{\mu}_i$ indicates the internal motion of i^{th} component while the $\vec{\mu}_0$ is that of reference feature (93.7 km s^{-1}). To extract pure internal motion, $\vec{\mu}_i$, $\vec{\mu}_0$ was subtracted assuming symmetric motions. The summation of all $\vec{\mu}_i$ should be zero. Therefore, $\vec{\mu}_0$ can be derived as

$$\vec{\mu}_0 = -\frac{1}{n}\sum_{i\neq 0}^{n} \vec{\mu_i^r}. \tag{3.2}$$

Reconstructed $\vec{\mu}_i$s are listed in Figure 3.4.2.

These relative proper motions were converted to absolute proper motions using that of 97.1 km s^{-1} feature obtained with VERA monitoring data. In addition, the relative positions of all maser features from KaVA were modified to absolute positions using the absolute position of the reference feature (80.5 km s^{-1} feature). In Figure 3.7, both features identified by KaVA (dots) and VERA (stars) with their internal motion vectors are presented. In addition to the bluest feature, slightly redshifted velocity component (97.1 km s^{-1} feature) moving toward the NE. Features having velocities close to the systemic velocity distributed at Dec offset~ 0 are moving away each other. The central cluster shows motions divided into two groups which are moving toward N and SW. Further discussions on the internal proper motions and circumstellar gas distribution will be done in the next chapter.

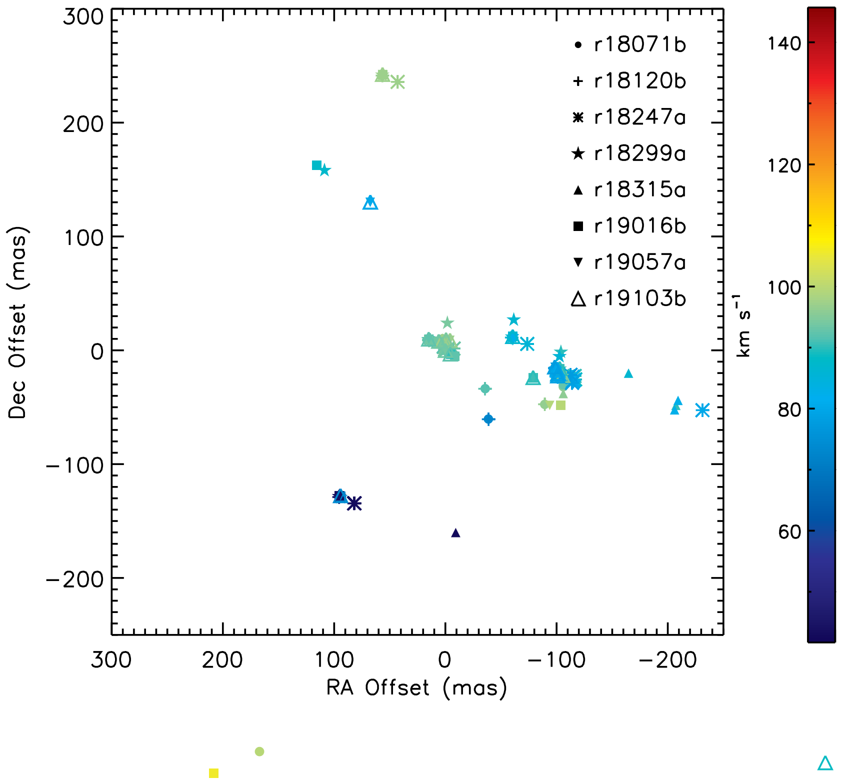

Figure 3.5: Distribution of H_2O masers toward G25.82. Filled circles denote H_2O maser spots having the same velocities in the color bar. The reference position (0,0) is the position of the reference maser feature having a velocity of 93.7 km s^{-1} which is the same as the systemic velocity of G25.82.

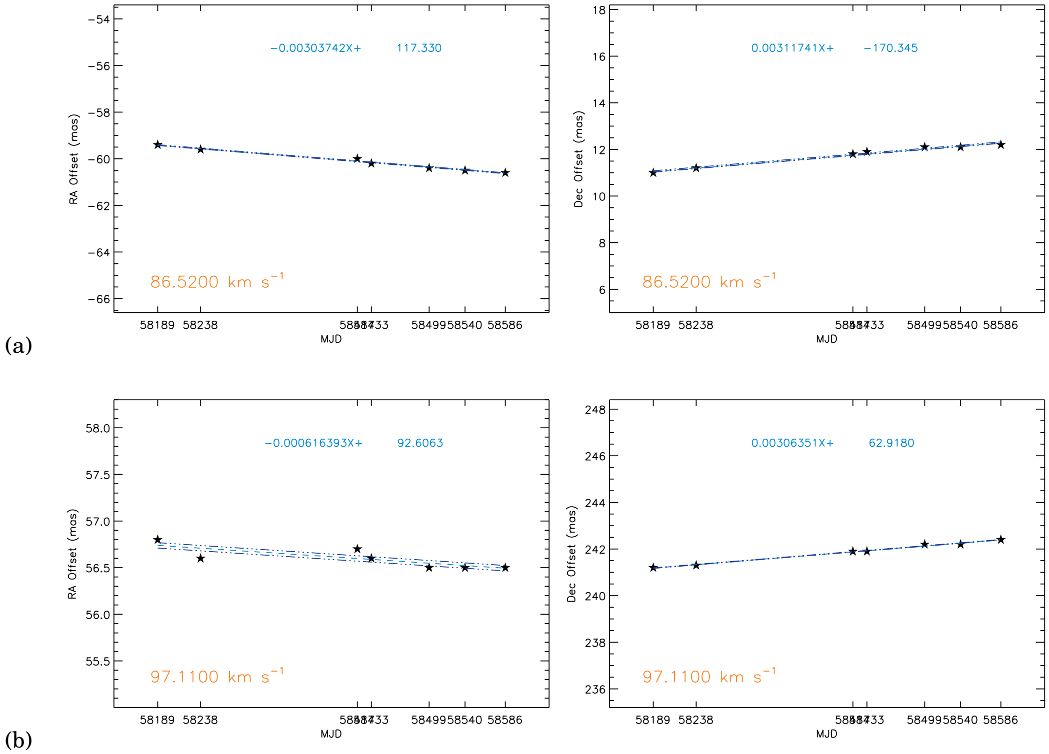

Figure 3.6: Linear fitting results of (a) 86.52 km s^{-1} feature and (b) 97.11 km s^{-1} feature. Stars denote maser positions. Blue dashed lines and navy dash-dot-dot-dot lines indicate linear fitting result and deviation, respectively.

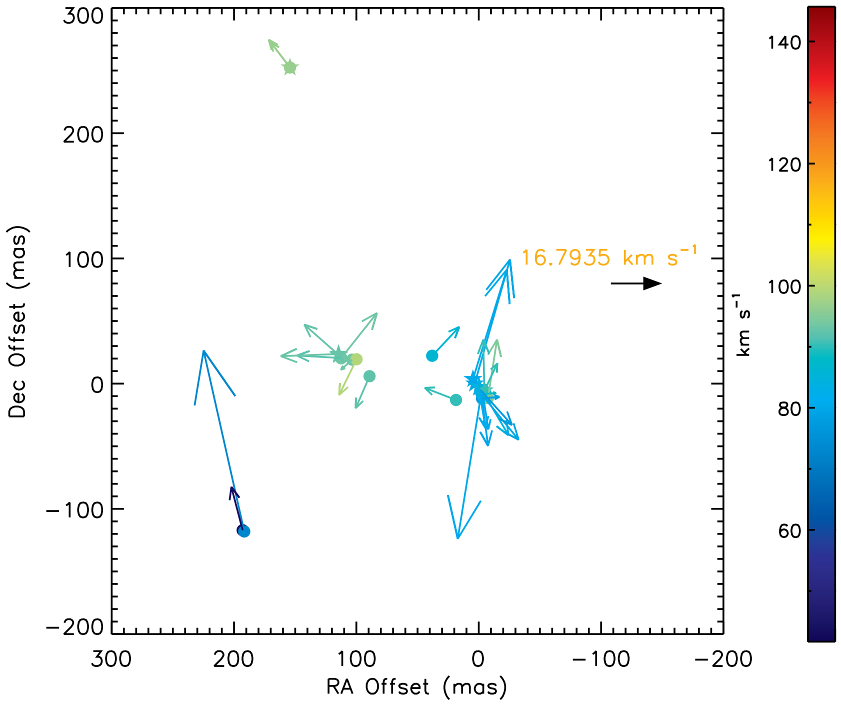

Figure 3.7: Proper motion of H_2O maser in G25.82. Filled circles denote H_2O maser spots having the same velocities in the color bar.

Table 3.5. Parameters of the 22 GHz water maser features in G25.82

Epoch ID	Detection	V$_{\rm lsr}$ (km s^{-1})	$\Delta\alpha\cos\delta$ (mas)	$\Delta\delta$ (mas)
1	1245 _ _ _	99.4	2.4	8.2
2	1245678	97.1	56.6	241.2
3	_ _ 45678	94.9	−105.0	−22.8
4	_ _ 456_ _	93.8	6.0	7.9
5	_ _ 456_ _	93.8	15.1	9.0
6	_ _ _ 567 _	92.5	−8.2	−5.3
7	_ 245 _ _ _	92.1	14.9	9.2
8	1245678	90.4	−102.0	−17.1
9	_ _ _ _ 5678	90.4	−78.9	−24.3
10	_ 24567 _	88.5	−102.0	−17.2
11	1245678	86.5	−59.4	11.0
12	_ _ _ 567 _	84.8	−100.8	−17.6
13	12456_ _	82.6	−101.1	−20.8
14	124_ _ _ _	80.7	−99.8	−17.6
15	_ _ _ _ 678	80.5	−101.0	−20.5
16	1245 _ _ _	79.8	−99.6	−18.6
17	_ _ 456 _ _	79.8	−100.7	−20.9
18	_ 24567 _	78.1	−100.1	−23.1
19	_ 245 _ _ _	77.6	−98.8	−16.3
20	_ _ 45678	73.3	94.2	−129.3
21	_ _ 4567 _	44.0	95.5	−128.3

3.5 Discussions

We derived the distance to G25.82 to be $4.44^{+0.43}_{-0.36}$ kpc from the sun. Estimated parallactic distance is ~70% of the kinematic distance of 6.7 kpc from Walsh et al. (1997) derived assuming a distance to the Galactic center, $R_\odot$, of 10 kpc and a Galactic circular rotation of the Sun, $\Theta_\odot$, of 250 km s^{-1}. On the other hand, our value shows better agreement with the kinematic distance of 5 kpc from Green & McClure-Griffiths (2011), assuming a flat rotation curve with the $R_\odot$ of 8.4 kpc (Bovy et al., 2009) and the $\Theta_\odot$ of 246 km s^{-1} (Ghez et al., 2008; Gillessen et al., 2009; Reid et al., 2009). In addition, it also show the same result compare to the kinematic distance of 5 kpc estimated with the galactic parameters of $R_\odot$ =7.92 kpc and $\Theta_\odot$ =227 km s^{-1}) from the recent VERA astrometry catalog (VERA Collaboration et al., 2020). Our parallactic distance is a factor of 0.89 (=4.44 kpc/5.0 kpc) smaller than the kinematic distance. In addition, uncertainty is deduced to 10% of 90%. Therefore, the physical parameters, mass of the G25.82, for example, have been slightly overestimated in the past. In case of mass is proportional to the square of the distance, it have been overestimated by a factor of 1.3. There is going to be the same impact on luminosity as that for the mass because radio luminosity is also proportional to the square of the distance. The mass of the core of G25.82 estimated from the $C^{18}O$ line data by de Villiers et al. (2014) can be revised to 106 $M_\odot$. This parallactic distance is going to be used for further analysis toward G25.82 with thermal line and continuum emission which is shown in the next chapter.

The position of Sun and the our parallactic distance, the location of G25.82 in the Galaxy can be provided. As shown in Figure 3.8, G25.82 is located on the "Scutum-Centaurus Arm" at the edge of "Long Bar" at the galactic center. G25.82 is located at the edge of arm, however, location is in the middle of other neighboring high-mass star-forming regions (Reid et al., 2014). Therefore, G25.82 is also located at the inner Galaxy region where the star formation is actively occurring. Combining the distance from the parallax measurement and the proper motions of the masers can provide not only the location of the maser source in the Galaxy, but

Table 3.6. Parallaxes of High-mass Star-forming Regions

Source	l (deg)	b (deg)	Parallax (mas)	Distance (kpc)	Ref.[a]
G13.87+0.28	13.87	+0.28	-0.25 ± 0.024	$3.94^{+0.41}_{-0.34}$	2
G16.58-0.05	16.58	-0.05	0.28 ± 0.023	$3.58^{+0.32}_{-0.27}$	2
G23.01-0.41	23.01	4.59	0.22 ± 0.02	$4.59^{+0.38}_{-0.33}$	3
G25.82-0.17	25.83	-0.18	0.23 ± 0.02	$4.44^{-0.36}_{+0.43}$	1
G29.95-0.01	29.96	-0.02	0.19 ± 0.019	$5.26^{+0.58}_{-0.48}$	2
G31.28+0.06	31.28	+ 0.06	0.23 ± 0.039	$4.27^{+0.85}_{-0.61}$	4
G31.58+0.07	31.58	+ 0.08	0.20 ± 0.030	$4.90^{+0.85}_{-0.63}$	4
G32.04+0.05	32.04	+ 0.06	0.19 ± 0.008	$5.18^{+0.22}_{-0.21}$	2

[a] References. (1) this work, (2) Sato et al. (2014), (3) Brunthaler et al. (2009), (4) Zhang et al. (2014).

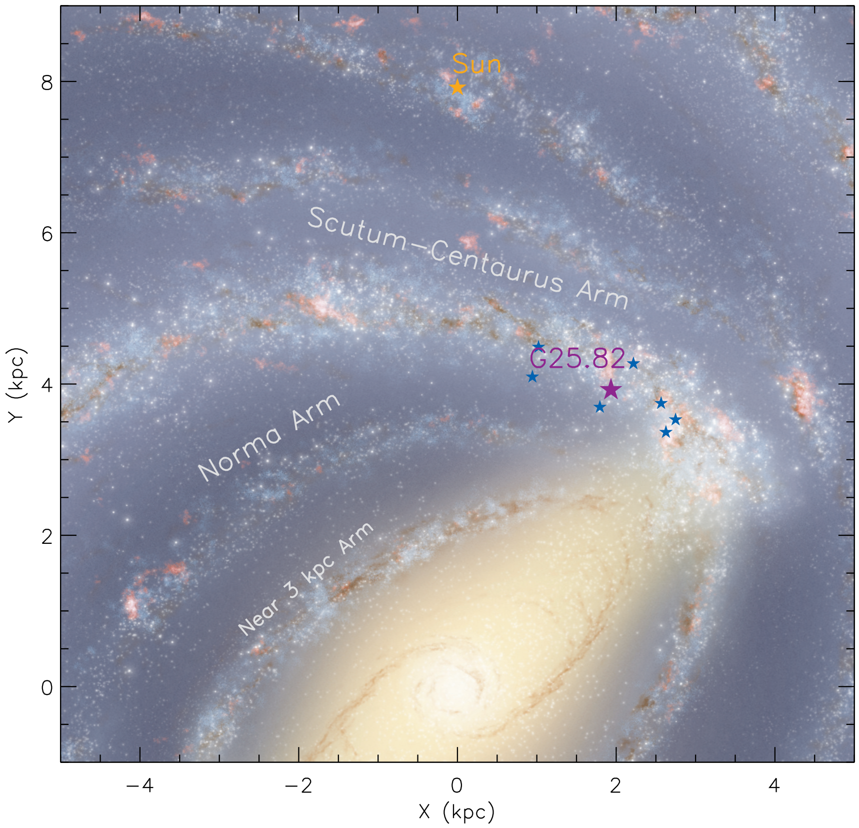

Figure 3.8: Location of G25.82 projected on the Galactic plane is denoted by a purple star. Blue stars show the galactic position of other star-forming regions listed in Table 3.6. The background is an artist's sketch of the Milky Way (R. Hurt:NASA/JPL-Caltech/SSC) looked down from the north Galactic pole from which the Galaxy rotates clockwise. The Galactic Center is at (0, 0) and the Sun (orange star) at (0, 7.92) kpc.

Table 3.7. Peculiar Motion of G25.82

U_s (km s^{-1})	V_s (km s^{-1})	W_s (km s^{-1})
33 ± 5	-9 ± 5	18 ± 5

also the full space motion of the region. We can subtract the effect of Galactic rotation and the peculiar motion of the Sun from the motion of the maser source. Then the peculiar motions of the maser source can be estimated. Following the methods and detailed discussion by (Reid et al., 2009), the individual peculiar motion of maser source can be representative of that of the whole high-mass star-forming region. The three of motion components are defined as locally moving toward the Galactic center, U_s, toward direction of Galactic rotation, V_s, and toward the north Galactic pole, W_s.

We adopt the values of $R_\odot$ =7.92 kpc and $\Theta_\odot$ =227 km s^{-1} from (VERA Collaboration et al., 2020). In addition, we assumed for the solar motion to be ($U_\odot$, $V_\odot$, $W_\odot$) = (11.1, 12.24, 7.25) in km s^{-1} (Schönrich et al., 2010). It may be strongly affected by the parallax uncertainty, we obtained the peculiar motion components of G25.82 listed in Figure 3.5.

Since we measured the exact distance to G25.82, the first discussions on the dynamics of G25.82, which will be introduced in the next chapter, was possible.

Chapter 4

Multiple outflows in the high-mass cluster forming region, G25.82–0.17

4.1 Introduction

Although masers are good probes to trace velocity field with high resolution, they can only provide spatially sparse structures. Therefore, outflow structures traced by thermal lines are essential to fill the gap between central HM-YSOs and maser distributions emitted in the outflows. Moreover, the powering sources cannot be identified due to the low continuum sensitivity of VLBI, and hence, follow-up observations of continuum emission with ALMA are necessary to understand basic properties of the systems, such as positions of the HM-YSOs and masses of hosting cores. Through the complementary follow-up observations with ALMA, physical properties can also be derived quantitatively. Studying a large sample of HM-YSOs via their maser emission will help to reveal the roles of disks and outflows in the formation of high-mass stars.

The H_2O masers having large velocity diversity ($\Delta V \sim 55$ km s^{-1}) were detected with KaVA with compact spatial distribution ($\sim 0''.2$). Velocity range of detected H_2O maser components is from 41.5 km s^{-1} to 98.0 km s^{-1}. The 3D velocity field of H_2O masers in the vicinity of the powering source was already obtained from the intense monitoring observations with VERA and KaVA. Thus, G25.82 is a suitable target for a detailed study of the HM-YSO(s) associated with outflow and possibly disk through high resolution maser observations.

4.2 Observations and Data Analysis

4.2.1 ALMA Observations

ALMA observations of G25.82 in Band 6 (230 GHz) were performed as a part of the KaVA LP project on August 19, and 22, 2016 (project 2015.1.01288.S: P.I. M.-K. Kim). The number of 12 m antennas was 36 and baseline lengths ranged from 15 to 1462 m. The phase tracking center for observations was $(\alpha,\delta)=(18^h39^m03^s.63, -06°24'09''.5)$ in the J2000.0 epoch. We set five spectral windows (spws) to cover the SiO 5–4 line, CH_3OH lines, and continuum emission. The 36 GHz series of the CH_3OH 8_{-1}–7_0 E maser line (class I; Slysh et al., 2002), is included. Frequencies of the observed lines are listed in Table 1. The spectral resolution and bandwidth were 1953.04 kHz (~1.3 km s^{-1}) and 937.5 MHz (~1300 km s^{-1}), respectively. In addition to the maser transitions, thermal CH_3OH lines such as CH_3OH 22_4–21_5 E were also included. The on-source time was 33 minutes. Initial data calibration was carried out using the ALMA pipeline from the CASA[1] package version 4.7 (McMullin et al., 2007). The half-power beamwidth (HPBW) of the primary beam was approximately 27″ at the observing frequencies and the synthesized beam size of the continuum data was 0".27 × 0".24 with a position angle of −83.6. Synthesized beams for the line images range from 0".25 × 0".26 to 0".30 × 0".26 using a robust weighting of 0.5. Plotting and analysis were done with the *Miriad*[2] software package (Sault et al., 1995).

---

[1] https://casa.nrao.edu/

[2] http://www.atnf.csiro.au/computing/software/miriad/

4.2.2 KaVA Observations

We used the KaVA imaging survey data observed on November 17, 2016, toward G25.82 at K-band (22 GHz). Observation settings, correlation processes, and calibration processes were the same as described in Chapter 2.2 and Chapter 3.2.2.

Imaging were performed using the IMAGR. The peak positions of maser spots were derived by Gaussian fitting to the individual channel images using the SAD. We employed image pixels greater than 5σ noise level for the Gaussian fitting to distinguish maser spots from side lobes with 1σ noise level of 23 mJy beam^{-1}.

4.2.3 VERA Observations

The first epoch of VERA observations in the 1 Gbps mode at K-band toward G25.82 was used (see also Chapter 3.2.1). Calibration processes were also done with AIPS. Traditional phase-referencing method was applied to derive the absolute positions of H_2O masers. Dual-beam phase calibration and delay correction were applied to the visibility data (Honma et al., 2008a). Instrumental delays and phase offsets were removed by executing FRING on DA406 (J1613+3412). Bandpass calibration was also conducted using DA406. Finally, residual phases were calibrated by running FRING on J1846-0651 and the solutions were applied to G25.82. Imaging and identifying maser spots was done through the same processes for KaVA data introduced in Chapter 2.2. The H_2O maser spot at a velocity of 80.5 km s^{-1} was used as a reference of absolute position for calculating the relative positions of other maser spots detected in KaVA observation.

Table 4.1. Summary of observed emissions

	Transition	ν (GHz)	E_L (K)	rms (mJy beam^{-1})	Reference	Telescope
H_2O	$6_{1,6}$-$5_{2,3}$	22.235080	642.43	30	JPL[a]	KaVA, VERA
SiO	5–4	217.104980	20.84	1.45	JPL	ALMA
CH_3OH	8_{-1}–7_0 E	229.758811	78.08	1.43	JPL	ALMA
CH_3OH	22_4–21_5 E	230.368199	671.69	1.24	JPL	ALMA
CO	2–1	230.538000	5.53	4.25	CDMS[b]	ALMA
Continuum				0.40	···	ALMA

[a] Jet Propulsion Laboratory Catalog (JPL; Pickett et al., 1998).

[b] Cologne Database for Molecular Spectroscopy (CDMS; Müller et al., 2001)

4.3 RESULTS

4.3.1 Continuum Emission

Figure 4.1 shows the distribution of 1.3 mm continuum emission obtained with ALMA in G25.82. The structure comprises two parts (G25.82–E and G25.82–W) with a separation in the E-W direction of 3″. The weaker component, G25.82–E, is located 0″.6 south from the peak of WISE 22 μm emission. The positional accuracy of the WISE source is indicated by the extent of the diamond in Figure 4.1 (($\Delta\alpha$, $\Delta\delta$)=(0″.12, 0″.13)).

Continuum emission at 1.3 mm toward G25.82–W shows a cometary structure and evidence of multiplicity. Three components were identified by two-dimensional Gaussian fits to emission at intensities larger than 10σ of the noise level (1σ = 0.4 mJy beam^{-1}). These three components were named as G25.82–W1, G25.82–W2, and G25.82–W3 (plus marks in Figure 4.1). The key parameters of these 1.3 mm continuum sources are listed in Table 4.2.

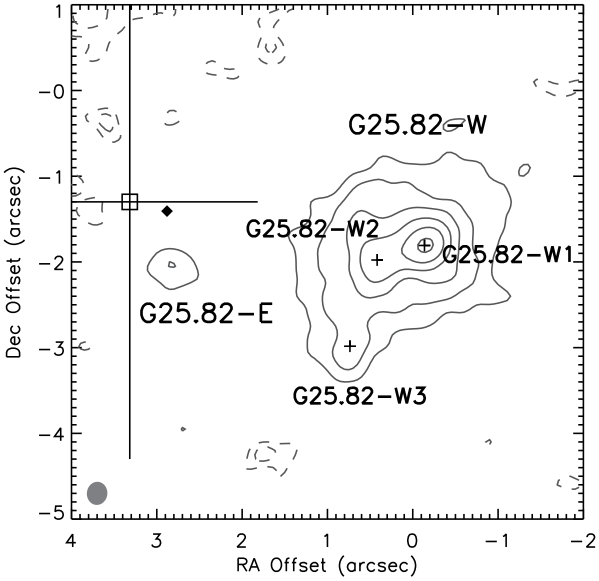

Figure 4.1: Continuum emission map toward G25.82 at 1.3 mm obtained with ALMA. Contour levels are 10σ, 20σ, 40σ, 80σ, 160σ, and 320σ, where 1σ is 0.4 mJy beam^{-1} while dashed contours are negative levels of -1σ and -2σ. The filled gray circle in the bottom left corner indicates the synthesized beam size of the 1.3 mm continuum image. The absolute coordinate of the (0,0) position is ($18^h39^m03^s.63$, -6°24$'$09$''$.5) in the J2000.0 epoch. Small crosses denote the positions of 1.3 mm continuum sources in G25.82–W. An open square indicates the peak position of VLA radio continuum emission with the angular resolution denoted by the cross (Hu et al., 2016). In addition, the position of WISE source is marked with the filled diamond. The absolute position error of ALMA Cycle 3 observations is less than 0$''$.01 while the VLA error is 0$''$.3 (Hu et al., 2016).

Table 4.2. Parameters of the 1.3 mm Continuum

	RA [$^{h\ m\ s}$]	Dec [$^{\circ\prime\prime\prime}$]	Peak Flux [mJy beam^{-1}]	Integrated Flux Density [mJy]	Source Size [$''\times''$], P.A. °
G25.82–W1	18:39:03.62	-6:24:11.31	143 (0.2)	377 (0.8)	[0.5 × 0.4], 116.4
G25.82–W2	18:39:03.66	-6:24:11.48	53 (0.2)	237 (1.3)	[0.6 × 0.5], 178.6
G25.82–W3	18:39:03.68	-6:24:12.48	13 (0.2)	65 (1.4)	[0.7 × 0.5], 160.5
G25.82–E	18:39:03.82	-6:24:11.56	8 (0.2)	31 (1.2)	[0.7 × 0.5], 80.2

4.3.2 Molecular Line Emission

A number of molecular lines are detected toward G25.82 at (sub) millimeter wavelengths. Most of the detected lines are distributed in the vicinity of G25.82–W which is in the earlier stage than having HII region and show a compact morphology. It implies that G25.82–W is one of hot molecular cores (e.g. Kurtz et al., 2000; Beuther, 2007). In this study, we focus on four molecular lines as representative tracers of high-density gas; the CO 2–1, SiO 5–4, CH_3OH 8_{-1}–7_0 E, and CH_3OH 22_4–21_5 E lines from the ALMA observations and the H_2O $6_{1,6}$-$5_{2,3}$ maser from the KaVA observations.

The profiles of molecular lines obtained with ALMA are shown in Figure 4.2. Using a Gaussian profile, fitting was done to derive line parameters such as the peak flux density, central velocity, and FWHM of the Gaussian. The central velocities of the CO 2–1, SiO 5–4, CH_3OH 8_{-1}–7_0 E, and CH_3OH 22_4–21_5 E lines are 94.3 km s^{-1}, 94.3 km s^{-1}, and 92.9 km s^{-1}, respectively. These are consistent with the adopted systemic velocity of G25.82 (93.7 km s^{-1}). The FWHM of the CH_3OH 8_{-1}–7_0 E and CH_3OH 22_4–21_5 E lines are 6.8 km s^{-1} and 6.3 km s^{-1}, respectively. The CO 2–1 and SiO 5–4 line have a broader FWHM ($\Delta v \sim 11.7$ km s^{-1}) than the other two lines.

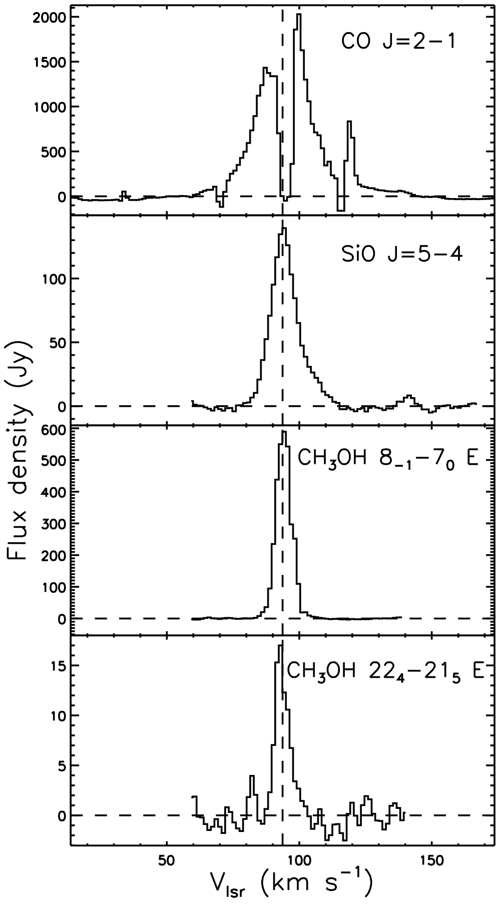

Figure 4.2: Spectra of analyzed molecular transitions toward G25.82 observed with ALMA. The vertical and horizontal dashed lines represent the systemic velocity (93.7 km s^{-1}; Wienen et al., 2012) of G25.82 and the zero baselines, respectively. Spectra are integrated over the rectangular region (15″ × 15″) as indicated in Figure 4.4 while the spectrum of CO 2–1 is integrated over the region (20″ × 25″).

CO 2–1

In Figure 4.3, outflowing gas traced by the CO 2–1 line toward G25.82 is shown. The outflow wing has been defined as the velocity components broader than the velocity width of the CH_3OH 22_4–21_5 E line (FWHM=6.3 km s^{-1}). The velocity ranges of the blue- and red-shifted components are defined as from 5.8 km s^{-1} to 80.1 km s^{-1} and from 103.7 km s^{-1} to 172.2 km s^{-1}, respectively. Comparable velocity ranges to each other are shown for both blue- and red-shifted wings.

Although the distribution of the CO 2–1 line is complicated, at least clear two CO outflows are identified in G25.82. One is N1–S1 CO outflow having blue- and red-shifted components at north and south. The other is is SE–NW CO outflow with the preceding gas in southeast and the receding gas in northwest of G25.82–W. The N1–S1 CO outflow originates from a position ~$0''.2$ northwest of G25.82–W1 and has an extent of about $12''$. Its total velocity range is from 5.8 km s^{-1} to 172.2 km s^{-1}. We should note that within this velocity range, contamination from other molecular lines is contained, especially in the vicinity of G25.82–W1. Main structures of blueshifted and redshifted emission exhibit similar distribution, extending to the north and south, respectively. The CO emission of this SE-NW outflow is very weak compared to N1-S1 CO outflow but still significant ($> 5\sigma$). The blueshifted (SE) and redshifted (NW) components can be seen in the integrated intensity map with the velocity ranges of 5.8−80.1 km s^{-1} and 103.7−172.2 km s^{-1}, respectively. The SE–NW CO outflow originates from a position separated at least ~$0.8''$ to the south from the three continuum sources and extends about $17''$.

SiO 5–4

One of the well-known outflow tracers (e.g., López-Sepulcre et al., 2011; Codella et al., 2013; Leurini et al., 2014), SiO, delineates the spatial and velocity structures of outflowing gas in G25.82. The outflow components have wing-like spectral features broader than the velocity

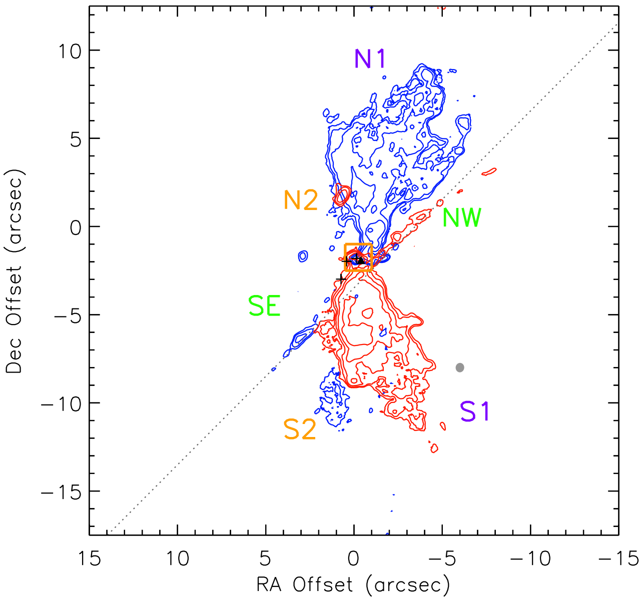

the intervals of 5σ, where 1σ for blue and red components are 9.8 mJy $\mathrm{beam}^{-1}\cdot$ km s^{-1} and 18 mJy $\mathrm{beam}^{-1}\cdot$ km s^{-1}, respectively. Positions of G25.82–W1, W2, and W3 are marked with black crosses while that of the H_2O maser spot at 80.5 km s^{-1} is denoted by a black triangle. The dotted line indicates the outflow axis of SE–NW CO outflow. The orange box indicates the area shown in Figure 4.8. The absolute positional uncertainties of water maser features are in all cases < 1 mas. In addition, that of ALMA Cycle 3 observations is less than $0''.01$.

Figure 4.3: Integrated intensities of blue- and redshifted emission of the CO 2–1 line overlaid onto the 1.3 mm continuum emission (gray contours; see Figure 4.1). Blue contours indicate intensities integrated over the velocity range from 5.8 km s^{-1} to 80.1 km s^{-1} while red contours represent that from 103.7 km s^{-1} to 172.2 km s^{-1}. Contours range from 5σ to 30σ at

width of the CH_3OH 22_4–21_5 E line (FWHM=6.3 km s^{-1}). The velocity ranges of the blue- and red-shifted components are defined as from 59.2 km s^{-1} to 80.1 km s^{-1} and from 103.7 km s^{-1} to 157.7 km s^{-1}, respectively, for the SiO 5–4 line. The red-shifted emission has a larger velocity range by a factor of 2.6 than that of the blue-shifted one.

Figure 4.4 shows the integrated intensity maps of the SiO 5–4 line. There are at least two SiO outflows in G25.82; the north–south (N–S) outflow and the southeast–northwest (SE–NW) outflow, both of which have red-shifted dominant structures. The N–S SiO outflow originates from a position ~0.2″ northwest of G25.82–W1 and has an extent of about 12″. Its total velocity range is from 52.9 km s^{-1} to 157.7 km s^{-1}. Blue-shifted and redshifted emission exhibit knotted, curved structure, extending to the north and south, respectively. The SiO emission of this SE-NW outflow is very weak but still significant ($> 5\sigma$). The blueshifted (SE) and redshifted (NW) components can be seen in the integrated intensity map with the velocity ranges of 75.4−80.1 km s^{-1} and 103.7−146.9 km s^{-1}, respectively. The SE–NW SiO outflow originates from a position separated at least ~0.8″ to the south from the three continuum sources and extends about 17″. Further analysis of other outflow tracers such as the CO lines will be helpful to investigate more detailed nature of the SE-NW SiO outflow. In addition to these bipolar structures, one red-shifted condensation having a high intensity of 12σ can be seen in the velocity range from 103 km s^{-1} to 113 km s^{-1} at the north of G25.82–W, which is labeled as N Knot in Figure 4.4.

CH_3OH 8_{-1}–7_0 E

The CH_3OH line at 229 GHz, CH_3OH 8_{-1}–7_0 E, is also detected toward G25.82. This line is predicted to be a a class I methanol maser (Slysh et al., 2002). Nevertheless, the line profile of the CH_3OH 8_{-1}–7_0 E line emission in G25.82 shows a mixture of maser and thermal emission (Figure 4.5). The line width of the CH_3OH 8_{-1}–7_0 E spectrum integrated over the whole G25.82 region is comparable to that of the CH_3OH 22_4–21_5 E line emission (upper panel in Figure 4.5). Weak wing emission is also found in the profile of the CH_3OH 8_{-1}–7_0

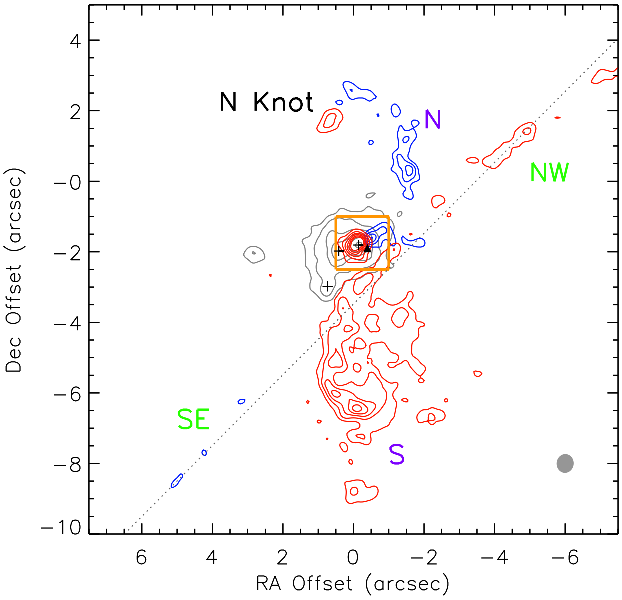

Figure 4.4: Integrated intensities of blue- and redshifted emission of the SiO 5–4 line overlaid onto the 1.3 mm continuum emission (gray contours; see Figure 4.1). Blue contours indicate intensities integrated over the velocity range from 59.2 km s^{-1} to 80.1 km s^{-1} while red contours represent that from 103.7 km s^{-1} to 157.7 km s^{-1}. Contours range from 5σ to 30σ with the intervals of 5σ, where 1σ for blue and red components are 9.8 mJy $beam^{-1}\cdot$ km s^{-1} and 18 mJy $beam^{-1}\cdot$ km s^{-1}, respectively. Positions of G25.82–W1, W2, and W3 are marked with black crosses while that of the H_2O maser spot at 80.5 km s^{-1} is denoted by a black triangle. The dotted line indicates the outflow axis of SE–NW SiO outflow. The orange box indicates the area shown in Figure 4.8. The filled gray circle in the right bottom corner denotes the synthesized beam size of the SiO map. The absolute positional uncertainties of water maser features are in all cases < 1 mas. In addition, that of ALMA Cycle 3 observations is less than 0.01″.

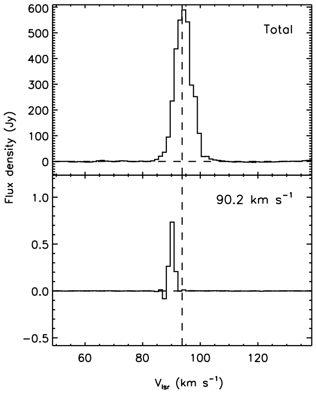

whole emitting region (*top*) and a compact component at a central velocity of 90.2 km s^{-1} (*bottom*). The vertical dashed lines and the horizontal dashed lines represent the systemic velocity (93.7 km s^{-1}; Wienen et al., 2012) of G25.82 and the zero baseline, respectively.

Figure 4.5: Spectra of the CH_3OH 8_{-1}–7_0 E line integrated over the

E line. Compact components of the CH_3OH 8_{-1}–7_0 E line are identified by Gaussian fits to the image. The spectrum of a spatially compact feature at a central velocity of 90.2 km s^{-1}, which is marked with a cross in Figure 4.6, is shown in the lower panel of Figure 4.5. It shows a narrower line width (~2 km s^{-1}) compared to that of the total spectrum. Due to insufficient spatial and spectral resolution, we could derive only the lower limit to the brightness temperature of >240 K using the peak flux of the compact feature.

The distribution of the CH_3OH 8_{-1}–7_0 E line is presented in Figure 4.6 (orange contours). Its extended structure (~15$''$) appears similar to the SiO 5–4 line emission in channels close to the systemic velocity of 93.7 km s^{-1}. In addition to the overall extended structure, there are compact features of CH_3OH 8_{-1}–7_0 E emission with a size of 1$''$ or less. These class I CH_3OH maser features appear to trace lower velocity outflowing gas than that traced by the SiO emission. It suggests that the class I CH_3OH maser at 229 GHz are likely tracing weaker or older shocks compared to the SiO emission (e.g., Yanagida et al., 2014).

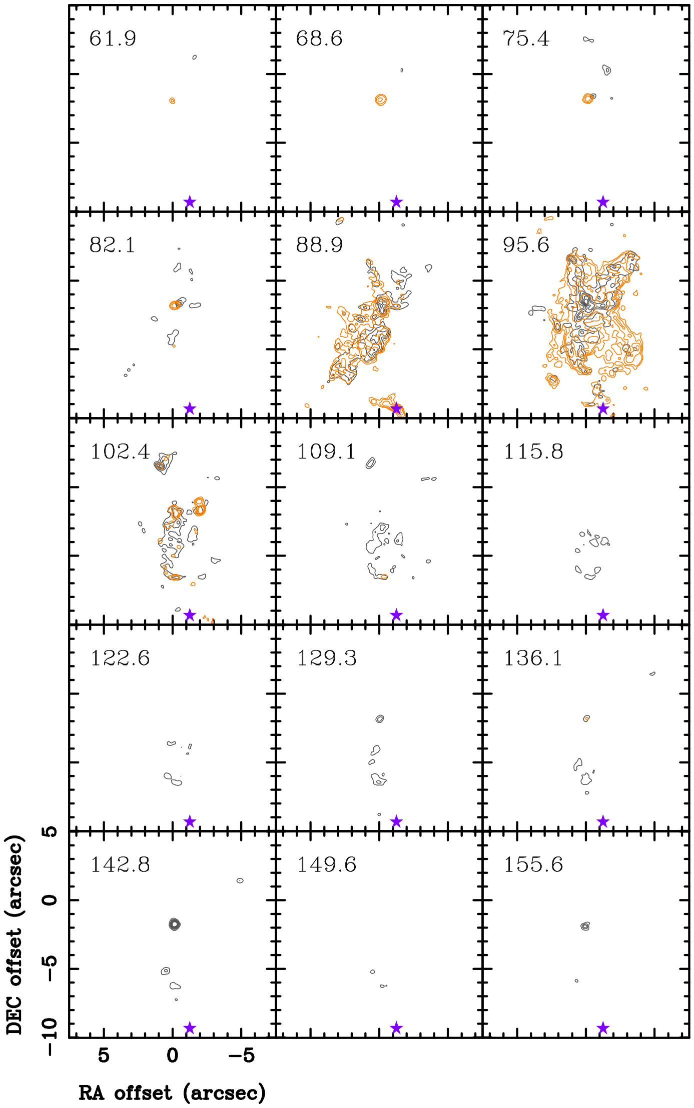

Figure 4.6: Distribution of integrated intensities of the SiO 5–4 (gray contours) and the CH_3OH 8_{-1}–7_0 E (orange contours) lines. Gray contours start from 5σ to 30σ with the increasing interval of 5σ, where 1σ is 1.4 mJy beam^{-1}. Orange contours indicate 5σ, 20σ, and 80σ, where 1σ is 1.4 mJy beam^{-1}. The compact features seen in orange contours at (0″, -2″) at the velocities from 61.9 km s^{-1} to 82.1 km s^{-1} and 136.1 km s^{-1} are contamination from the other molecular lines close to the frequencies of the SiO 5–4 line. Numbers in the upper left of each panel are respective velocities in km s^{-1}. A purple star denotes the position of the compact structure shown in the bottom panel of Figure 4.5.

H_2O Masers

Several H_2O maser features are identified toward G25.82–W1. The 22 GHz H_2O maser is often detected in the innermost (< 1000 au) regions of shocked outflowing gas from the central protostar (e.g., Goddi et al., 2007; Chibueze et al., 2014; Moscadelli et al., 2016; Burns et al., 2017). Hereafter we call the outflow traced by these H_2O masers the "H_2O maser outflow". The velocity range of detected maser features is from 41.5 km s^{-1} to 98 km s^{-1} (Figure 4.7). The absolute position of the 80.5 km s^{-1} feature determined by VERA is (α,δ)=($18^h39^m03^s.60$, -06°24′11″.4) which is also used to astrometrically register the KaVA maser map (Figure 4.8). The positional errors of water maser features determined using VERA astrometry data are, in all cases, less than 1 mas. A compact distribution is shown in the southwest part of G25.82–W1 with an offset of 0″.25 (~1100 au). Most of the maser spots are distributed within a 0″.2 area except one spot at 41.5 km s^{-1}, which is located 0″.2 southeast from the 80.5 km s^{-1} component. Within the 0″.2 area, the most red-shifted component (98.0 km s^{-1}) is located closest to the position of G25.82–W1 while the most blue-shifted component (77.3 km s^{-1}) is located on the southwestern side. The velocity structure of the H_2O maser outflow is not consistent with those of other outflow tracers.

CH_3OH 22_4–21_5 E

Channel maps of CH_3OH 22_4–21_5 E line emission and the integrated intensity map are shown in Figure 4.9 and Figure 4.10, respectively. The 230 GHz CH_3OH line emission shows a compact (~1″) circular distribution at the continuum peak of G25.82–W1. There are no emission peaks at G25.82–W2 or W3. However, the peak positions of individual channels are not exactly coincident with that of the 1.3 mm continuum of G25.82–W1. This ring-like structure with a velocity gradient can be found in the intensity-weighted mean velocity (moment 1) map as shown in Figure 4.11. The velocity gradient ranges from 90.2 km s^{-1} to 96.1 km s^{-1} within a diameter of about 1″, which corresponds to 5000 au. Overall, the 230

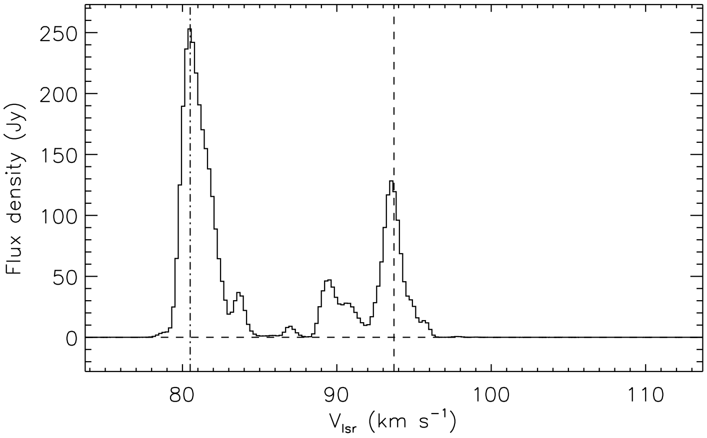

Figure 4.7: Scalar averaged cross-power spectrum of the 22 GHz H_2O maser line toward G25.82. The vertical dashed line and the horizontal dashed line represent the systemic velocity of the source and zero baseline, respectively. The dash-dotted line indicates the velocity channel used as a reference for phase referencing analysis (triangle in Figure 4.4).

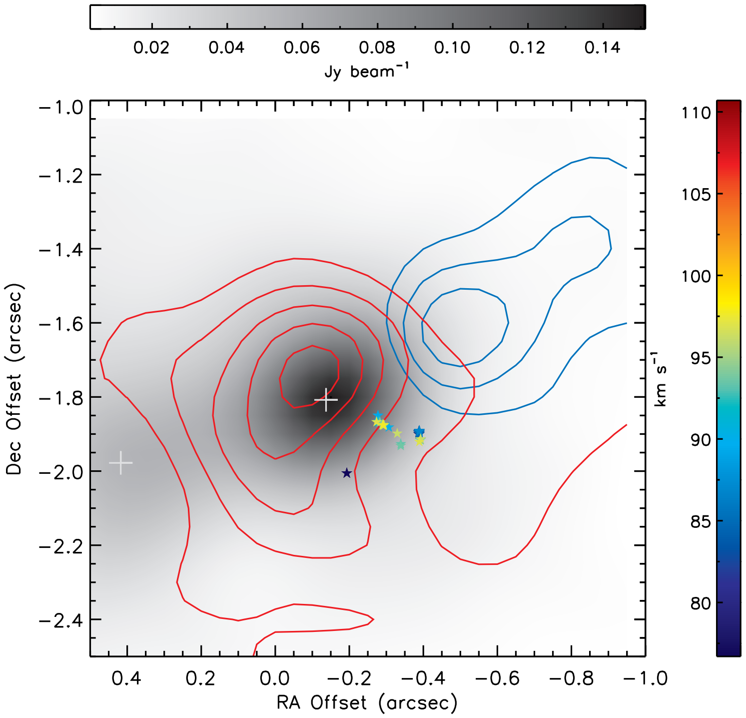

Figure 4.8: Distribution of the 22 GHz H_2O masers obtained with KaVA overlaid onto ALMA 1.3 mm continuum emission (gray scale). Blue and red contours indicate the integrated intensity map of the SiO 5–4 line as presented in Figure 4.4. Blue contours range from 5σ to 15σ having the intervals of 5σ with the 1σ level of 9.2 mJy beam^{-1}· km s^{-1} while red contours range from 5σ to 25σ having the same intervals with the 1σ level of 16 mJy beam^{-1}· km s^{-1}. Stars denote H_2O maser spots having the same velocities in the color bar. The bluest feature at 41.5 km s^{-1} at (−0.2, −2.0) is out of range of the color bar. Crosses denote the positions of the 1.3 mm continuum sources, G25.82–W1 and G25.82–W2. The absolute position errors of water maser features are in all cases < 1 mas. In addition, that of ALMA Cycle 3 observations is less than 0.01″.

GHz CH_3OH line emission appears to trace a rotating disk or envelope around G25.82–W1.

4.4 Discussions

4.4.1 Mass Estimation

Because there is no infrared or centimeter radio continuum source in G25.82–W, we assume all the continuum emission at 1.3 mm is thermal dust emission. Assuming the emission is optically thin graybody radiation, we can derive the total enclosed mass (gas+dust), $M_{\rm total}$, using the following equation:

$$M_{\rm total} = \frac{S_\nu D^2}{\kappa_\nu B_\nu(T_{\rm dust})}. \tag{4.1}$$

The 1.3 mm integrated flux, S_ν, in Table 1 for G25.82–W1 (377 mJy) is used and D is the adopted distance of 4.44 kpc. Since the millimeter/submillimeter continuum data at other wavelengths is not available for this source, dust temperature ($T_{\rm dust}$) is assumed to be 150 K with an uncertainty by a factor of 2 (75 K - 300 K). This assumed dust temperature is adopted from measurements toward typical hot molecular cores since G25.82–W is one of the hot molecular cores as described in Section 4.4.2 (Beuther et al., 2017; Beltrán et al., 2018b). B_ν is the Planck function for a blackbody of temperature $T_{\rm dust}$. For the mass opacity coefficient, we adopted $\kappa_\nu = 0.1(250\mu m/\lambda)^\beta$ cm^{2}g^{-1} from Hildebrand (1983) with $\beta = 1.85$ from the dust model of Ossenkopf & Henning (1994). The total mass is estimated to be 16 $M_\odot$-66 $M_\odot$ assuming the gas to dust mass ratio of 100. The luminosity can also be estimated using the above assumptions and the following relation (Scoville, & Kwan, 1976; Zhang et al., 2007);

$$T_{\rm dust} = 65\left(\frac{0.1\ {\rm pc}}{R_{\rm s}}\right)^{2/(4+\beta)}\left(\frac{L}{10^5\ L_\odot}\right)^{1/(1+\beta)}\left(\frac{0.1}{\kappa_\nu}\right)^{1/(4+\beta)} K. \tag{4.2}$$

Here $R_{\rm s}$ is the source radius in pc. Using a source size of 0.005 pc (0.22″), the luminosity of G25.82–W1 is estimated to be $\sim 1.3 \times 10^4$ $L_\odot$ corresponding to a B0.5 star having a stellar mass of 12.7 $M_\odot$ (Mottram et al., 2011).

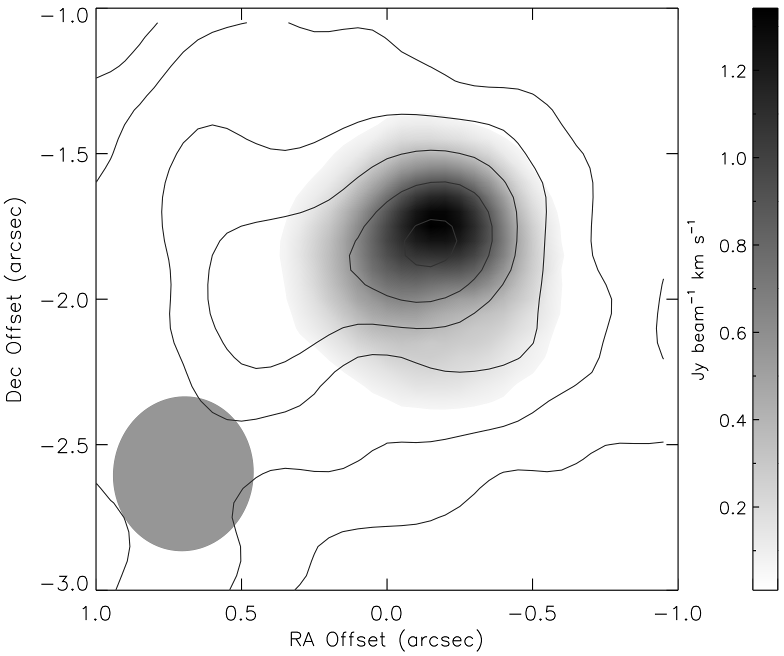

Figure 4.9: Integrated intensity map of the CH$_3$OH 22_4–21_5 E line (gray scale). Contours show the distribution of the 1.3 mm continuum emission. Contour levels are 10σ, 20σ, 40σ, 80σ, 160σ, and 320σ, where 1σ is 0.4 mJy beam^{-1}. The filled gray circle in the bottom left corner indicates synthesized beam size. The absolute position errors of water maser features are in all cases < 1 mas. In addition, that of ALMA Cycle 3 observations is less than $0.01''$.

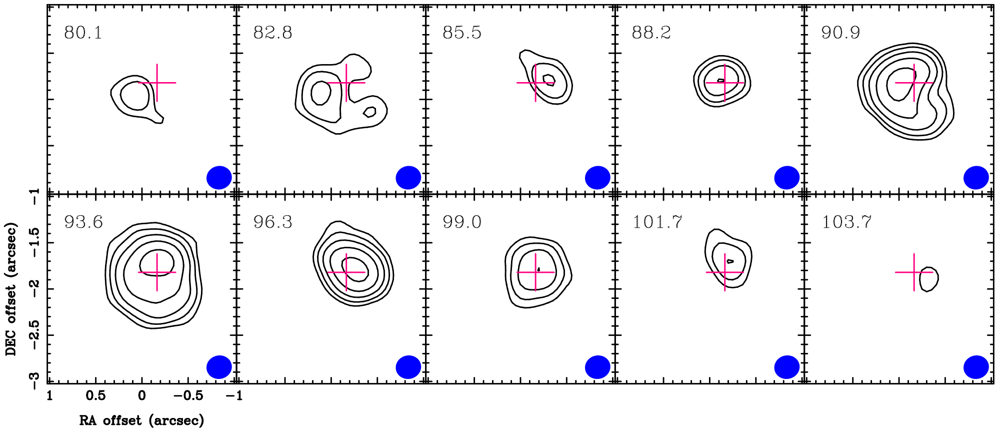

Figure 4.10: Channel maps of the CH_3OH 22_4–21_5 E line. Respective velocities in km s^{-1} are presented in the upper left of each panel. Contours show the 5σ, 10σ, 20σ, 40σ, and 80σ levels, where 1σ is 1.24 mJy $beam^{-1}$. Cross denotes the position of G25.82–W1. The filled blue circle in the right bottom corner presents the synthesized beam size in the CH_3OH 22_4–21_5 E line map.

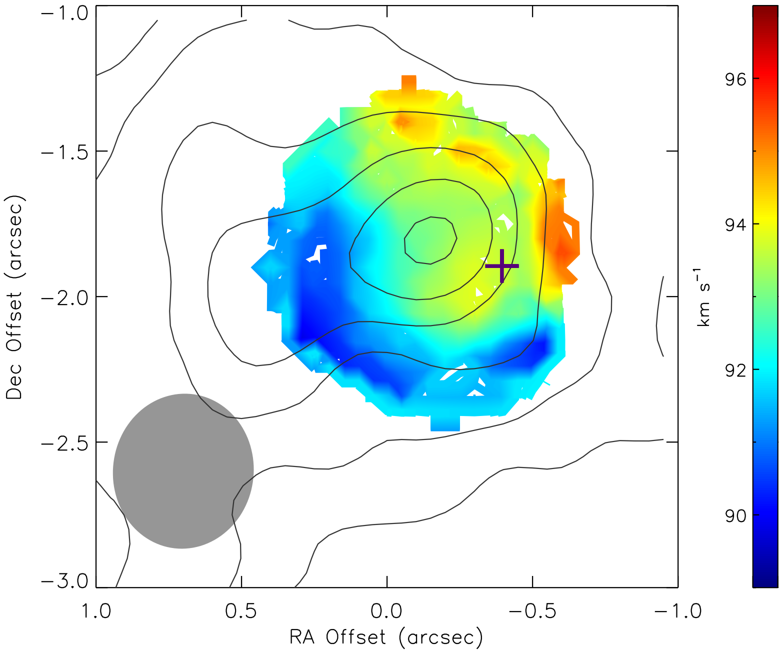

Figure 4.11: The moment 1 map of the CH_3OH 22_4–21_5 E line (color scale). Contours show the distribution of the 1.3 mm continuum emission. Contour levels are 10σ, 20σ, 40σ, 80σ, 160σ, and 320σ, where 1σ is 0.4 mJy beam^{-1}. A purple cross denotes the absolute position of the H_2O maser feature at 80.5 km s^{-1}. The filled gray circle in the bottom left corner indicates synthesized beam size. The absolute position errors of water maser features are in all cases < 1 mas. In addition, that of ALMA Cycle 3 observations is less than 0.01″.

As for G25.82–W2 and W3, there is no molecular emission peak at any of them suggesting that there is no heating source (or embedded YSO) in each of them. Therefore, we here assume that they are starless cores. The derived masses of these cores are 280 $M_\odot$ and 77 $M_\odot$, respectively, adopting a 15 K dust temperature for starless massive dense cores (Russeil et al., 2010).

Dynamical mass of the central protostar can be estimated assuming that the 230 GHz CH_3OH line emission arises from an edge-on rotating structure with the Keplerian rotation,

$$M = \frac{Rv^2}{G}, \tag{4.3}$$

where G is the gravitational constant, R is the radius of the 230 GHz CH_3OH 22_4–21_5 E line emission of 2200 au ($0''.5$) and v is the velocity difference within R of 3 km s^{-1}. The derived mass is 23 ± 10 $M_\odot$ in the case of the edge-on geometry. The uncertainty in dynamical mass includes the fractional errors of the measured radius mainly caused by the uncertainties distance (10%) and the velocity difference of 0.65 km s^{-1}(23%). The measurement error in defining the size of radius is small compare to that in the distance. Our mass estimate is a lower limit because the inclination of the disk is unknown. Thus, G25.82–W1 is very likely a high-mass protostellar object.

4.4.2 Evolutionary phases of G25.82–E and G25.82–W

G25.82 is composed of two regions, G25.82–E and G25.82–W. G25.82–E is the weakest 1.3 mm continuum condensation in G25.82. There is one WISE 22 μmsource, J183903.80-062411.0, in the vicinity of G25.82–E. In addition, a radio continuum source was also detected in this region using the VLA (Hu et al., 2016). Considering the spatial resolution of the VLA observations (~ $3''$), the radio continuum source appears to be associated with G25.82–E. In the ultra-compact HII (UCHII) region phase, the free-free radiation is the dominant source of the centimeter radio continuum emission from central HM-YSOs. Spatial association with far-infrared (FIR) and centimeter radio continuum sources suggests that G25.82–E is at an evolved stage such as an UCHII region. The weak 1.3 mm continuum emission of G25.82–E suggests the destruction of dust grains by UV radiation from the central HM-YSO. Furthermore, there is no signpost of mass accretion traced by molecular lines such as outflows or rotating/accreting material around the HM-YSO.

On the other hand, G25.82–W is an infrared dark region. Even at the WISE 22 μm, there is no counterpart. Moreover, radio continuum emission is not detected toward this region (Hu et al., 2016). However, multiple outflows in different scales are identified in the present study. The N–S SiO outflow, the SE–NW SiO outflow, and H_2O maser outflow are driven by YSOs in G25.82–W. Outflows are strong evidence that the accretion process is ongoing in this region. Therefore it follows that G25.82–W is in an earlier evolutionary stage than G25.82–E.

4.4.3 Outflows in G25.82–W

Within G25.82–W, there are at least three potential sites of star formation; an HM-YSO, G25.82–W1, and two starless cores, G25.82–W2, and G25.82–W3. The size of this region is determined by the 10σ contour level in the 1.3 mm continuum map to be about $2''$or 0.05 pc. This is smaller than the typical size of massive dense cores, 0.1−0.2 pc (Motte et al., 2017). Clustered formation in this small region is also suggested by the existence of multiple outflows.

Here we discuss that the N1–S1 CO outflow (N–S SiO outflow) is most likely driven by G25.82–W1 as it is located at the center of blue- and red-shifted components. In addition, a rotating structure is also detected toward G25.82–W1. The velocity gradient shown in the moment 1 map of the CH_3OH 22_4–21_5 E line traces a rotating disk or envelope around G25.82–W1. Therefore, it is likely that G25.82–W1 hosts an embedded HM-YSO.

In the case of the SE–NW CO outflow (SE–NW SiO outflow), the driving source cannot be determined based on the morphology of CO (SiO) outflows and the distribution of continuum sources at the resolution of the ALMA data presented here. Moreover, no signs of star formation in G25.82–W2 and W3 suggests that they have less possibility to be the driving source of the SE–NW CO (SiO) outflow. In addition, the existence of a potential companion is suggested by the spatial inconsistency between the H_2O maser and the 1.3 mm continuum peak if the H_2O maser outflow were to be tracing another small scale outflow not associated with the SiO outflows. However, we cannot rule out the possibility that the H_2O maser outflow is tracing the inner part of the large scale outflow (N1–S1 CO outflow and N–S SiO outflow). If this is the case, the inconsistency of velocity structure of H_2O maser outflow and N1–S1 CO outflow and/or N–S SiO outflow could be interpreted by the difference in physical structures traced by each tracer. In other word, the H_2O maser outflow may be the interior of outflowing gas in the vicinity of G25.82-W1 (Figure 4.12).

As described in Moscadelli et al. (2019), magneto-centrifugal disk winds (MC DWs) are considered the most likely way for acceleration of protostellar jets. Considering the radius, where the H_2O masers are distributed, is about $0.2''$ and the dynamical mass is 25 $M_\odot$, the escape velocity, $v_{\mathrm{escape}} = \sqrt{\frac{2GM}{r}}$, is estimated as 6.3 km s^{-1}. The line-of-sight velocities of 27 among 57 H_2O maser features are smaller than the escape velocity (Figure 4.8). However, considering the proper motion of H_2O maser almost all of H_2O features are moving out with higher velocity then escape velocity (see Figure 3.7, Figure 4.8, and Figure 4.12). Thus, the H_2O maser are indeed tracing the innermost region of the outflow.

There are potential HM-YSOs in G25.82–W, G25.82–W1 and a possible companion hosting the SE–NW CO (SiO) outflow. In addition, high-mass starless/protostellar core candidates are also detected, G25.82–W2 and G25.82–W3. In contrast, low-mass starless/protostellar cores are not detected outside the continuum emission source G25.82–W considering the sensitivity of continuum emission at 1.3 mm (5σ ~2 mJy beam^{-1}~0.5 $M_\odot$) which is high enough to detect low-mass cores. This implies that these HM-YSOs formed in isolation as predicted by the turbulent core accretion model (e.g., CygX-N53-mm2 Duarte-Cabral et al. (2013), G11.92-0.61-MM2 Cyganowski et al. (2014), and C9A Kong et al. (2017)). If this is the case, high-mass star formation in G25.82 is likely a scaled-up version of low-mass star forma-

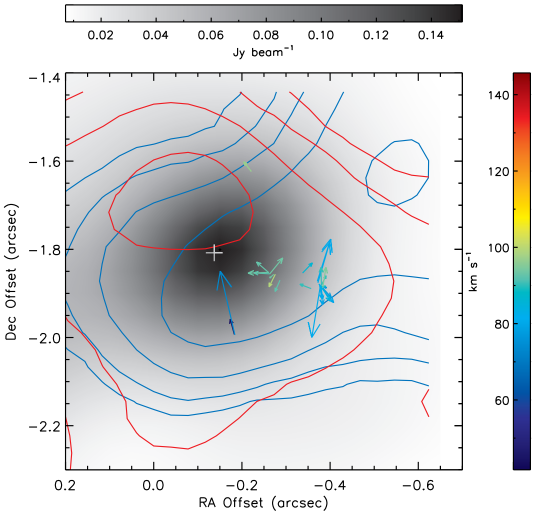

Figure 4.12: Proper motions of the 22 GHz H_2O masers obtained with KaVA overlaid onto ALMA 1.3 mm continuum emission (gray scale). Blue and red contours indicate the integrated intensity map of the CO 2–1 line as presented in Figure 4.3. Blue contours range from 5σ to 15σ having the intervals of 5σ with the 1σ level of 9.2 mJy beam^{-1}· km s^{-1} while red contours range from 5σ to 25σ having the same intervals with the 1σ level of 16 mJy beam^{-1}· km s^{-1}. Stars denote H_2O maser spots having the same velocities in the color bar. Cross denote the positions of the 1.3 mm continuum source, G25.82–W1. The absolute position errors of water maser features are in all cases < 1 mas. In addition, that of ALMA Cycle 3 observations is less than $0.01''$.

tion where the material accretes onto the YSOs through an accretion disk within a monolithic core. Because of the limited spatial resolution of our ALMA data, we cannot exclude the possibility that there are embedded/unresolved low-mass cores in G25.82–W even though the sensitivity is enough. This work promotes the G25.82 region as a valuable laboratory for future investigations of high-mass star formation.

4.4.4 Calculation of physical parameters of the N1–S1 CO Outflow

Although the determination of outflow parameters contains a large number of errors, rough estimation can be made. The physical parameters of the the N–S CO outflow are calculated following the method shown in Beuther et al. (2002a). To estimate the H_2 column density, the CO 2–1 line is assumed to be in local thermodynamic equilibrium (LTE). Therefore, the excitation temperatures ($T_{\rm ex}$) in all levels are the same. The $T_{\rm ex}$ of the outflow lobes, is adopted as 35 K (e.g. Shepherd & Churchwell, 1996; Henning et al., 2000; Beuther et al., 2002a). The column density of CO under the assumption of optically thin emission ($\tau \ll 1$), can be estimated with the integrated intensity (Schnee et al., 2007) as

$$N(\mathrm{CO}) = \frac{8k\pi\nu^2}{hc^3A_{21}}\frac{\exp(-E_2/kT_{\rm ex})}{(2J+1)}Q(T_{\rm ex})\int T_{\rm mb}dv. \tag{4.4}$$

where ν is the frequency of the transition, 230.530 GHz, A_{21} is the Einstein coefficient of $6.910\times10^{-7}\ s^{-1}$, $Q(T_{\rm ex})$ is the partition function, c is the light speed, and E_2 is the upper state energy of the CO 2–1 line. In addition, h and k are the Planck's constant and the Boltzmann's constant. Finally, the H_2 column density is converted using the abundance ratio of the molecule x and H_2 with the abundance of $X(x)$:

$$N(\mathrm{H_2}) = \frac{N(x)}{X(x)}\ \mathrm{cm}^{-2}. \tag{4.5}$$

The CO abundance, $X(\mathrm{CO})$, of 10^{-4} is used.

By integrating the emission within the velocity ranges which are the same as that of outflow map (Figure 4.3), the total H_2 column densities of each outflow lobes, $N_{\rm b/r}$ (blue or red) can be estimated. These column densities are used to calculate the mass of each lobe:

$$M_{\mathrm{b/r}} = (N_{\mathrm{b/r}} \times A_{\mathrm{b/r}}) \times \mu \, m_{\mathrm{H_2}} \, M_{\odot}. \tag{4.6}$$

$A_{\mathrm{b/r}}$ is the surface area of each lobe, $m_{\mathrm{H_2}}$ is the mass of a hydrogen molecule, and μ is a mean molecular weight of 2.37 per "free particle" (H_2 and He). The surface area is defined as the area covered by the 5 σ noise level contour and calculated by summing the total number of pixels in each lobe. Finally, the total mass M_{outflow} is obtained by adding that of each lobe:

$$M_{\mathrm{outflow}} = M_{\mathrm{b}} + M_{\mathrm{r}}. \tag{4.7}$$

The outflow mass of N1–S1 CO outflow, M_{outflow} is 0.1 $M_{\odot}$.

For the outflow velocity, the maximum velocity offset from the systemic velocity is employed which is one of the most common methods in the literature. By testing several different analysis methods, van der Marel et al. (2013) revealed that all methods, including the use of the maximum velocity, agree with each other within a factor of 6. Using the outflow velocities, $v_{\mathrm{max_b}}$ and $v_{\mathrm{max_r}}$, which are the maximum velocities of outflow lobes relative to the LSR velocity of G25.82 (93.7 km s^{-1}), the outflow momentum p and energy E calculated using:

$$P = M_{\mathrm{b}} \times v_{\mathrm{max_b}} + M_{\mathrm{r}} \times v_{\mathrm{max_r}} \tag{4.8}$$

$$E = \frac{1}{2} M_{\mathrm{b}} \times v^2_{\mathrm{max_b}} + \frac{1}{2} M_{\mathrm{r}} \times v^2_{\mathrm{max_r}} \tag{4.9}$$

The estimated P and E of N1–S1 CO outflow are 6.9 $M_{\odot}$ km s^{-1} and 5.8×10^{45} erg, respectively. The outflow mass is the only velocity-independent variable and thus the only one not affected by inclination angle. Considering the mean inclination angle of ∼57°.3 in Bontemps et al. (1996), a constant scaling of ∼1.85 ($1/\cos((\theta))$) for momentum and ∼3.43 ($1/\cos^2((\theta))$) for energy are expected. Therefore, it does not change the relative relationships between source luminosity and the outflow parameters.

In order to calculate the dynamical time-scale, $t_{\rm dyn}$, The maximum length of outflow, $l_{\rm max}$ is measured and it is $11''$. Downes & Cabrit (2007) reported that calculating $t_{\rm dyn}$ by dividing $l_{\rm max}$ by $\rm v_{max}$ is the best 'classical' way and proved by the previous surveys (Beuther et al., 2002a; Maud et al., 2015). Using this length, $t_{\rm dyn}$ is calculated as

$$t_{dyn} = \frac{l_{\rm max}}{(v_{\rm max_b} + v_{\rm max_r})\,/\,2}. \tag{4.10}$$

The $t_{\rm dyn}$ of N1–S1 CO outflow is 2.8×10^3 yr.

The mass-loss rate of the molecular outflow $\dot{M}_{\rm outflow}$, the mechanical force $F_{\rm m}$, and the mechanical luminosity $L_{\rm m}$ are calculated using

$$\dot{M}_{\rm outflow} = \frac{M_{\rm outflow}}{t_{\rm dyn}} \tag{4.11}$$

$$F_{\rm m} = \frac{p}{t_{\rm dyn}} \tag{4.12}$$

$$L_{\rm m} = \frac{E}{t_{\rm dyn}}. \tag{4.13}$$

The physical parameters of the N1–S1 CO outflow are summarized in Table 4.3. The outflow parameters of the N1–S1 CO outflow are smaller than that from the previous survey on this target (de Villiers et al., 2014). The properties of the N1–S1 CO outflow have smaller values than that of $\rm C^{18}O$ outflow from de Villiers et al. (2014) obtained with James Clerk Maxwell Telescope (JCMT). In case of de Villiers et al. (2014), a kinematic distance of 5 kpc (Green & McClure-Griffiths, 2011) was used. For outflow mass which is proportional to volume, it was overestimated by a factor of 1.4 compared to outflow mass from this work. However, still all outflow mass, momentum, and energy are smaller from de Villiers et al. (2014) even considering the difference in distance. Difference between the mass from this work and de Villiers et al. (2014) comes from the different scale that two observations can trace. It is also likely that emission observed with ALMA could be resolved out, resulting in weaker intensity. On the other hand, the time-dependent properties (mass loss rate, force, and luminosity) of the N1–S1 CO outflow are following the similar relationships with source luminosity reported by Maud et al. (2015, see Figure 5). The small scale outflow revealed by the ALMA observations is a part of the large scale outflow observed by single-dish telescope. The correlation of these parameters in both small and large scale outflow would imply that the driving mechanism are common for entire scale of the outflow.

In addition, the total outflow force versus luminosity is presented in Figure 4.13. It includes the total outflow force of each outflows associated with HM-YSOs from Maud et al. (2015), Class 0 and Class I low-mass YSOs from Bontemps et al. (1996), and ~Class I low-mass sources from van der Marel et al. (2013). It should be noted there are more samples having outflow force information (e.g. Beuther et al., 2002a; Wu et al., 2004); however, these are not used in the plot because some sources lake the luminosity information and many different methods were used to calculate the outflow parameters. For consistency, a factor of ~2.9 has been applied to outflow forces associated HM-YSOs including G25.82–W1 to scale for an average inclination angle (57°.3) used in Bontemps et al. (1996). The continuity between the low-mass and high-mass samples was confirmed by Maud et al. (2015) and the outflow force of G25.82–W1 also follows this trend. By extending the best-fitting result to the low-mass source of Bontemps et al. (1996), $\log F_{\rm m} = -5.6 + 0.9 \times \log L_{\rm source}$, intersects with HM-YSOs and lies slightly below the low-mass YSOs. G25.82–W1 is also located slightly lower region than the solid line. It suggests that a similar process is expected for outflows in HM-YSOs and the lower mass regime. However, it is hard to determine which mechanism is most likely to drive outflows in G25.82 (e.g. Maud et al., 2015). The relationship shown here supports that the star-forming mode in G25.82 is likely a scaled-up version of that in low-mass star formation.

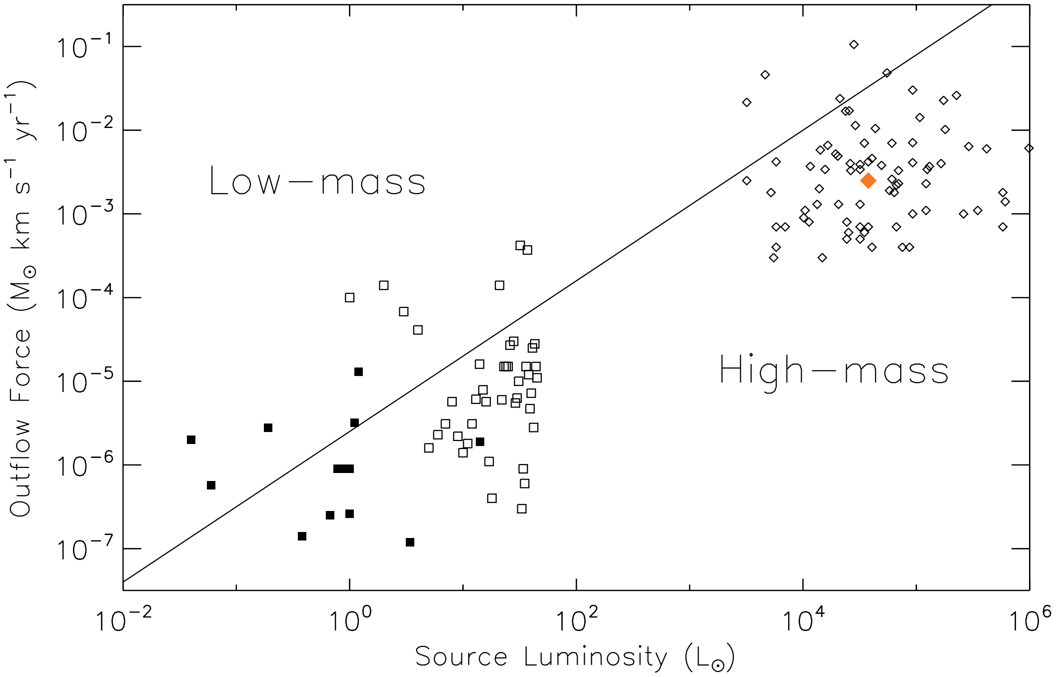

Figure 4.13: Outflow force F_{m} versus luminosity for G25.82 with HM-YSO samples (D < 6 kpc) from Maud et al. (2015). The open diamonds represent the force of HM-YSOs from Maud et al. (2015) whlie a filled orange diamond denotes that of G25.82–W1. The filled squares are Class 0 and Class I low-mass sources from Bontemps et al. (1996) while the open squares are the ~Class I sources from van der Marel et al. (2013). The black solid line presents the linear trend of outflow force with luminosity from Bontemps et al. (1996).

Table 4.3. Physical Parameters of N1–S1 CO outflow

Quantity	Units	This work	de Villiers et al. (2014)
Mass	$M_\odot$	0.1	25
Momentum	($M_\odot$ km s^{-1})	6.9	190
Energy	($\times 10^{45}$ erg)	5.8	92
Mass-loss rate	($\times 10^{-5}$ M$_\odot$ yr^{-1})	2.9	60
Force	($\times 10^{-3}$ M$_\odot$ km s^{-1} yr^{-1})	2.5	4.3
Luminosity	($L_\odot$)	17	17
Dynamical time scale	($\times 10^{3}$ yr)	2.8	44

Chapter 5

Conclusions and Future prospects

This thesis presents the circumstellar structure in the vicinity of G25.82–0.17 in the early stage of high-mass cluster formation associated with masers. Data from several interferometric observations using the KaVA, VERA, and ALMA is used to understand star-forming environments by analyzing connection between structures traced by masers with that by thermal and continuum emission.

As aimed in the first place, this thesis has (1) revealed the star-forming environment that the HM-YSOs associated with masers have, (2) figured out where the H_2O masers are excited in the circumstellar structure, (3) clarified the spatial and spectral structure of outflow that can be traced by Class I CH_3OH masers based on the observational results of G25.82.

1. High-mass cluster formation in G25.82 is revealed by using KaVA, VERA, and ALMA. Multiple 1.3 mm continuum sources are resolved, indicating the presence of YSOs. In addition, the evolutionary stages of YSOs are different determined by comparison with infrared, radio continuum and thermal line emission. Moreover, class I CH_3OH and H_2O masers are associated with YSOs (G25.82-W) in the earlier stage than UCHII region (G25.82-E).

2. In G25.82-W, outflows tracing different scales from the W1, having disk-like structure

around, were detected. The smallest scale of view of outflow was by H_2O maser observation. The H_2O maser is likely to trace the innermost interior of the blueshifted gas of N–S outflow. The result suggests that the outflow is launched with a wide opening angle in the first place from the disk around G25.82-W1 similar to outflow driven by disk wind (e.g. Moscadelli et al., 2020).

3. SiO and class I CH_3OH masers trace the smaller scale and narrower velocity range of outflow than CO. Furthermore, Class I CH_3OH maser is tracing the lower velocity of outflow compare to the SiO line which has comparable distribution.

It is an observational proof of benefit to use maser species comprehensively because they trace different structure near the powering source.

Similar case study done for G25.82 will be done toward HM-YSOs with KaVA monitoring data and other thermal line and continuum emission data to fill up the evolutionary scenario for HM-YSOs. Dynamical information such as inclination of outflow can be derived by measuring proper motions of masers comprehensively (H_2O and class I CH_3OH masers) to earn accurate information on the accretion such as mass accretion rate for statistical study.

From KaVA LP (Chapter 2), summary of snapshot imaging survey of H_2O maser is presented to examine typical trend in spectral and spatial distributions of maser features and select appropriate target to investigate in detail. Results from analysis of H_2O masers toward 15 targets selected based on KaVA LP criteria are shown. Detected H_2O masers are divided into three groups by their spectral distribution (velocities of detected features). In total, three sources were classified as “blue" , two were as “red”, and ten sources were classified as “both". The H_2O masers in the “both” group are highly expected to trace bipolar outflows and isotropically expanding shells/winds while targets in “blue” and “red” would be tracing a part of those structures. To investigate the trend in the distribution of H_2O masers, morphology factor was defined as $\alpha = l_{\rm max}/l_{\rm min}$ where $l_{\rm max}$ and $l_{\rm min}$ are major size and minor size of H_2O maser distribution, respectively. These 10 targets in “both” group are largely divided into two groups: a "compact" distribution group and an "elongated" distribution group. The major axis is estimated from the distribution map. Since information on accurate distance is not provided for all sources, therefore, direct comparison between the linear scale is not available. However, the ratio of major and minor axis (morphology factor) provides a hint on the morphology of H_2O maser distribution source to source. Five sources, including G25.82–0.17, one of targets having the largest morphology factor, are classified as "compact" while others are in "elongated" group. "Elongated" structure may trace bipolar outflows with high possibility while "compact" structure is hard to imagine what kinds of dynamical structures can be traced. To examine the environmental difference between these two groups, the 3D velocity structures of H_2O masers are going to be obtained with monitoring observations. Based on the results from the imaging survey, monitoring observations were done including G25.82-0.17.

G25.82-0.17, one of targets having the largest morphology factor of 0.4, is selected for the pilot case study from the KaVA LP as the first step to KaVA LP ultimate goals since it shows about 60 features with 60 velocity range, suggesting it is a good laboratory to investigate the connection between the dynamical structures in the vicinity of the powering source and H_2O maser 2D and 3D distributions. In this thesis, analysis only for G25.82-0.17 is presented using the KaVA monitoring data while the 3D velocity structures for other sources is going to be derived eventually. It is very important for verification of technical and scientific aspects of KaVA LP studies at the same time before extending the research.

By taking full advantage of VERA and KaVA observations, parallax and proper motions of H_2O masers in G25.82 (Chapter 3) are measured to estimate accurate distance and 3D velocity structure of H_2O masers for further analysis. In addition, the galactic position and the peculiar motion of G25.82 is presented to compare with other high-mass star forming regions. The eight maser features have been successfully employed detected in more than five epochs. Obtained parallax is 0.225 ± 0.020 mas, corresponding to a distance of $4.44^{+0.4}_{-0.4}$ kpc. Estimated parallactic distance is ~70% of a kinematic distance of 6.7 kpc from Walsh et al. (1997) while it shows better agreement with a kinematic distance of 5 Kpc from Green & McClure-Griffiths (2011). In addition, it is comparable to a kinematic distance of 5 kpc estimated with the galactic parameters from the recent VERA astrometry catalog (VERA Collaboration et al., 2020). Our parallactic distance is a factor of 0.89 (=4.44 kpc/5.0 kpc) smaller than the kinematic distance. In addition, uncertainty is reduced to 10% of 89%. This parallactic distance is going to be used for further analysis toward G25.82 with thermal line and continuum emission which is shown in the next chapter. Since we measured the exact distance to G25.82, the first discussions on the dynamics of G25.82, introduced in the Chapter 4, was possible.

Internal proper motions of H_2O maser features in G25.82 were measured. Using the position of the 97.3 km s^{-1} feature as reference, we obtained the relative distribution of all detected H_2O maser features. In total, 21 H_2O maser features were identified which were detected at least in three epochs. Most of identified H_2O maser features have blueshifted or similar velocities to a systemic velocity of G25.82 (93.7 km s^{-1}). In addition to the bluest feature, slightly redshifted velocity component (97.1 km s^{-1} feature) moving toward the NE. Features having velocities close to the systemic velocity distributed at Dec offset$\sim$ 0 are moving away each other. The central cluster shows motions divided into two groups which are moving toward N and SW.

G25.82 is located on the “Scutum-Centaurus Arm” at the edge of “Long Bar” at the galactic center with the location in the middle of other neighboring high-mass star-forming regions. Therefore, G25.82 is also located at the part of Galaxy where the star formation is actively occurring. In addition to the galactic position, the peculiar motions of the maser source can be estimated by subtracting the effect of Galactic rotation and the peculiar motion of the Sun from the motion of the maser source. It may be strongly affected by the parallax uncertainty, we obtained the peculiar motion components of G25.82 to be (U_s, V_s, W_s) = (33, −9, 18).

To investigate the mechanism of high-mass star formation in the G25.82 region and compare with the 3D velocity structure made by H_2O maser observations, this thesis carried out 1.3 mm continuum and spectral line observations with ALMA and 22 GHz H_2O maser observations using KaVA and VERA (Kim et al., 2020). In the 1.3 mm continuum map, G25.82 is divided into two parts; G25.82–E and G25.82–W. G25.82–E is a compact and weak condensation being located close to a source of infrared and radio continuum. On the other hand, no infrared or radio continuum source is detected toward the other strong 1.3 mm continuum source, G25.82–W. Three 1.3 mm continuum condensations are identified, G25.82–W1, W2, and W3. The strongest 1.3 mm continuum peak is located at G25.82–W1.

In G25.82–W, three sets of blue- and redshifted lobes of CO are identified. One is outflow having relatively poorly collimated blue- and redshifted components at north and south, respectively (N1–S1 CO outflow). Second is well-collimated outflow with blue-shifted knots elongated to the SE of G25.82–W while red-shifted knots are located at the NW (SE–NW CO outflow). It cannot be ruled out that it is a part of N1–S1 CO outflow, the N2–S2 CO outflow is also identified as the third set. The axis of the SE–NW CO outflow is shifted at least $0''.8$ to the southwest from the 1.3 mm continuum sources.

In addition to CO outflows, two SiO bipolar outflows are also identified. One is relatively poorly collimated outflow having blue- and redshifted components at north and south, respectively (N–S SiO outflow). Both blue- and redshifted components show curved structures. It may trace the same but smaller scale of the N1–S1 CO outflow. The other shows weaker emission but still significant ($> 5\sigma$), extending in the southeast–northwest direction (SE–NW SiO outflow). Blue-shifted knots are elongated to the SE of G25.82–W while red-shifted knots are located at the NW. The axis of the SE–NW SiO outflow is also shifted to the southwest from the 1.3 mm continuum sources corresponding the SE–NW CO outflow.

Furthermore, the CH_3OH 8_{-1}–7_0 E line at 229 GHz is detected toward G25.82–W. The distribution of the CH_3OH 8_{-1}–7_0 E line shows a mixture of thermal and maser emission. The extended structure ($\sim$15 $''$) close to the systemic velocity shows a similar structure to that of the SiO 5–4 line emission in the same velocity ranges. In contrast, the 22 GHz H_2O masers are distributed at a position $0''.25$ shifted from that of G25.82–W1. The velocity distribution of the H_2O masers is not consistent with those of other outflow tracers.

In addition to outflowing structures, a ring-like structure is detected around G25.82–W1 (R ~2200 au) in the 230 GHz CH_3OH 22_4–21_5 E line emission map. The velocity gradient is detected centered at the position of the 1.3 mm continuum peak of G25.82–W1. It is likely tracing a rotating disk or envelope around a HM-YSO.

The total mass of G25.82–W1 is estimated as $20_{\odot}$-$84_{\odot}$ using the 1.3 mm continuum emission while a dynamical mass of > 25 $M_{\odot}$ is measured using the CH_3OH 22_4–21_5 E emission line. The dynamical mass gives the lower limit due to the inclination of the rotation axis. Thus, G25.82–W1 appears to be a HM-YSO surrounded by a rotating disk or envelope. In addition, the luminosity of G25.82–W1, $\sim 1.3 \times 10^4$ $L_{\odot}$, also suggests that G25.82–W1 is a high-mass B0.5 type star with a stellar mass of 12.7 $M_{\odot}$.

Given the multiple outflows and multiple sources, G25.82 is a high-mass cluster formation. G25.82–E is in the UCHII phase while G25.82–W is in an earlier evolutionary phase due to the lack of infrared or cm radio continuum counterparts. Signposts of star formation such as outflowing gas and a rotating structure are shown toward G25.82–W supporting that it is in the early evolutionary stage of high-mass star formation.

Velocity and spatial inconsistency are shown between each outflow map traced by different transitions. The driving source of the N–S CO (SiO) outflow is G25.82–W1 while that of the SE–NW CO (SiO) outflow is uncertain. In the case of the H_2O maser outflow, it could be tracing the interior of the larger scale of outflow (N1–S1 CO outflow and N–S SiO outflow) near the central source, G25.82–W1.

Multiple high-mass starless/protostellar core candidates are detected in G25.82. In contrast, low-mass cores were not detected around G25.82–W despite the high sensitivity of our observations. It implies that HM-YSOs here would be formed in individual high-mass cores, as predicted by the turbulent core accretion model. Although we cannot fully rule out a possibility of unresolved embedded low-mass cores within G25.82–W, high-mass star formation processes in G25.82 could be consistent with a scaled-up version of low-mass star formation model.

For the first time, disk-outflow system in G25.82 is revealed in this thesis. Further studies with higher spatial and spectral resolutions are essential to examine the detailed dynamics of the disk–outflow systems in G25.82–W and derive accurate physical parameters of HM-YSOs. In addition, spatial and spectral analysis of disk tracers and H_2O maser outflow would reveal the driving mechanism of N1–S1 CO outflow (N–S SiO outflow). These result will provide important clues to constrain the direction and inclination of the outflow. Moreover, establishing a schematic view to connect all outflow tracers toward G25.82 to understand the mass ejection history in this region.

Appendix A

Spectra and distribution maps from the KaVA imaging survey

A.1 Present status of KaVA Monitoring Observations

Basically, sources to be monitored were selected based on the results from the snap shot survey. We decided to observe 14 sources including G25.82–0.17 from KaVA imaging survey targets having water masers except already monitored with other VLBI arrays (e.g. G357.967-0.163). In addition, two sources in our primary source list were included based on VERA archival data. In total, 16 sources were selected including VERA two sources. During the operation period of monitoring observations, G18.34+1.78, G11.95-0.16, and G12.88+0.483 were substituted with G75.77+0.34, G6.05-1.45, and G0.54-0.85 because the number of H_2O maser features toward G18.34+1.78, G11.95-0.16, and G12.88+0.483 were not sufficient to achieve our scientific goals.

All data were calibrated in **a** coherent way. Basically we followed general calibration for VLBI data. The total bandwidth was 256 MHz (16 MHz × 16 IFs) and recorded the left-hand circular polarization at a 1 Gbps sampling rate. We analyzed only one of the 16 MHz

IF channels assigned to the H_2O $6_{1,6}$-$5_{2,3}$ transition. The spectral resolution is 15.625 kHz (~0.21 km s $^{-1}$) for the H_2O maser line. Correlated data was delivered from the KJCC (Lee et al., 2015) with the informations for calibration such as measured system temperature. Extragalactic radio continuum sources, NRAO 530, DA193, and BALLAC, were employed for bandpass and delay calibration. Data calibration was also carried out using the AIPS. Gains were calibrated by using the AIPS task APCAL using measured system temperatures. Delays and phase offsets were removed by running AIPS task FRING using aforementioned calibrators. Bandpass response was also calibrated using the same calibrators. Fringe fitting was done on a reference maser component having the highest intensity in each source spectrum. Imaging and CLEAN (deconvolution) were performed using the AIPS task IMAGR. We set the cell size of image as 0.2 mas and the pixel number of each axis as 4096 which was enough to cover all detected H_2O masers proved by imaging survey in the previous section. The peak positions of maser spots were derived by Gaussian fitting to the individual channel images using the AIPS task SAD. We employed image pixels greater than 5σ noise level for the Gaussian fitting to distinguish maser spots from side lobes.

Table A.1. KaVA Monitoring Observations

Source name	R.A. $[^{h\ m\ s}]$	Dec. [° ′ ″]	V_{lsr} [km s^{-1}]	D [kpc]	Epochs	Identifier
G354.61+0.47	17:30:17.13	-33:13:55.10	-24	···	123	
G351.24-0.67	17:20:17.76	-35:54:42.80	-100	1.34[a]	1234	
G75.77+0.34	20:21:41.10	+37:25:54.00	···	3.51[a]	123	IRAS 20198+3716
G49.49-0.39	19:23:43.96	+14:30:31.00	59	5.41[a]	12345	
G49.49-0.37	19:23:40.00	+14:30:51.00	60	5.13[a]	12345	W51N
G45.07+0.13	19:13:22.06	+10:50:53.60	58	8.00[a]	12345678	
G35.19-0.74	18:58:13.10	+01:40:35.00	29	2.19[a]	1234	IRAS 18556+0136
G34.26+0.15	18:53:18.66	+01:14:57.70	55	···	123456	
G30.82-0.05	18:47:46.80	-01:54:36.00	101	···	123456	
G25.82-0.17	18:39:03.63	-06:24:09.50	93.7	···	12345678	
G19.61-0.23	18:27:37.44	-11:56:38.40	40	···	123456	
G18.34+1.78	18:17:49.95	-12:08:06.48	75	···	12	G18.34+1.78SW
G13.87+0.28	18:14:35.83	-16:45:35.90	-5	3.94[a]	12345678	
G11.95-0.16	18:12:21.00	-18:39:35.00	1	···	12	IRAS 18094-1840
G12.88+0.48	18:11:51.40	-17:31:29.60	4	2.50[a]	12	
G10.62-0.38	18:10:28.56	-19:55:49.50	15	4.95[a]	12345678	IRAS 18075-1956
G10.47+0.03	18:08:38.10	-19:51:50.00	-43	8.55[a]	12345	IRAS 18056-1952
G6.05-1.45	18:04:53.02	-24:26:41.69	11	···	12345	IRAS 18018-2426
G0.54-0.85	17:50:14.35	-28:54:31.10	12	···	12345	RCW124

[a] Distances determined by measuring trigonometric parallaxes (Reid et al., 2014).

Appendix B

Linear fit results for H_2O masers features in G25.82

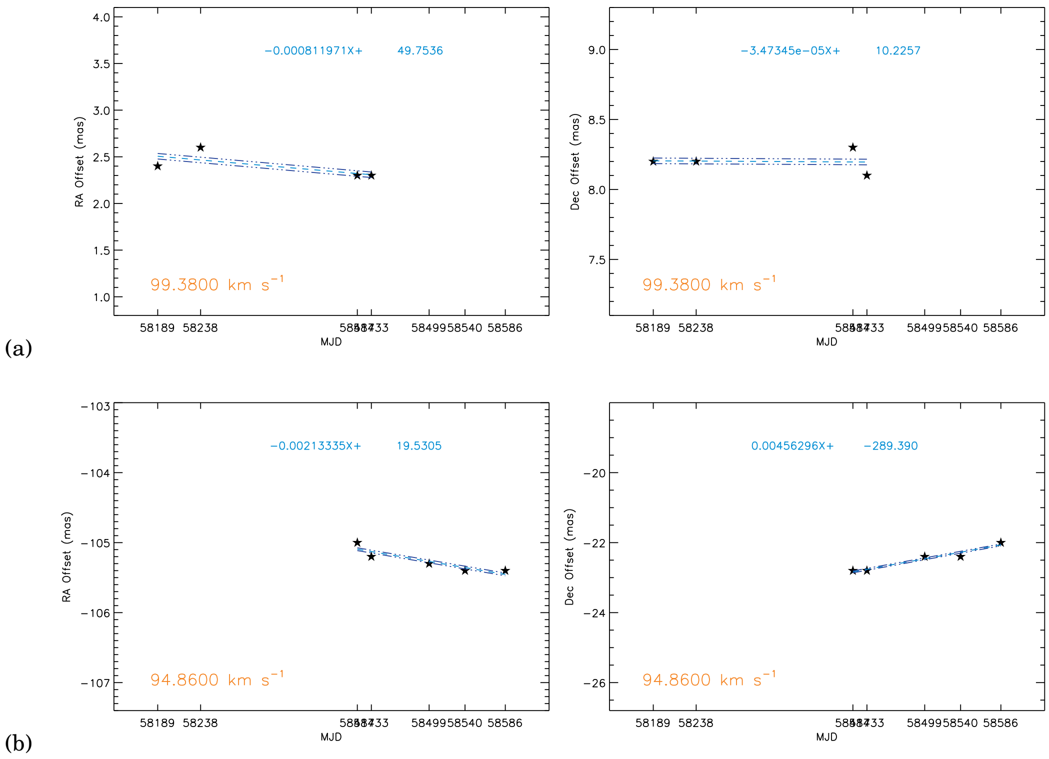

Figure B.1: Linear fitting results of (a) 99.4 km s^{-1} feature and (b) 94.9 km s^{-1} feature. Annotations are the same as Figure 3.6.

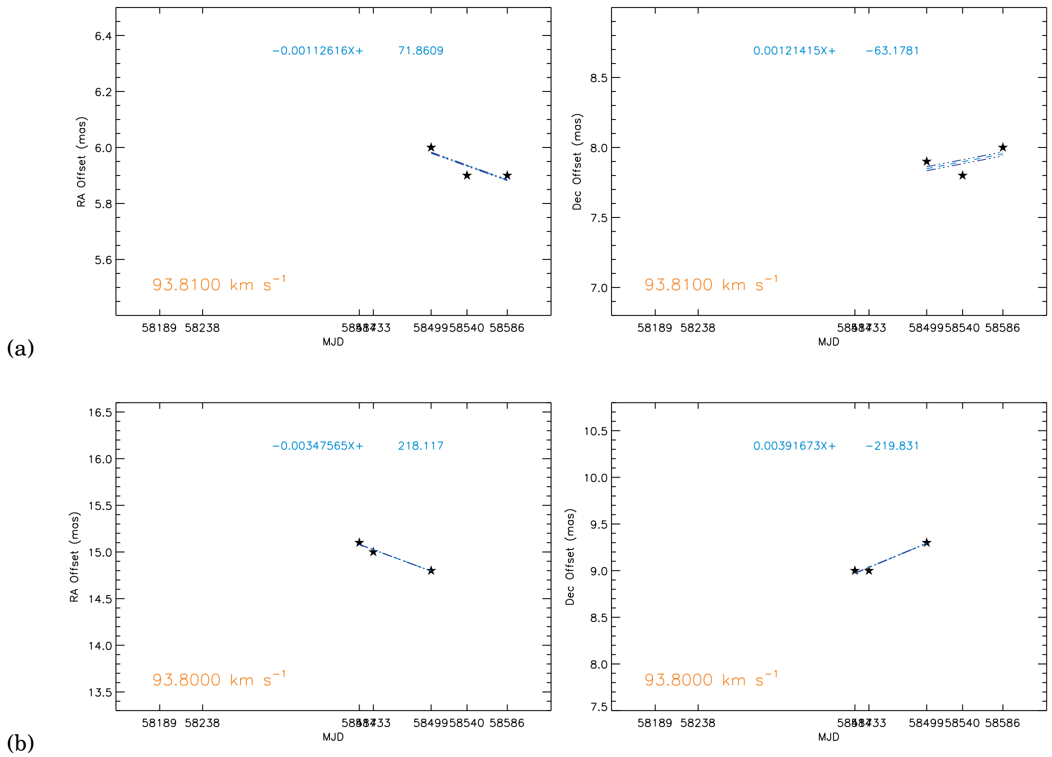

Figure B.2: Linear fitting results of (a) 93.81 km s^{-1} feature and (b) the other 93.8 km s^{-1} feature. Annotations are the same as Figure 3.6.

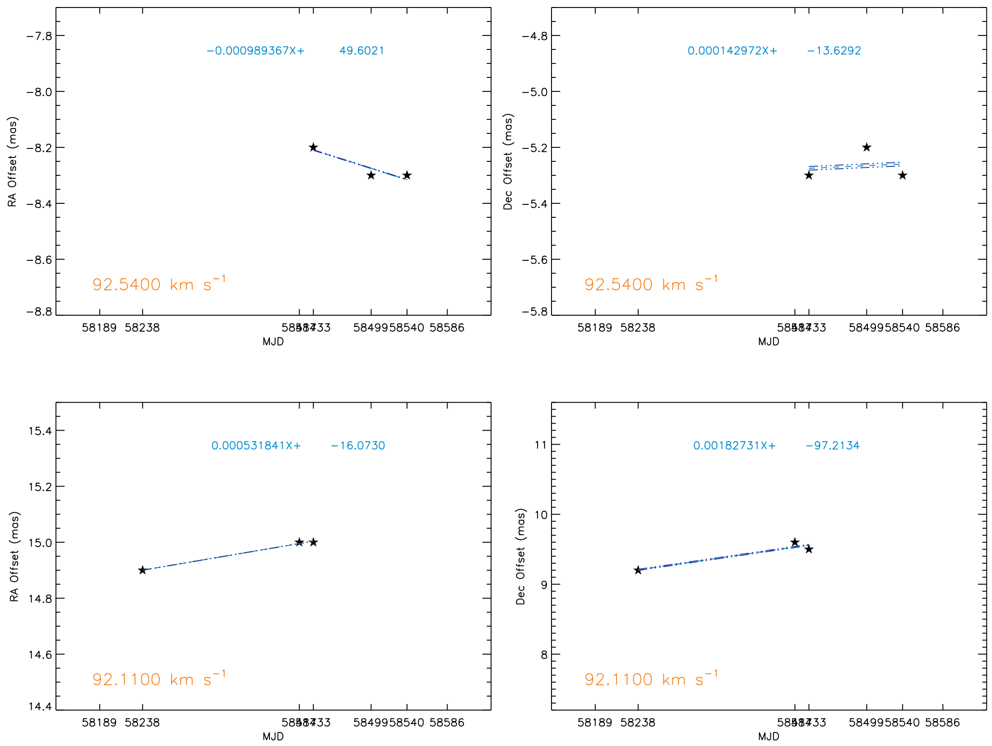

(a)

(b)

Figure B.3: Linear fitting results of (a) 92.5 km s^{-1} feature and (b) 92. km s^{-1} feature. Annotations are the same as Figure 3.6.

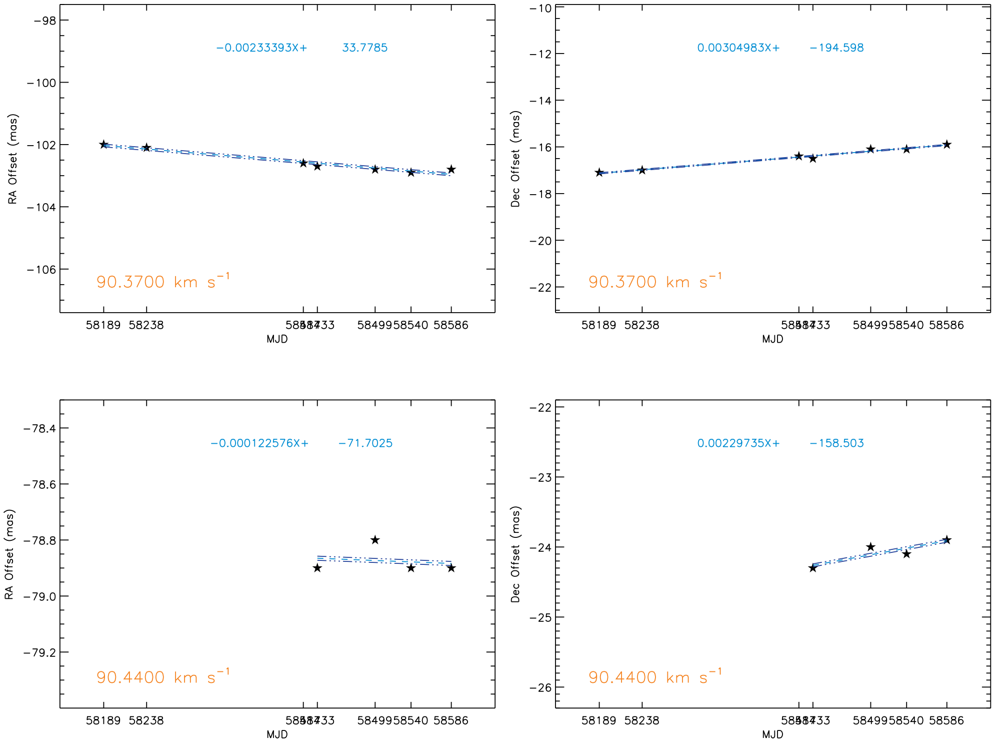

(a)

(b)

Figure B.4: Linear fitting results of (a) 90.4 km s^{-1} feature and (b) 90.4 km s^{-1} feature. Annotations are the same as Figure 3.6.

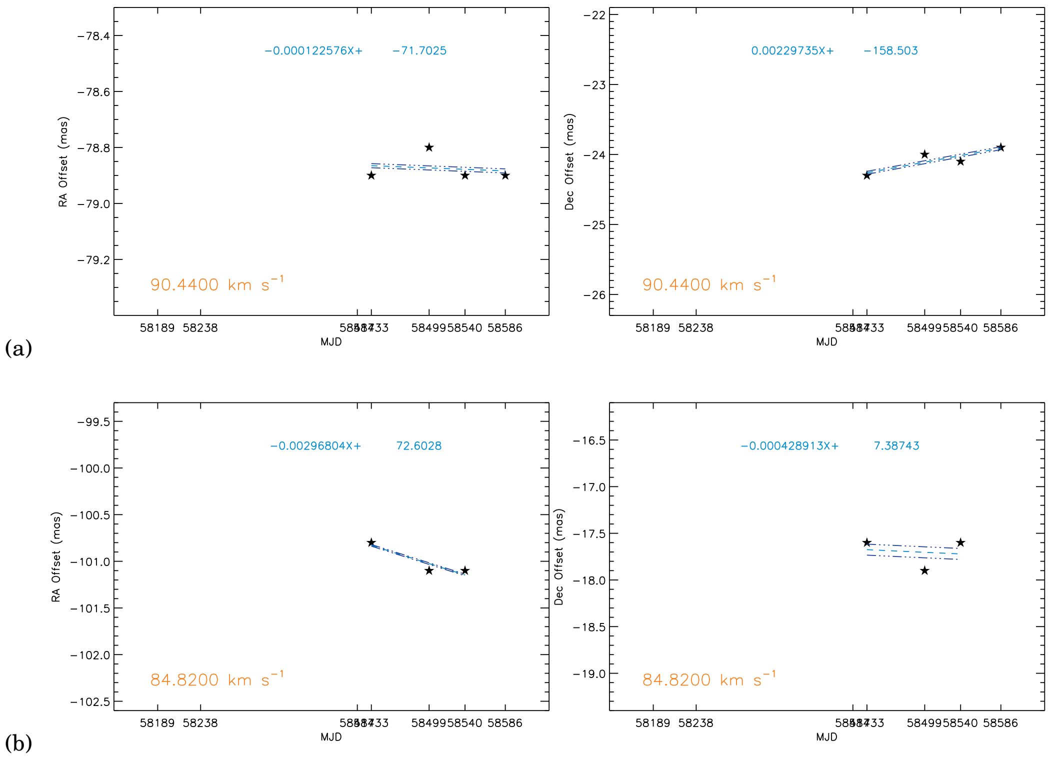

Figure B.5: Linear fitting results of (a) 88.5 km s^{-1} feature and (b) 84.8 km s^{-1} feature. Annotations are the same as Figure 3.6.

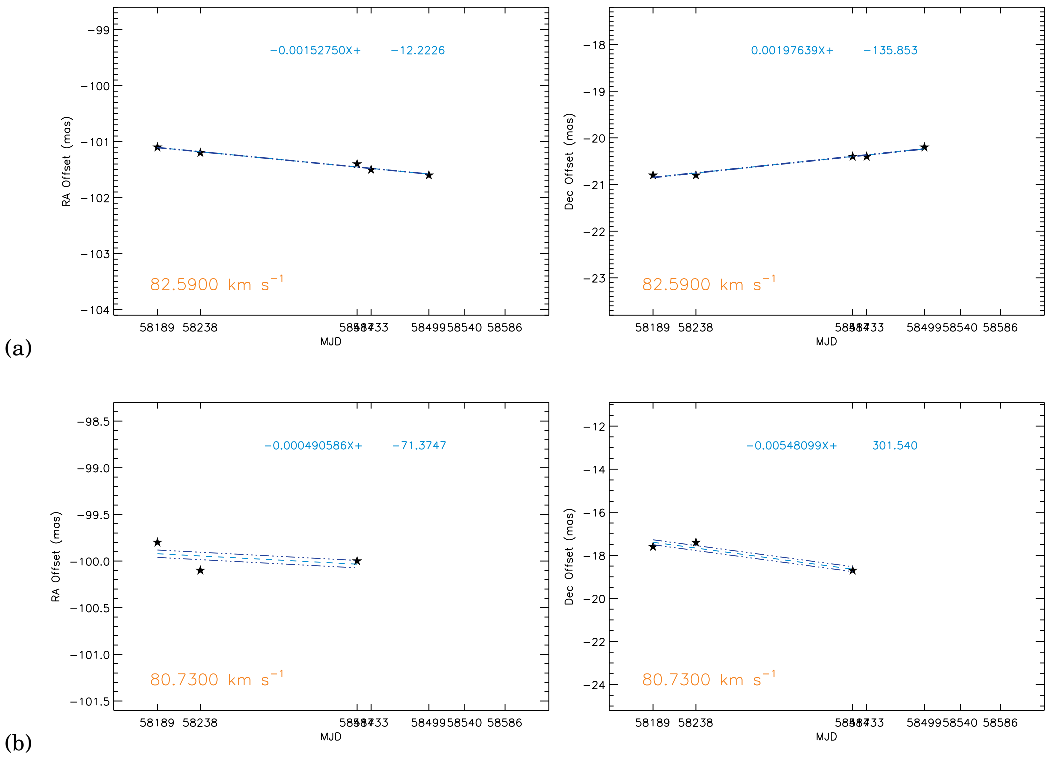

Figure B.6: Linear fitting results of (a) 82.6 km s^{-1} feature and (b) 80.7 km s^{-1} feature. Annotations are the same as Figure 3.6.

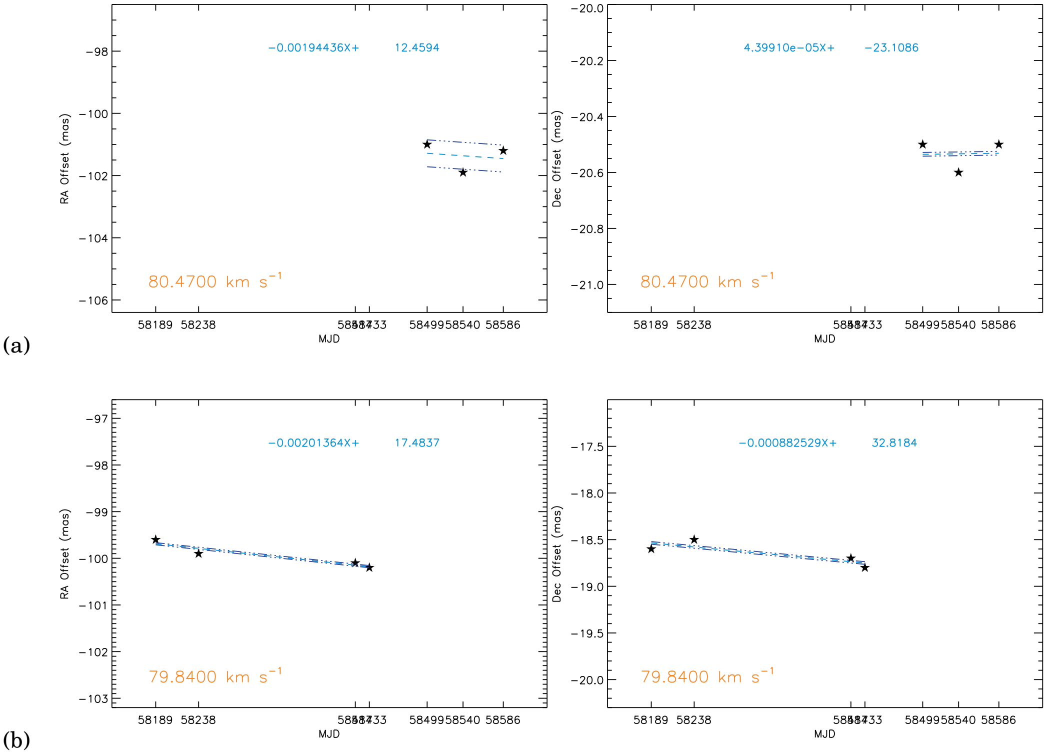

Figure B.7: Linear fitting results of (a) 80.5 km s^{-1} feature and (b) 79.8 km s^{-1} feature. Annotations are the same as Figure 3.6.

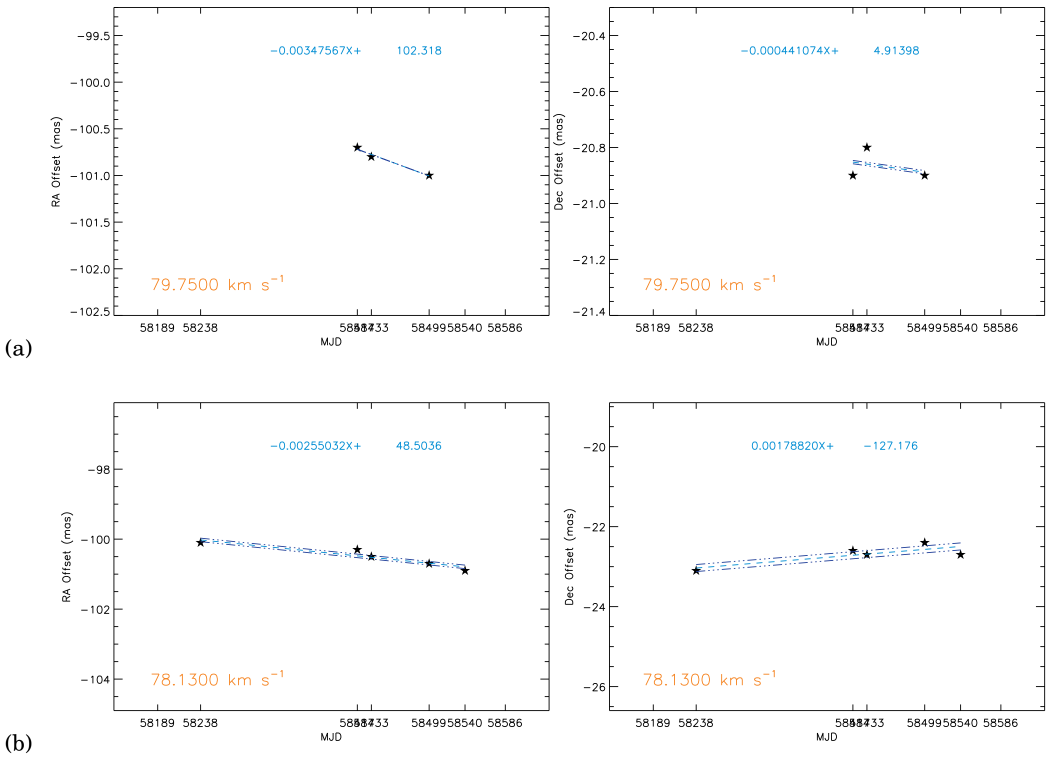

Figure B.8: Linear fitting results of (a) the second 79.8 km s^{-1} feature and (b) 78.1 km s^{-1} feature. Annotations are the same as Figure 3.6.

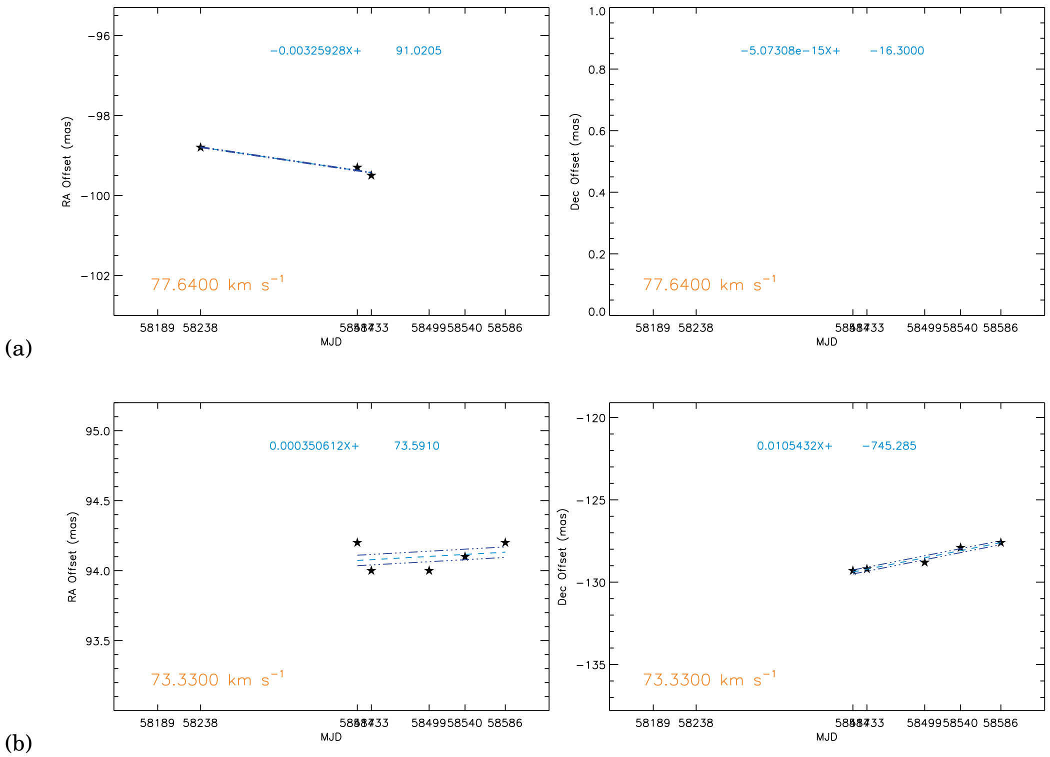

Figure B.9: Linear fitting results of (a) 77.6 km s^{-1} feature and (b) 73.3 km s^{-1} feature. Annotations are the same as Figure 3.6.

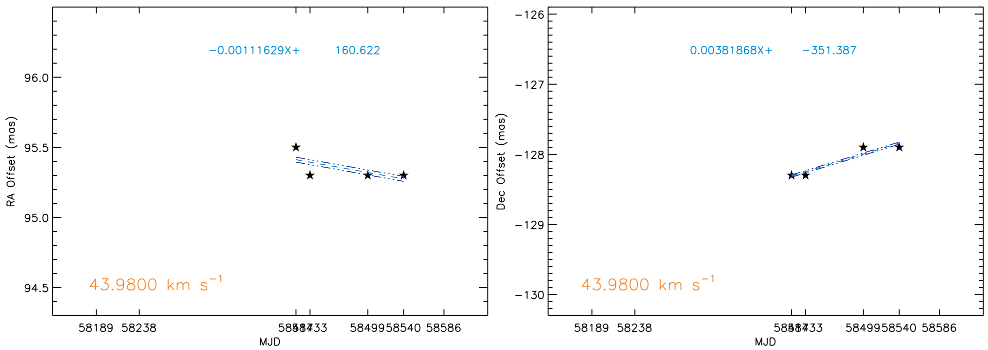

Figure B.10: Linear fitting results of 44.0 km s^{-1} feature. Annotations are the same as Figure 3.6.

Bibliography

Ball, J. A., Gottlieb, C. A., Lilley, A. E., et al. 1970, ApJL, 162, L203

Błaszkiewicz, L., & Kus, A. J. 2004, A&A, 413, 233

Bartkiewicz, A., Szymczak, M., van Langevelde, H. J., et al. 2009, A&A, 502, 155

Beltrán, M. T., Cesaroni, R., Neri, R., et al. 2005, A&A, 435, 901

Beltrán, M. T., Cesaroni, R., Neri, R., et al. 2011, A&A, 525, A151

Beltrán, M. T., Sánchez-Monge, Á., Cesaroni, R., et al. 2014, A&A, 571, A52

Beltrán, M. T., & de Wit, W. J. 2016, A&A Rv, 24, 6

Beltrán, M. T. 2018, Astrophysical Masers: Unlocking the Mysteries of the Universe, 193

Beltrán, M. T., Cesaroni, R., Rivilla, V. M., et al. 2018, A&A, 615, A141

Beuther, H., Schilke, P., Sridharan, T. K., et al. 2002, A&A, 383, 892

Beuther, H., Walsh, A., Schilke, P., et al. 2002, A&A, 390, 289

Beuther, H., & Shepherd, D. 2005, Astrophysics and Space Science Library, 105

Beuther, H. 2007, Triggered Star Formation in a Turbulent ISM, 237, 148

Beuther, H., Walsh, A. J., Johnston, K. G., et al. 2017, A&A, 603, A10

Beuther, H., Linz, H., Henning, T., Feng, S., & Teague, R. 2017, A&A, 605, A61

Bonnell, I. A., & Bate, M. R. 2005, MNRAS, 362, 915

Bonnell, I. A., & Bate, M. R. 2006, MNRAS, 370, 488

Bontemps, S., Andre, P., Terebey, S., et al. 1996, A&A, 311, 858

Bontemps, S., Motte, F., Csengeri, T., et al. 2010, A&A, 524, A18

Bovy, J., Hogg, D. W., & Rix, H.-W. 2009, ApJ, 704, 1704

Brand, J., Cesaroni, R., Comoretto, G., et al. 2003, A&A, 407, 573

Breen, S. L., Ellingsen, S. P., Caswell, J. L., et al. 2010, MNRAS, 401, 2219

Breen, S. L., Ellingsen, S. P., Contreras, Y., et al. 2013, MNRAS, 435, 524

Breen, S. L., Fuller, G. A., Caswell, J. L., et al. 2015, MNRAS, 450, 4109

Breen, S. L., Ellingsen, S. P., Caswell, J. L., et al. 2016, MNRAS, 459, 4066

Burns, R. A., Imai, H., Handa, T., et al. 2015, MNRAS, 453, 3163

Burns, R. A., Handa, T., Imai, H., et al. 2017, MNRAS, 467, 2367

Brunthaler, A., Reid, M. J., Menten, K. M., et al. 2009, ApJ, 693, 424

Cesaroni, R., Galli, D., Lodato, G., et al. 2006, Nature, 444, 703

Cesaroni, R., Galli, D., Lodato, G., et al. 2007, Protostars and Planets V, 197

Cesaroni, R., Beltrán, M. T., Zhang, Q., et al. 2011, A&A, 533, A73

Cesaroni, R., Sánchez-Monge, Á., Beltrán, M. T., et al. 2017, A&A, 602, A59

Cheung, A. C., Rank, D. M., Townes, C. H., et al. 1968, Physical Review Letters, 21, 1701

Chibueze, J. O., Omodaka, T., Handa, T., et al. 2014, ApJ, 784, 114

Codella, C., Beltrán, M. T., Cesaroni, R., et al. 2013, A&A, 550, A81

Commerçon, B., Hennebelle, P., & Henning, T. 2011, ApJL, 742, L9

Cyganowski, C. J., Brogan, C. L., Hunter, T. R., & Churchwell, E. 2009, ApJ, 702, 1615

Cyganowski, C. J., Brogan, C. L., Hunter, T. R., et al. 2014, ApJL, 796, L2

De Buizer, J. M., Bartkiewicz, A., & Szymczak, M. 2012, ApJ, 754, 149

de Villiers, H. M., Chrysostomou, A., Thompson, M. A., et al. 2014, MNRAS, 444, 566

de Wit, W. J., Testi, L., Palla, F., et al. 2005, A&A, 437, 247

Downes, T. P., & Cabrit, S. 2007, A&A, 471, 873

Duarte-Cabral, A., Bontemps, S., Motte, F., et al. 2013, A&A, 558, A125

Ellingsen, S. P., Voronkov, M. A., Cragg, D. M., et al. 2007, Astrophysical Masers and Their Environments, 213

Evans, N. J., II, Dunham, M. M., Jørgensen, J. K., et al. 2009, ApJs, 181, 321

Fish, V. L., Muehlbrad, T. C., Pratap, P., et al. 2011, ApJ, 729, 14

Fontani, F., Cesaroni, R., & Furuya, R. S. 2010, A&A, 517, A56

Fujisawa, K., Takase, G., Kimura, S., et al. 2014, PASJ, 66, 78

Ghez, A. M., Salim, S., Weinberg, N. N., et al. 2008, ApJ, 689, 1044

Gillessen, S., Eisenhauer, F., Fritz, T. K., et al. 2009, ApJL, 707, L114

Goddi, C., Moscadelli, L., Alef, W., et al. 2005, A&A, 432, 161

Goddi, C., & Moscadelli, L. 2006, A&A, 447, 577

Goddi, C., Moscadelli, L., Sanna, A., et al. 2007, A&A, 461, 1027

Goddi, C., Moscadelli, L., & Sanna, A. 2011, A&A, 535, L8

Green, J. A., & McClure-Griffiths, N. M. 2011, MNRAS, 417, 2500

Hennebelle, P., Commerçon, B., Joos, M., et al. 2011, A&A, 528, A72

Henning, T., Schreyer, K., Launhardt, R., et al. 2000, A&A, 353, 211

Hildebrand, R. H. 1983, QJRAS, 24, 267

Hirota, T., Machida, M. N., Matsushita, Y., et al. 2017, Nature Astronomy, 1, 0146

Hirota, T. 2018, Publication of Korean Astronomical Society, 33, 21

Honma, M., Kijima, M., Suda, H., et al. 2008, PASJ, 60, 935

Honma, M., Tamura, Y., & Reid, M. J. 2008, PASJ, 60, 951

Hu, B., Menten, K. M., Wu, Y., et al. 2016, ApJ, 833, 18

Ilee, J. D., Cyganowski, C. J., Brogan, C. L., et al. 2018, ApJL, 869, L24

Imai, H., Watanabe, T., Omodaka, T., et al. 2002, PASJ, 54, 741

Imai, H., Sakai, N., Nakanishi, H., et al. 2012, PASJ, 64, 142

Jijina, J., & Adams, F. C. 1996, ApJ, 462, 874

Kang, H., Kim, K.-T., Byun, D.-Y., et al. 2015, ApJs, 221, 6

Kim, C.-H., Kim, K.-T., & Park, Y.-S. 2018, ApJs, 236, 31

Kim, J., Hirota, T., Kim, K.-T., et al. 2018, Astrophysical Masers: Unlocking the Mysteries of the Universe, 303

Kim, J., Kim, M. K., Hirota, T., et al. 2020, ApJ, 896, 127

Kim, K.-T., Byun, D.-Y., Je, D.-H., et al. 2011, Journal of Korean Astronomical Society, 44, 81

Klassen, M., Pudritz, R. E., Kuiper, R., et al. 2016, ApJ, 823, 28

Kong, S., Tan, J. C., Caselli, P., et al. 2017, ApJ, 834, 193

Könyves, V., André, P., Men'shchikov, A., et al. 2010, A&A, 518, L106

Krumholz, M. R., McKee, C. F., & Klein, R. I. 2005, Nature, 438, 332

Krumholz, M. R., Klein, R. I., & McKee, C. F. 2007, ApJ, 656, 959

Krumholz, M. R., Klein, R. I., McKee, C. F., Offner, S. S. R., & Cunningham, A. J. 2009, Science, 323, 754

Kuiper, R., Klahr, H., Beuther, H., & Henning, T. 2010, ApJ, 722, 1556

Kuiper, R., Klahr, H., Beuther, H., & Henning, T. 2011, ApJ, 732, 20

Kurtz, S., Cesaroni, R., Churchwell, E., et al. 2000, Protostars and Planets IV, 299

Kurtz, S., Hofner, P., & Álvarez, C. V. 2004, ApJs, 155, 149

Lee, S.-S., Oh, C. S., Roh, D.-G., et al. 2015, Journal of Korean Astronomical Society, 48, 125

Leurini, S., Codella, C., López-Sepulcre, A., et al. 2014, A&A, 570, A49

Liu, T., Kim, K.-T., Wu, Y., et al. 2015, ApJ, 810, 147

Liu, T., Zhang, Q., Kim, K.-T., et al. 2016, ApJ, 824, 31

López-Sepulcre, A., Walmsley, C. M., Cesaroni, R., et al. 2011, A&A, 526, L2

Mason, B. D., Hartkopf, W. I., Gies, D. R., et al. 2009, AJ, 137, 3358

Matsumoto, N., Hirota, T., Sugiyama, K., et al. 2014, ApJL, 789, L1

Matsushita, Y., Machida, M. N., Sakurai, Y., & Hosokawa, T. 2017, MNRAS, 470, 1026

Matsushita, Y., Sakurai, Y., Hosokawa, T., & Machida, M. N. 2018, MNRAS, 475, 391

Matsushita, Y., Takahashi, S., Machida, M. N., & Tomisaka, K. 2019, ApJ, 871, 221

Maud, L. T., Moore, T. J. T., Lumsden, S. L., et al. 2015, MNRAS, 453, 645

Maud, L. T., Cesaroni, R., Kumar, M. S. N., et al. 2018, A&A, 620, A31

Maud, L. T., Cesaroni, R., Kumar, M. S. N., et al. 2019, A&A, 627, L6

Menten, K. M. 1991, ApJL, 380, L75

McKee, C. F., & Tan, J. C. 2002, Nature Astronomy, 416, 59

McKee, C. F., & Tan, J. C. 2003, ApJ, 585, 850

McMullin, J. P., Waters, B., Schiebel, D., Young, W., & Golap, K. 2007, Astronomical Data Analysis Software and Systems XVI, 376, 127

Moscadelli, L., Cesaroni, R., & Rioja, M. J. 2000, A&A, 360, 663

Moscadelli, L., Cesaroni, R., & Rioja, M. J. 2005, A&A, 438, 889

Moscadelli, L., Cesaroni, R., Rioja, M. J., et al. 2011, A&A, 526, A66

Moscadelli, L., Sánchez-Monge, Á., Goddi, C., et al. 2016, A&A, 585, A71

Moscadelli, L., Rivilla, V. M., Cesaroni, R., et al. 2018, A&A, 616, A66

Moscadelli, L., Sanna, A., Cesaroni, R., et al. 2019, A&A, 622, A206

Moscadelli, L., Sanna, A., Goddi, C., et al. 2019, A&A, 631, A74

Moscadelli, L., Sanna, A., Goddi, C., et al. 2020, A&A, 635, A118

Motogi, K., Sorai, K., Honma, M., et al. 2016, PASJ, 68, 69

Motogi, K., Hirota, T., Sorai, K., et al. 2017, ApJ, 849, 23

Motogi, K., Hirota, T., Machida, M. N., et al. 2019, ApJL, 877, L25

Motte, F., Bontemps, S., & Louvet, F. 2017, ARA&A, 56, 41

Mottram, J. C., Hoare, M. G., Davies, B., et al. 2011, ApJL, 730, L33

Müller, H. S. P., Thorwirth, S., Roth, D. A., et al. 2001, A&A, 370, L49

Nagayama, T., Kobayashi, H., Hirota, T., et al. 2020, PASJ, doi:10.1093/pasj/psaa034

Nakano, T. 1989, ApJ, 345, 464

Norris, R. P., Whiteoak, J. B., Caswell, J. L., et al. 1993, ApJ, 412, 222

Ossenkopf, V., & Henning, T. 1994, A&A, 291, 943

Oyama, T., Kono, Y., Suzuki, S., et al. 2016, PASJ, 68, 105

Pickett, H. M., Poynter, R. L., Cohen, E. A., et al. 1998, JQSRT, 60, 883

Preibisch, T., Balega, Y., Hofmann, K.-H., et al. 1999, New Astron., 4, 531

Reid, M. J., Menten, K. M., Zheng, X. W., et al. 2009, ApJ, 700, 137

Reid, M. J., Menten, K. M., Brunthaler, A., et al. 2014, ApJ, 783, 130

Reid, M. J. 2018, Astrophysical Masers: Unlocking the Mysteries of the Universe, 336, 148

Russeil, D., Zavagno, A., Motte, F., et al. 2010, A&A, 515, A55

Sana, H. & Evans, C. J. 2011, Active OB Stars: Structure, Evolution, Mass Loss, and Critical Limits, 272, 474

Sánchez-Monge, Á., Beltrán, M. T., Cesaroni, R., et al. 2014, A&A, 569, A11

Sanhueza, P., Jackson, J. M., Zhang, Q., et al. 2017, ApJ, 841, 97

Sato, M., Wu, Y. W., Immer, K., et al. 2014, ApJ, 793, 72

Sault, R. J., Teuben, P. J., & Wright, M. C. H. 1995, Astronomical Data Analysis Software and Systems IV, 77, 433

Sanna, A., Moscadelli, L., Cesaroni, R., et al. 2016, A&A, 596, L2

Sanna, A., Moscadelli, L., Goddi, C., et al. 2018, A&A, 619, A107

Sanna, A., Moscadelli, L., Goddi, C., et al. 2019, A&A, 623, L3

Schnee, S., Caselli, P., Goodman, A., et al. 2007, ApJ, 671, 1839

Schönrich, R., Binney, J., & Dehnen, W. 2010, MNRAS, 403, 1829

Scoville, N. Z., & Kwan, J. 1976, ApJ, 206, 718

Seifried, D., Pudritz, R. E., Banerjee, R., et al. 2012, MNRAS, 422, 347

Shirley, Y. L., Ellsworth-Bowers, T. P., Svoboda, B., et al. 2013, ApJS, 209, 2

Shepherd, D. S., & Churchwell, E. 1996, ApJ, 472, 225

Slysh, V. I., Kalenskiĭ, S. V., & Val'tts, I. E. 2002, Astronomy Reports, 46, 49

Stahler, S. W., & Palla, F. 2005, The Formation of Stars

Sugiyama, K., Fujisawa, K., Doi, A., et al. 2014, A&A, 562, A82

Surcis, G., Vlemmings, W. H. T., van Langevelde, H. J., et al. 2014, A&A, 565, L8

Surcis, G., Vlemmings, W. H. T., van Langevelde, H. J., et al. 2019, A&A, 623, A130

Tan, J. C., Kong, S., Butler, M. J., et al. 2013, ApJ, 779, 96

Tan, J. C., Beltrán, M. T., Caselli, P., et al. 2014, Protostars and Planets VI, 149

Torrelles, J. M., Gómez, J. F., Rodríguez, L. F., et al. 1997, ApJ, 489, 744

Urquhart, J. S., Morgan, L. K., Figura, C. C., et al. 2011, MNRAS, 418, 1689

van der Marel, N., Kristensen, L. E., Visser, R., et al. 2013, A&A, 556, A76

van Moorsel, G., Kemball, A., & Greisen, E. 1996, Astronomical Data Analysis Software and Systems V, 37

VERA Collaboration, Hirota, T., Nagayama, T., et al. 2020, PASJ, doi:10.1093/pasj/psaa018

Walsh, A. J., Hyland, A. R., Robinson, G., et al. 1997, MNRAS, 291, 261

Walsh, A. J., Burton, M. G., Hyland, A. R., et al. 1998, MNRAS, 301, 640

Wang, K., Zhang, Q., Testi, L., et al. 2014, MNRAS, 439, 3275

Weaver, H., Williams, D. R. W., Dieter, N. H., et al. 1965, Nature, 208, 29

Wienen, M., Wyrowski, F., Schuller, F., et al. 2012, A&A, 544, A146

Wright, E. L., Eisenhardt, P. R. M., Mainzer, A. K., et al. 2010, AJ, 140, 1868

Wu, Y., Wei, Y., Zhao, M., et al. 2004, A&A, 426, 503

Yanagida, T., Sakai, T., Hirota, T., et al. 2014, ApJL, 794, L10

Yorke, H. W., & Sonnhalter, C. 2002, ApJ, 569, 846

Zhang, B., Moscadelli, L., Sato, M., et al. 2014, ApJ, 781, 89

Zhang, Q., Hunter, T. R., Beuther, H., et al. 2007, ApJ, 658, 1152

Zhang, Q., Wang, Y., Pillai, T., et al. 2009, ApJ, 696, 268

Zinnecker, H., & Yorke, H. W. 2007, ARA&A, 45, 481